

UNIVERSIDAD AUTÓNOMA DE SAN LUÍS POTOSÍ

Doctorado Institucional en Ingeniería y Ciencia de Materiales

Efficient separation and recovery of critical metals from aqueous solution by adsorption and electrosorption

PARA OBTENER EL GRADO DE

DOCTORA EN INGENIERÍA Y CIENCIA DE MATERIALES

QUE PRESENTA

Ning Wang

DIRECTORA y Co-DIRECTOR

Dra. Mildred Quintana Ruiz and Dr Shaoxian Song



PATROCINADO POR SECIHTI Beca número 1327523

San Luis Potosí, S.L.P. Noviembre de 2026

UNIVERSIDAD AUTÓNOMA DE SAN LUÍS POTOSÍ

Doctorado Institucional en Ingeniería y Ciencia de Materiales

Efficient separation and recovery of critical metals from aqueous solution by adsorption and electrosorption

QUE PARA OBTENER EL GRADO DE

DOCTORA EN INGENIERÍA Y CIENCIA DE MATERIALES

QUE PRESENTA

Ning Wang

DIRECTORA y Co-DIRECTOR

Dra. Mildred Quintana Ruiz and Dr Shaoxian Song

Sinodales

Dra. Mildred Quintana Ruiz _____

Dr. Shaoxian Song _____

Dra. Socorro Oros Ruiz _____

Dr. Hiram Joazet Ojeda Galván _____

Dra. Selene Concepción Acosta Morales _____

Dra. Verónica Pérez-Luna _____

San Luis Potosí, S.L.P. Noviembre de 2026



Efficient separation and recovery of critical metals from aqueous solution by adsorption and electrosorption by Ning Wang is licensed under Attribution-NonCommercial-NoDerivatives 4.0 International

Acknowledgement

Gratitude is the quietest and most lasting harvest of a long journey.

This thesis marks the end of my doctoral journey and the beginning of a new chapter in my life. Here, I wish to thank all the advisors, family, classmates, and friends who have guided me, supported me, encouraged me, and accompanied me throughout these years of study and research. Every achievement presented in this thesis and every step of my personal and academic growth would not have been possible without your kindness, encouragement, and generous support.

A great mentor is like a guiding light, illuminating the path ahead. My deepest gratitude goes to Professor Mildred Quintana Ruiz for her invaluable guidance throughout my doctoral studies, her patience and encouragement in my research, and her thoughtful care during my time in Mexico. Her rigorous scientific thinking and open-minded approach broadened my academic perspective, while her warmth eased the loneliness of living far from home and allowed me to pursue my studies with confidence and focus. I am also sincerely grateful to Professor Shaoxian Song and Professor Feifei Jia. Their valuable input and insight benefited every stage of my doctoral research. Their rigorous scholarship, profound academic insight, and dedication to research have deeply influenced me and will continue to guide my academic and personal development. I am equally grateful to all the professors who taught and guided me during doctoral studies. In particular, I would like to thank Professor Socorro Oros Ruiz, Professor Hiram Joazet Ojeda Galván, Professor Selene Concepción Acosta Morales, Professor Verónica Pérez-Luna, Professor José Adrián Martínez-González and Professor Yanmei Li for their encouragement and support. I will always remember their encouragement and generosity.

Family is a harbor that shelters me through every storm. Throughout my academic journey, my parents have always been my strongest source of support. I am deeply grateful to my parents for their love, upbringing, and guidance. Through their simple yet enduring example, they taught me kindness, generosity, diligence, and perseverance, and showed me the importance of remaining grounded while pursuing one's goals with determination. They have supported every choice I have made, quietly shouldered the burdens of life, and made it possible for me to pursue my education without hesitation. Years of studying far from home have meant that I have spent far too little time by their side, something for which I have always felt deeply sorry. Everything I have achieved

today rests upon their selfless devotion and unwavering trust. Their love and expectations will always give me the courage to face whatever lies ahead. I would also like to express my heartfelt gratitude to Jinen Li. During the most difficult and uncertain periods of my doctoral journey, you were always there with patience, understanding, and unwavering support. Your companionship eased the anxiety and exhaustion of these years and stayed with me through both struggle and growth. Y You taught me to face life with gentleness, strength, and determination. You have been a warm light in my life, and I feel deeply fortunate to have you by my side.

True friends are like stars, shining through the long nights. The path of research can often be lonely and demanding, and I feel fortunate to have shared these years with such wonderful friends and classmates. I would like to express my sincere gratitude to Weiquan Zhang, Jie Wu, Cui Zhang, Lingjie Zhang, Lei Hou, Yingxin Chen, Huan Zhang, Zhenlei Wang, Jianhui Zhu, and Yunjia Ling for generously sharing their research experience, patiently discussing academic questions with me, and offering invaluable support whenever I encountered difficulties. I also extend my thanks to everyone at LAMCC. The friendship we have built over the years is something I will always cherish, and I hope it will endure long into the future.

Time has passed swiftly, and these years seem to have gone by in an instant. Looking back on my doctoral journey, there were moments of uncertainty and hardship, but also abundant rewards and continuous growth. Every challenge I have faced and every distance I have travelled has become a source of strength, giving me greater composure, resilience, and confidence for the future.

Finally, I sincerely acknowledge the financial support provided by the Secretariat of Science, Humanities, Technology, and Innovation (SECIHTI) of Mexico under Grant No. 1327523.

I am grateful for every encounter along the way, bidding farewell to the past with sincerity and stepping toward the future with conviction.

Ning Wang

Mexico

Abstract

The sustainable recovery of critical metals such as gallium, indium, and platinum group metals from aqueous systems is of great importance for securing resource supply, supporting economic development, and reducing environmental burdens. Their occurrence at low concentrations, the presence of complex coexisting ions, and the similar chemical properties of different metals make it difficult to simultaneously achieve high recovery efficiency and selective separation, placing higher demands on the interfacial recognition capability of functional materials and on separation and recovery technologies. In this study, a series of molybdenum-based materials and porous carbon materials were developed, with chemisorption and electrosorption activities regulated to enable the efficient separation and recovery of low-concentration critical metals from complex aqueous systems.

Herein, the separation and recovery technologies for critical metals were first systematically reviewed, with particular emphasis on the structure-performance relationships, adsorption mechanisms, and limitations of gallium adsorbents. To improve gallium adsorption performance, molybdenum oxide was modified through nitrogen doping and defect regulation, yielding a maximum adsorption capacity of 464.8 mg g^{-1} with high selectivity. To overcome mass-transfer limitations at low concentrations, bimetallic heterointerfaces were constructed for electro-assisted preferential gallium recovery, suppressing competitive hydrogen evolution and achieving recovery efficiencies of 97.3-98.2% at trace concentrations of 0.5-1.0 mg L^{-1}. This study provides theoretical insights and technical support for the sustainable recovery of critical metals from secondary aqueous resources.

Resumen

La recuperación sostenible de metales críticos, como el galio, el indio y los metales del grupo del platino, a partir de sistemas acuosos es de gran importancia para garantizar el suministro de recursos, impulsar el desarrollo económico y reducir las cargas ambientales. Su presencia a bajas concentraciones, la coexistencia de mezclas complejas de iones y las propiedades químicas similares de distintos metales dificultan alcanzar simultáneamente una alta eficiencia de recuperación y una separación selectiva, lo que impone mayores exigencias tanto a la capacidad de reconocimiento interfacial de los materiales funcionales como a las tecnologías de separación y recuperación. En este estudio se desarrolló una serie de materiales a base de molibdeno y materiales de carbono poroso, cuyas actividades de quimisorción y electrosorción fueron reguladas para posibilitar la separación y recuperación eficientes de metales críticos presentes a bajas concentraciones en sistemas acuosos complejos.

En primer lugar, se revisaron sistemáticamente las tecnologías de separación y recuperación de metales críticos, con especial énfasis en las relaciones estructura–rendimiento, los mecanismos de adsorción y las limitaciones de los adsorbentes de galio. Para mejorar el desempeño de adsorción de galio, el óxido de molibdeno se modificó mediante dopaje con nitrógeno y regulación de defectos, alcanzándose una capacidad máxima de adsorción de 464.8 mg g^{-1} y una alta selectividad. Para superar las limitaciones de transferencia de masa a bajas concentraciones, se construyeron heterointerfaces bimetálicas para la recuperación preferencial de galio asistida electroquímicamente, reduciendo la influencia de la evolución competitiva de hidrógeno y alcanzando eficiencias de recuperación de 97.3-98.2% a concentraciones traza de 0.5-1.0 mg L^{-1}. Posteriormente, la separación electroquímica selectiva de galio e indio se logró mediante la integración del control de la especiación en solución con interfaces de disulfuro de molibdeno dopado con nitrógeno, obteniéndose un coeficiente máximo de selectividad galio/indio de 193.0 en medio cloruro. Finalmente, la estrategia de acoplamiento de quimisorción y electrosorción se extendió a metales del grupo del platino fácilmente reducibles mediante electrodos de biocarbón poroso catiónico, lo que permitió la reducción electroquímica directa de $[PtCl_6]^{2-}$ a platino metálico con una eficiencia de recuperación de 95.1%; además, la estrategia también fue aplicable a $[PdCl_4]^{2-}$ y $[RhCl_6]^{3-}$. Este estudio aporta fundamentos teóricos y soporte técnico para la recuperación sostenible de metales críticos a partir de recursos acuosos secundarios.

Extended Abstract

Modern technological development and the global energy transition have heightened the importance of a secure and sustainable supply of critical metals. Industrial process streams, metallurgical effluents, and other secondary aqueous resources are increasingly recognized as potentially viable sources for recovering critical metals such as gallium, indium, and platinum group metals (PGMs). However, target metals in these streams are typically present at low concentrations and coexist with chemically similar or more abundant competing ions, posing substantial challenges to efficient and selective recovery. In this study, a novel strategy was proposed for the efficient recovery of gallium, indium, and PGMs at low concentrations by regulating the chemisorption and electrosorption activities of molybdenum-based materials and porous carbon materials.

To improve the adsorption capacity and selectivity for gallium, nitrogen-doped and vacancy-engineered synergistically modified molybdenum oxide nanowires (α-MoO_x/N) were rationally designed. The introduction of a moderate amount of ethylenediamine induced the transition of α-MoO_x to the amorphous state. Mixed-valence α-MoO_x/N-0.53 (Mo(V) and Mo(VI)) with abundant active sites notably enhanced the adsorption kinetics of gallium ions, with 98.9% of gallium ions adsorbed within 60 min. Compared with most reported gallium adsorbents, α-MoO_x/N-0.53 exhibited the maximum adsorption capacity of 464.8 mg g^{-1} (298 K), mainly attributed to the synergistic effect of electrostatic adsorption, ion exchange with H^+ as well as surface complexation with Mo-O and pyridinic N. The self-enhanced adsorption mechanism and oxygen vacancies as gallium ion adsorption traps in α-MoO_x/N-0.53 augmented the opportunities for capturing gallium ions. Excellent selective adsorption of gallium ions from binary and multicomponent systems containing Zn^{2+}, Al^{3+}, Cu^{2+}, Ni^{2+}, together with robust cycling stability, further endorse α-MoO_x/N as the promising candidate for recovering gallium ions.

To address the limited recovery efficiency of traditional adsorption methods under low-concentration conditions, an asymmetric chemisorption and electrosorption coupling (CEC) strategy centered on a bimetallic molybdenum oxide/tin oxide (MoO_3/SnO_2) was proposed to achieve preferential recovery of gallium ions from various electrolytes. Controlled incorporation of SnO_2 triggered charge rearrangement at the heterointerface, thereby contributing to the suppression of the hydrogen evolution

reaction. Under an applied electric field, oxygen coordination between the electrode and gallium ions enhanced the electrical double-layer capacitance and reduced electron transport resistance, promoting the rapid capture of gallium ions. The CEC system achieved a gallium recovery capacity of up to 486.3 mg g^{-1} over an initial concentration range of 0.5-200 mg L^{-1}. Notably, at trace concentrations of only 0.5-1.0 mg L^{-1}, gallium recovery efficiencies remained as high as 97.3-98.2%, and more than 81.5% of the saturation capacity was reached within 1 h. Stepwise voltage regulation within a low-voltage window of 1.0-1.8 V and specific adsorption at the electrode jointly endowed the CEC system with outstanding gallium selectivity in complex solutions.

Contents

Acknowledgement II
Abstract I
Resumen II
Extended Abstract III
Contents V
Index of Figures VIII
Index of Tables XII
Chapter 1. Introduction 1
1.1. Justification 1
1.2. Objectives 2
1.2.1. General objective 2
1.2.2. Goals 3
1.3. References 3
Chapter 2. Literature Review 5
2.1. Introduction 5
2.2. Gallium separation and recovery: Focus on adsorption 8
2.2.1. Functional ligands for gallium adsorption 8
2.2.2. Solid supports 15
2.2.3. Adsorption mechanism 19
2.2.4. Current limitations of the gallium adsorption method 21
2.3. Electro-assisted gallium adsorption 22
2.3.1. Chemisorption and electrosorption coupling method 22
2.3.2. Design principles for electrode materials 25
2.4. Summary and perspectives 27
2.5. References 28
Chapter 3. Nitrogen-doped and vacancy-engineered molybdenum oxide for selective gallium adsorption 40
3.1. Introduction 40
3.2. Experimental section 42
3.2.1. Reagents and materials 42
3.2.2. Syntheses of α-MoO_x and α-MoO_x/N 42

3.2.3. Adsorption experiment....43
3.2.4. Selective adsorption....44
3.2.5. Circulation recovery of gallium....45
3.2.6. Characterizations....45
3.3. Results and discussion....46
3.3.1. Characterization of α-MoO_x and α-MoO_x/N....46
3.3.2. Anti-interference performance....50
3.3.3. Gallium ions uptake capacity....56
3.3.4. Adsorption mechanism....60
3.3.5. Adsorption and desorption Cycles....63
3.3.6. Gallium ions adsorption from zinc slag leachate....65
3.4. Conclusions....65
3.5. References....66
Chapter 4. Electro-assisted preferential gallium capture at bimetallic oxide heterointerfaces 74
4.1. Introduction....74
4.2. Experimental section....77
4.2.1. Reagents and materials....77
4.2.2. Fabrication of composite MoO_3/SnO_2 electrodes....77
4.2.3. Chemisorption and electrosorption coupling recovery experiments....77
4.2.4. Characterization of composite MoO_3/SnO_2....78
4.2.5. Electrochemical tests....79
4.2.6. Randles-Sevcik....79
4.2.7. Double potential step chronocoulometry....80
4.3. Results and discussion....80
4.3.1. Characterization of composite MoO_3/SnO_2....80
4.3.2. Selective suppression of hydrogen evolution reaction....85
4.3.3. Gallium uptake capacity and electrode evaluation....87
4.3.4. Environment-controlled selective gallium recovery....93
4.3.5. Electro-assisted recovery mechanism....98
4.4. Conclusions....104
4.5. References....104
Chapter 5. Direct electroreduction of platinum group metals on cationic porous carbon electrode....**Error! Bookmark not defined.**

5.1. Introduction..... **Error! Bookmark not defined.**
5.2. Experimental section..... **Error! Bookmark not defined.**
5.2.1. Reagents and materials ..... **Error! Bookmark not defined.**
5.2.2. Fabrication of P/BC electrodes ..... **Error! Bookmark not defined.**
5.2.3. Direct electrochemical reduction experiment **Error! Bookmark not defined.**
5.2.4. Electrode reusability ..... **Error! Bookmark not defined.**
5.2.5. Characterization ..... **Error! Bookmark not defined.**
5.2.6. Electrochemical measurements..... **Error! Bookmark not defined.**
5.2.7. Specific capacitance..... **Error! Bookmark not defined.**
5.3. Results and discussion ..... **Error! Bookmark not defined.**
5.3.1. Characterization of BC and P/BC ..... **Error! Bookmark not defined.**
5.3.2. Electrochemical reduction recovery performance **Error! Bookmark not defined.**
5.3.3. Electrochemical reduction recovery capacity and selectivity of $[PtCl_6]^{2-}$ ..... **Error! Bookmark not defined.**
5.3.4. Cycling stability..... **Error! Bookmark not defined.**
5.3.5. Recovery mechanism..... **Error! Bookmark not defined.**
5.3.6. Recovery of other PGMs ..... **Error! Bookmark not defined.**
5.4. Conclusions..... **Error! Bookmark not defined.**
5.5. References..... **Error! Bookmark not defined.**
Chapter 6. Conclusions..... 113
Appendix I. Articles and patents published during the Ph. D studies 115
Appendix II. Experimental data..... 117

Index of Figures

Fig. 2.1 Classification of critical metals commonly designated by the European Union, the United States, Canada, Australia, and Japan. 5
Fig. 2.2 Relationship between functional end-of-use recycling rates and companionality in global primary metal production. The shaded upper-left quadrant highlights metals with low recycling rates and high companionality, indicating priority targets for resource recovery. 6
Fig. 2.3 (a) Material flow analysis of the Ga cycle. (b-f) Major technologies for Ga separation and recovery. 7
Fig. 2.4 Three possible bonding motifs between amidoxime and Ga ions. 11
Fig. 2.5 Schematic illustration of the preparation and selective recognition mechanism of ion-imprinted materials..... 15
Fig. 2.6 pH-dependent distribution of Ga species. 20
Fig. 2.7 Feasibility of aqueous electrodeposition of different metals based on their standard reduction potentials. 24
Fig. 3.1 The schematic illustration of the fabrication strategy for α-MoO_x/N. 46
Fig. 3.2 (a) XRD patterns of α-MoO_x/N synthesised by hydrothermal synthesis and low-temperature pyrolysis with different amount of EDA; (b) FT-IR spectra of α-MoO_x/N; XPS spectra of α-MoO_x/N-0.53: (c) survey spectra and high-resolution spectra of (d) Mo 3d, (e) N 1s, (f) O 1s; (g) EPR spectra of α-MoO_x and α-MoO_x/N-0.53; SEM images of (h) α-MoO_x, (i) α-MoO_x/N-1.05, (j) α-MoO_x/N-0.53, (k) α-MoO_x/N-0.35 and (l) EDS element mapping images of α-MoO_x/N-0.53 for Mo, O, N, C. 48
Fig. 3.3 N_2 adsorption-desorption isotherm (inset is the pore size distribution) of (a) α-MoO_x, (b) α-MoO_x/N-1.05, (c) α-MoO_x/N-0.53 and (d) α-MoO_x/N-0.35. 50
Fig. 3.4 (a) Adsorption performance of α-MoO_x and α-MoO_x/N for gallium ions at varying pH; (b) variation of pH during adsorption (solid-liquid ratio = 0.3 : 1 g L^{-1}, 50 mg L^{-1} gallium ions, time = 240 min). 51
Fig. 3.5 Water contact angle of (a) α-MoO_x, (b) α-MoO_x/N-1.05, (c) α-MoO_x/N-0.53 and (d) α-MoO_x/N-0.35. 52
Fig. 3.6 (a) Adsorption efficiency and (b) adsorption capacity of different adsorbents for gallium ions (pH = 3.8, 0.3 : 1 g L^{-1}, 50 mg L^{-1} gallium ions, time = 240 min). 52
Fig. 3.7 Zeta potentials of α-MoO_x/N-0.53 obtained at different pH values..... 53
Fig. 3.8 (a) Adsorption efficiencies and selectivity coefficients (k) of α-MoO_x/N-0.53 for Ga^{3+} and coexisting ions In^{3+}, Fe^{3+}, Cr^{3+}, Zn^{2+}, Al^{3+}, Cu^{2+}, Ni^{2+} in binary systems; (b) Adsorption efficiencies of α-MoO_x/N-0.53 for Ga^{3+}, In^{3+}, Fe^{3+}, Cr^{3+}, Zn^{2+}, Al^{3+}, Cu^{2+}, Ni^{2+} in multivariate system; (c) Adsorption efficiencies of Ga^{3+}, Zn^{2+} and Al^{3+} in binary systems of Ga/Zn and Ga/Al (concentration ratios of 1:1, 1:10 and 1:100); (d) Comparison of α-MoO_x/N-0.53 with other gallium adsorbents for $k_{Ga/Zn}$ and $k_{Ga/Al}$. 55
Fig. 3.9 Langmuir (a) and Freundlich (b) isotherm models for adsorption of gallium ions on α-MoO_x/N-0.53. 56

Fig. 3.10 Adsorption performances of α-MoO_x/N-0.53 for different initial concentrations of gallium ions at (a) 298 K, (b) 308 K, and (c) 318 K. 57
Fig. 3.11 (a) Pseudo-first-order kinetic model, (b) pseudo-second-order kinetic model, and (c) intraparticle diffusion model for adsorption of gallium ions on α-MoO_x/N-0.53. 59
Fig. 3.12 (a) Fitting curves of pseudo-second-order kinetic model for the adsorption of gallium ions by α-MoO_x/N-0.53 at different temperatures and (b) fitting curve between lnk_2 and $1/T$. 59
Fig. 3.13 XRD patterns of α-MoO_x/N-0.53 before and after adsorption of gallium ions. 61
Fig. 3.14 (a) FTIR patterns and (b) XPS spectra of α-MoO_x/N-0.53 before and after adsorption of gallium ions; High-resolution XPS spectra of (c) Ga 2p, (d) Ga 3d, (e) Mo 3d, (f) O 1s and (g) N 1s after adsorption. 62
Fig. 3.15 EPR spectra of α-MoO_x/N-0.53 before and after adsorption for gallium ions. 63
Fig. 3.16 (a) Cyclic adsorption performance of gallium ions on α-MoO_x/N-0.53 and desorption efficiency of gallium ions on α-MoO_x/N-0.53 by 0.1 M HNO_3; (b) molybdenum dissolution loss rates during the adsorption and desorption process. 64
Fig. 3.17 SEM images of α-MoOx/N-0.53 (a) before and (b) after adsorption of gallium ions; (c) EDS element mapping images of α-MoO_x/N-0.53 for O, C, N, Mo, Ga after adsorption. 64
Fig. 4.1 (a) Schematic of ion migration driven by electric fields and enrichment at the electrical double-layer interface during CEC process. The electrochemical interface structure is commonly partitioned into five distinct regions: electrode, inner Helmholtz plane (IHP), outer Helmholtz plane (OHP), diffusion layer, and bulk. (b) General electrochemical features of corresponding metals (standard reduction potentials referenced from CRC Handbook of Chemistry and Physics) (c) Configuration of the customized recovery cell. 76
Fig. 4.2 (a) Design of MoO_3/SnO_2 electrode with redox functionality, (b) TEM image, (c) SAED pattern, (d) HRTEM image, (e) TEM image and corresponding elemental mapping of MoO_3/SnO_2-0.50. (f) XRD spectra of MoO_3, SnO_2, MoO_3/SnO_2-0.25, MoO_3/SnO_2-0.50 and MoO_3/SnO_2-0.75. (g) Deconvoluted high-resolution XPS spectra of Mo 3d of MoO_3 and MoO_3/SnO_2-0.50. (h) EPR spectrum of MoO_3/SnO_2-0.50. 81
Fig. 4.3 SEM images of (a) MoO_3, (b) SnO_2, (c) MoO_3/SnO_2-0.25, (d) MoO_3/SnO_2-0.50, (e) MoO_3/SnO_2-0.75 and (f) EDS element mapping images of MoO_3/SnO_2-0.50 for Mo, Sn, O. 82
Fig. 4.4 HRTEM image of MoO_3/SnO_2-0.50. 83
Fig. 4.5 FT-IR spectra of MoO_3, SnO_2, MoO_3/SnO_2-0.25, MoO_3/SnO_2-0.50 and MoO_3/SnO_2-0.75. 83
Fig. 4.6 Deconvoluted high-resolution XPS spectra of (a) Sn 3d and (b) O1s of MoO_3, SnO_2 and MoO_3/SnO_2-0.50. 84
Fig. 4.7 (a) Polarization curves (with iR correction) and (b) CV curves of MoO_3, SnO_2, MoO_3/SnO_2-0.25, MoO_3/SnO_2-0.50 and MoO_3/SnO_2-0.75 electrodes at different applied potentials in gallium-containing electrolyte at a scan rate of 5 mV s^{-1}. (c) Nyquist plots of various electrodes. (d) CV curves of MoO_3/SnO_2-0.50 and graphite substrate electrodes in different electrolytes. 86

Fig. 4.8 (a) Electrochemical recovery performance and (b) current efficiency of gallium in asymmetric CEC systems with different cathodes under constant applied voltage of 1.8 V. (c) Gallium recovery kinetics in traditional adsorption and CEC processes. (d) Gallium recovery performances at various concentrations. (e) Langmuir and Freundlich isotherm models for gallium recovery. (f) Comparison of gallium recovery capacity with previous literatures..... 88
Fig. 4.9 Chronoamperometry tests of (a) MoO_3, (b) SnO_2, (c) MoO_3/SnO_2-0.25, (d) MoO_3/SnO_2-0.50 and (e) MoO_3/SnO_2-0.75 during the gallium recovery process. 89
Fig. 4.10 (a) Nyquist plots of MoO_3/SnO_2-0.50 at different temperatures and (b) fitting curve between lnR_{ct} and $1/T$. 89
Fig. 4.11 Recovery performance of gallium ions at different initial concentrations (pH = 3.0, 100 mL, 1.8 V, 240 min). 90
Fig. 4.12 (a) Cycling gallium recovery performance of the MoO_3/SnO_2-0.50 cathode. (b) Mo and Sn dissolution losses from the cathode during the acid elution process. 91
Fig. 4.13 (a,b) SEM images, corresponding EDS elemental mappings of (c) O, (d) Mo, and (e) Sn, and (f) map sum spectrum of the MoO_3/SnO_2-0.50 cathode before gallium recovery. 92
Fig. 4.14 (a,b) SEM images, corresponding EDS elemental mappings of (c) O, (d) Mo, and (e) Sn, and (f) map sum spectrum of the MoO_3/SnO_2-0.50 cathode after desorption. 93
Fig. 4.15 CV curves of the electrode with 20 consecutive cycles..... 93
Fig. 4.16 (a) Effect of pH on the CEC process of gallium recovery (V = 100 mL, C = 50 mg L^{-1}, t = 240 min). (b) Gallium recovery performances in different electrolytic systems. Stepwise separation efficiencies in (c) the multi-metal solution and (e) the simulated zinc residue leachate, and corresponding selectivity coefficients in (d) and (f), respectively. 94
Fig. 4.17 (a) Real-time monitoring and (b) effect of pH during the gallium recovery process. 95
Fig. 4.18 (a) SEM image and corresponding elemental mapping, (b) XRD spectrum of the anode activated carbon after gallium recover. 95
Fig. 4.19 (a) Effect of charging voltage on the CEC process of gallium recovery. (b) Chronoamperometry tests during gallium recovery under different voltage conditions. 96
Fig. 4.20 Effect of flow rate on the CEC process. 96
Fig. 4.21 (a) Comparison of gallium recovery performance among CEC, adsorption and electrosorption. (b) CV curves of the MoO_3/SnO_2-0.50 electrode at different scan rates. (c) The double potential step chronocoulometry curves, and (d) charge-distribution analysis distinguishing the contributions of specific adsorption and electrical double-layer capacitance for graphite paper and MoO_3/SnO_2-0.50 electrodes. High-resolution XPS spectra of (e) Mo 3d, (f) Sn 3d, (g) Ga 2p, (h) Ga 3d and (i) O 1s after the recovery of gallium. 99
Fig. 4.22 Relationship of I_p and $v^{1/2}$ of the cathodic peak on MoO_3/SnO_2-0.50..... 100
Fig. 4.23 Anson plots of the forward and reverse potential steps in (a, b) graphite paper and (c, d) MoO_3/SnO_2-0.50. 100
Fig. 4.24 XPS spectrum of MoO_3/SnO_2-0.50 after recovery..... 101
Fig. 4.25 Schematic illustration of the electro-assisted gallium capture mechanism at the

MoO_3/SnO_2-0.50 heterointerface. 104

Index of Tables

Table 2.1 Active functional groups, optimal pH, and maximum adsorption capacities (q_{max}) of various adsorbents for Ga recovery 12
Table 2.2 Comparison between the three mass transfer processes 22
Table 3.1 Porous structural parameters for α-MoO_x and α-MoO_x/N 50
Table 3.2 Adsorption isotherm parameters on α-MoO_x/N-0.53 57
Table 3.3 Comparison of the gallium ions adsorption performance by α-MoO_x/N-0.53 and other adsorbents 57
Table 3.4 Adsorption thermodynamics parameters on α-MoO_x/N-0.53 59
Table 3.5 Major elements in simulated zinc slag leachate (mg L^{-1}) 65
Table 4.1 Fitted electrochemical impedance spectroscopy (EIS) parameters of different electrodes 87
Table 4.2 Major elements in simulated zinc residue leachate 98
Table 4.3 Binding energies and relative contents of the components in the high-resolution O 1s XPS spectra after recovery 102

Chapter 1. Introduction

1.1. Justification

Gallium, indium, and platinum group metals (PGMs) possess unique electrical, optical, and catalytic properties, making them indispensable resources for low-carbon energy technologies, advanced electronics, semiconductors, and high-end manufacturing [1,2]. Rapidly growing consumption, coupled with low natural abundance, geographically concentrated supply, and predominant production as by-products of other metals, has intensified concerns over long-term resource security. Industrial process streams, metallurgical effluents, and other secondary aqueous resources are therefore increasingly regarded as important sources for critical-metal recovery [3]. However, these streams typically contain low concentrations of target metals and complex mixtures of coexisting ions, and selective separation becomes even more difficult when different metals exhibit similar aqueous chemistry. Developing innovative recovery technologies and improving recycling rates will be essential to meeting the growing demand for critical metals over the coming decades.

At present, chemical precipitation, solvent extraction, ion exchange, adsorption, and electrodeposition have been widely applied to the recovery of gallium, indium, and platinum group metals [4,5]. Chemical precipitation is operationally simple but often suffers from insufficient selectivity in multicomponent systems. Solvent extraction can achieve high separation efficiency, yet it typically relies on substantial amounts of extractants and organic diluents and may introduce additional environmental burdens. Electrodeposition can directly yield metallic products, but at low concentrations it is readily limited by mass transfer and competing reactions. By contrast, adsorption offers advantages such as relatively low cost, operational flexibility, and environmental compatibility, making it an important approach for recovering critical metals from aqueous media [6]. However, many existing adsorbents still require complicated synthesis procedures and cumbersome regeneration and elution steps. More importantly, conventional adsorption is primarily driven by concentration gradients and is prone to diffusion limitations at low metal concentrations, resulting in slow kinetics and low recovery efficiency. Efficient separation and recovery of gallium, indium, and platinum group metals from dilute aqueous systems thus remain a major challenge.

Chemisorption and electrosorption coupling provides a promising route to

overcoming the aforementioned limitations. An applied electric field can promote ion migration toward the electrode interface, increasing the probability of contact between the target species and active sites, while interfacial chemical interactions can further impart the selectivity required for the separation process [7]. Given that the electroreduction of low-concentration gallium and indium in an aqueous solution is easily limited by hydrogen evolution competition and low current efficiency, selective capture through field-enhanced mass transport coupled with interfacial coordination offers advantages over direct electrodeposition. Recovery performance and selectivity depend strongly on the structural and chemical characteristics of the electrode. Transition-metal oxides and sulfides possess tunable electronic structures and abundant active sites, providing attractive platforms for interfacial recognition and selective regulation of metal ions [8,9]. Molybdenum oxides (MoO_x) and molybdenum disulfide (MoS_2) combine favorable charge-transport properties, structural tunability, and environmental compatibility, warranting further investigation as electrode materials for gallium and indium recovery from aqueous solutions.

For readily reducible PGMs such as platinum, palladium, and rhodium, complexes enriched at the electrode interface can accept electrons and undergo reduction. Chemisorption and electrosorption coupling can therefore be extended from selective ion capture to direct electrochemical reduction and recovery. At low concentrations, efficient recovery depends on enhancing the transport of PGM complexes toward the electrode interface and increasing their local concentration to facilitate subsequent electron injection. Porous carbon materials, characterized by high specific surface area, well-developed pore structures, and good electrical conductivity, provide abundant interfacial reaction sites while enhancing charge storage within the electrical double layer and local ion accumulation [10]. Structural design and interfacial charge regulation of porous carbon are key to enhancing the selective recognition, interfacial transport, and local enrichment of metal complexes, ultimately improving the efficiency of direct electrochemical reduction and recovery.

1.2. Objectives

1.2.1. General objective

The objective is to develop novel molybdenum-based materials and porous carbon materials for the efficient separation and recovery of gallium, indium, and PGMs from dilute aqueous solutions. By tailoring material structure, interfacial properties, and

solution chemistry to regulate chemisorption and electrosorption, this study aims to enhance mass transport, selective recognition, and electrochemical conversion of target metals. The findings provide mechanistic insights and material-design guidance for the sustainable recovery of critical metals from secondary aqueous resources, helping reduce dependence on primary resources and strengthen long-term supply security.

1.2.2. Goals

(1) Enhancing gallium adsorption capacity and selectivity through nitrogen doping and defect engineering of MoO_x. Tuning the electronic structure, surface coordination environment, and defect chemistry creates more accessible binding sites for gallium.

(2) Achieving efficient electro-assisted preferential recovery of gallium from dilute solutions by establishing a favorable bimetallic oxide interface to minimize competing hydrogen evolution and accelerate field-driven gallium transport toward the electrode.

(3) Enabling selective electrochemical separation of gallium and indium by integrating solution speciation control with N-doped MoS_2 interfaces to creat a favorable separation window based on differences in their hydrolysis, complexation, and interfacial coordination behaviors.

(4) Developing cationic porous carbon electrodes for direct electrochemical recovery of PGMs from dilute acidic solutions by coupling interfacial enrichment with electron transfer to improve recovery efficiency and enable direct formation of metallic products.

1.3. References

[1] H. Dong, J. Zhao, J. Chen, Y. Wu, B. Li, Recovery of platinum group metals from spent catalysts: A review, Int. J. Miner. Process. 145 (2015) 108–113. https://doi.org/10.1016/j.minpro.2015.06.009.

[2] K. Zheng, M.F. Benedetti, E.D. van Hullebusch, Recovery technologies for indium, gallium, and germanium from end-of-life products (electronic waste) – A review, J. Environ. Manage. 347 (2023) 119043. https://doi.org/10.1016/j.jenvman.2023.119043.

[3] R.M. DuChanois, N.J. Cooper, B. Lee, S.K. Patel, L. Mazurowski, T.E. Graedel, M. Elimelech, Prospects of metal recovery from wastewater and brine, Nat. Water 1 (2023) 37–46. https://doi.org/10.1038/s44221-022-00006-z.

[4] S. Bao, Q. Huang, B. Chen, Y. Jiang, Hydrometallurgical recovery of gallium from

gallium-containing secondary resources: Leaching, separation and purification, Sep. Purif. Technol. 376 (2025). https://doi.org/10.1016/j.seppur.2025.134068.

[5] H. Zheng, Y. Ding, Q. Wen, B. Liu, S. Zhang, Separation and purification of platinum group metals from aqueous solution: Recent developments and industrial applications, Resour. Conserv. Recycl. 167 (2021). https://doi.org/10.1016/j.resconrec.2021.105417.

[6] L. MacDonald, D. Zhang, A. Karamalidis, Platinum group metals: Key solid phase adsorption technologies for separation from primary and secondary sources, Resour. Conserv. Recycl. 205 (2024) 107590. https://doi.org/10.1016/j.resconrec.2024.107590.

[7] W. Zhan, W. Zhang, Trends in electro-adsorption technologies for rare earth elements recovery: Materials, mechanisms, and future prospects, Chem. Eng. J. 531 (2026). https://doi.org/10.1016/j.cej.2026.174048.

[8] P. Shao, Z. Chang, M. Li, X. Lu, W. Jiang, K. Zhang, X. Luo, L. Yang, Mixed-valence molybdenum oxide as a recyclable sorbent for silver removal and recovery from wastewater, Nat. Commun. 14 (2023) 1362. https://doi.org/10.1038/s41467-023-37143-2.

[9] W. Zhan, X. Zhang, Y. Yuan, Q. Weng, S. Song, M. de J. Martínez-López, J.L. Arauz-Lara, F. Jia, Regulating Chemisorption and Electrosorption Activity for Efficient Uptake of Rare Earth Elements in Low Concentration on Oxygen-Doped Molybdenum Disulfide, ACS Nano 18 (2024) 7298–7310. https://doi.org/10.1021/acsnano.4c00691.

[10] S. Iftekhar, G. Heidari, N. Amanat, E. Nazarzadeh, Z. Muhammad, B. Asif, Porous materials for the recovery of rare earth elements, platinum group metals, and other valuable metals: a review, Springer International Publishing, 2022. https://doi.org/10.1007/s10311-022-01486-x.

Chapter 2. Literature Review

2.1. Introduction

Modern technological development is highly dependent on a secure and reliable supply of critical metals. In recent years, major economies, including the European Union, the United States, Canada, Australia, and Japan, have established and periodically updated lists of critical metals or raw materials [1–5]. The designation of critical metals is based not only on geological availability but also on economic importance, supply concentration, import dependence, substitutability, and vulnerability to supply disruption [6]. Fig. 2.1 summarizes the critical metals commonly designated across these five jurisdictions, including rare earth elements (REEs), platinum group metals (PGMs), lithium (Li), gallium (Ga), and precious metals such as gold (Au) and silver (Ag). The unique physicochemical properties of critical metals impart distinct and often difficult-to-substitute functionalities to materials that allow them to perform effectively in advanced technological applications [7,8]. For example, the global energy transition increasingly relies on sustainably sourced Ga and indium (In) for thin-film solar cells with high conversion efficiency, platinum (Pt) as an essential electrocatalyst in polymer electrolyte fuel cells, and Li, nickel (Ni), and cobalt (Co) for lithium-ion batteries with high energy density. However, the long-term supply of these critical metals and metalloids cannot be assured as available resources become increasingly constrained and ore grades continue to decline.

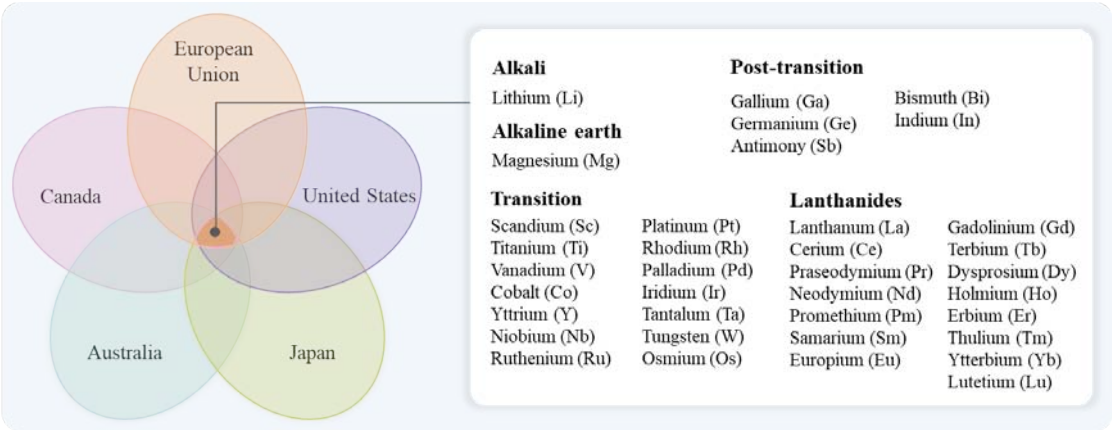


Fig. 2.1 Classification of critical metals commonly designated by the European Union, the United States, Canada, Australia, and Japan.

Developing a circular economy with routine recycling of critical metals is essential to meeting future resource demand. Many critical metals rarely occur in deposits that can be exploited independently and are instead present as companion metals, typically recovered as by-products during the mining and processing of host metals [9–11]. Because companion metals generally contribute only a small fraction of the overall financial return of a mine, their production is largely constrained by the production scale of the corresponding host metals. In addition, some companion metals are used in small quantities and are highly dispersed in compositionally complex products, which further complicates their functional recycling at the end of product life [12]. For example, the functional end-of-life recycling rates of Ga, In, Ge, and REEs are below 1% [6,7]. Industrial wastewater and process streams therefore represent a potential secondary source for the recovery of metals with high companion fractions and low functional recycling rates, which can not only supplement metal supply but also offset wastewater treatment costs and reduce the environmental burden associated with metal discharges [6,13]. In particular, the metals located in the upper-left quadrant of the plot in Fig. 2.2 warrant greater attention for recovery from wastewater because they face particularly high risks of supply shortage [7,14].

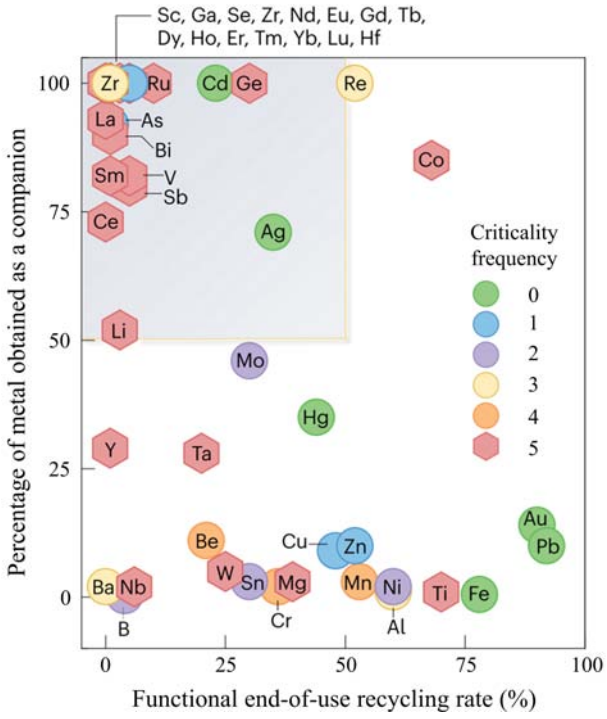


Fig. 2.2 Relationship between functional end-of-use recycling rates and companionality in global primary metal production. The shaded upper-left quadrant

highlights metals with low recycling rates and high companionality, indicating priority targets for resource recovery.

Gallium is a representative by-product metal, and its extraction and recovery are primarily associated with the processing of bauxite and zinc ores [15]. Coal fly ash and electronic waste constitute important secondary sources of Ga, typically characterized by large generation volumes and complex compositions [16]. Hydrometallurgical leaching facilitates the transfer of Ga from the solid phase to the aqueous phase, often accompanied by the co-dissolution of other metals. In addition, approximately 120-170 tons of Ga have been reported to be lost annually during the production of gallium arsenide (GaAs) wafers, integrated circuits, light-emitting diodes, and other Ga-containing products [17]. Ga-containing industrial wastewater generated during hydrometallurgical processing and manufacturing holds considerable potential for resource recovery but remain comparatively underexplored.

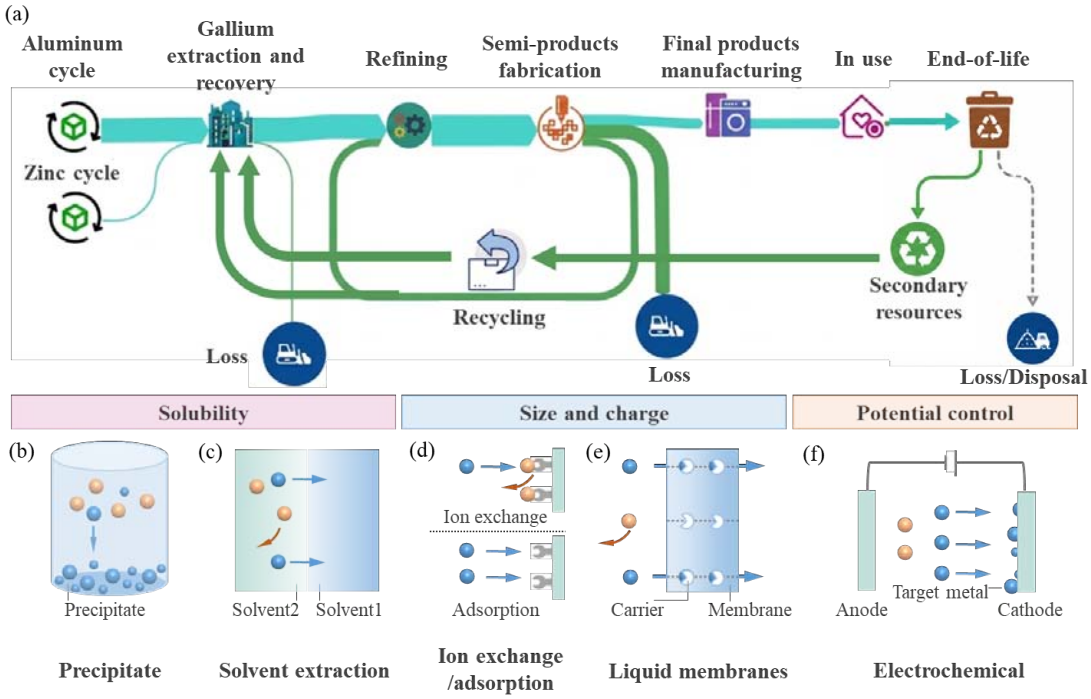


Fig. 2.3 (a) Material flow analysis of the Ga cycle. (b-f) Major technologies for Ga separation and recovery.

Ga is typically present at low concentrations (<50 mg L^{-1}) in industrial wastewater and often coexists with much higher concentrations of competing cations, making its selective separation and effective enrichment particularly challenging [18,19]. Current

methods for Ga separation and recovery mainly include precipitation [20], solvent extraction [21], membrane separation [22], adsorption [23], and electrochemical approaches [24] (Fig. 2.3). Among these methods, adsorption offers operational simplicity, generally requires relatively limited wastewater pretreatment, and can simultaneously achieve separation and enrichment. Moreover, the composition, surface functional groups, and interfacial properties of adsorbents can be readily tailored, providing considerable flexibility for improving Ga selectivity [6,8]. Accordingly, this chapter focuses on the ligand types, solid supports, adsorption performance, selectivity, and adsorption mechanisms reported for Ga separation, followed by an assessment of the major limitations of existing adsorption systems and potential material-design and interfacial-regulation strategies for improving Ga separation and recovery.

2.2. Gallium separation and recovery: Focus on adsorption

The size, charge, and polarizability of metal ions govern their interactions with functional materials and provide an important basis for selective adsorption [7]. Adsorption is considered a promising approach for Ga recovery because of its operational simplicity, relatively low cost, and broad diversity of available material systems. By tailoring the composition and structure of functional ligands and solid supports, adsorbents with specific recognition sites and mass-transfer properties can be developed . In particular, Ga selectivity is largely determined by the chemical nature and spatial configuration of interfacial coordination sites, whereas adsorption kinetics and site utilization are further influenced by specific surface area, pore structure, active-site accessibility, and intraparticle diffusion [23,25–27]. In addition, operating conditions, including pH, temperature, contact time, fluid mixing, competing ions, and other coexisting components, can further affect Ga recovery performance.

2.2.1. Functional ligands for gallium adsorption

2.2.1.1 Nitrogen and oxygen-donor ligands

Nitrogen (N) and oxygen (O) are the most common donor atoms in Ga adsorbents. Functional groups containing these donor atoms, including hydroxyl, carboxyl, carbonyl, amino, imine, and heterocyclic nitrogen groups, together with multidentate ligands containing both N and O donors (Table 2.1), enable selective Ga capture through ion exchange, coordination, and chelation. According to hard and soft acids and bases theory, Ga(III) is a hard Lewis acid and therefore generally exhibits a strong

affinity for hard-base functional groups containing O donor atoms [6,28]. Adsorbents bearing hydroxyl and carboxyl groups have been widely employed for Ga recovery from acidic solutions, where surface hydrogen ions (H^+) can be exchanged with cationic Ga species, including Ga^{3+}, $GaOH^{2+}$, and $Ga(OH)_2^+$, followed by the formation of Ga-O coordination bonds. During Ga(III) adsorption onto iminodiacetic acid-modified corn stalk, deprotonated hydroxyl and carboxyl groups can jointly participate in Ga(III) binding, and the proposed adsorption configurations suggest simultaneous coordination of Ga species with multiple O sites [29]. Similarly, vicinal hydroxyl groups in catechol-derivative-functionalized polymeric resins can form stable bidentate chelate complexes with Ga [26].

N sites with accessible lone-pair electrons can also participate in Ga coordination. Amine, imine, and certain heterocyclic N atoms can serve as potential Lewis-base sites, although the coordination ability is strongly influenced by the electronic structure and protonation state of the N atoms . In acidic media, amine groups are readily protonated, thereby reducing the availability of the lone-pair electrons for direct Ga-N coordination. Graphene oxide functionalized with 4-amino-3-hydrazino-1,2,4-triazol-5-thiol (AHTZT) contains abundant N-, O-, and S-containing groups, among which the N-containing sites were proposed to play a dominant role in enhancing the selective adsorption of Ga^{3+}. At pH 3.0, the N-N bonds in AHTZT remain unprotonated and can selectively interact with Ga^{3+} through electron donor-cation interactions [30]. Under alkaline conditions, $Ga(OH)_4^-$ is captured by Zn^{2+}/quaternary-ammonium/polyamine-modified lignin through a combination of hydrogen bonding, Zn^{2+}-mediated electrostatic attraction, ion exchange between Cl^- and $Ga(OH)_4^-$, and coordination of Ga with -NH- groups. The adsorption capacity increases with increasing pH, reaching a maximum of 289.20 mg g^{-1} [31].

Adsorbents containing both N- and O-functional groups can establish more stable Ga coordination environments through the cooperative action of N/O donor sites. Chelating resins containing an =NOH group together with a second active group, such as =NH, $-NH_2$, -SH, or -OH, have been reported to exhibit strong affinity for Ga [32]. Among these ligands, amidoxime is one of the most representative groups used for Ga recovery. Its oxime (=N-OH) and amino ($-NH_2$) groups are attached to the same carbon atom, allowing multiple metal-binding configurations [33]. Amidoxime-based chelating resins, functional fibers, and composite materials have therefore been widely employed for Ga adsorption from strongly alkaline Bayer liquor [32,34,35]. Metal

binding by amidoxime generally involves the hydroxyl proton dissociation and may proceed through three typical coordination modes (Fig. 2.4): (a) direct coordination of the metal ion to the oxime O atom; (b) N,O-chelation involving the formation of a five-membered ring; and (c) η^2 binding with the N-O bond of oxime [36,37]. In strongly alkaline Bayer liquor, Ga exists predominantly as $Ga(OH)_4^-$. Upon capture by amidoxime sites, H^+ released during oxime deprotonation can combine with OH^- from $Ga(OH)_4^-$ to form H_2O. Density functional theory calculations further indicated that the preferred binding modes for $Ga(OH)_4^-$ adsorption on commercial amidoxime chelating resins were oxygen coordination mode I and chelation mode II [37]. In actual Bayer liquor, an amidoxime porous resin achieved adsorption efficiencies of 93.37% and 91.70% for Ga and V, respectively, followed by the further separation through washing and stepwise desorption [38]. 8-Hydroxyquinoline is another typical bidentate N,O ligand, where the heteroatomic N and the deprotonated phenolic hydroxyl O can simultaneously coordinate with the Ga center to form a stable chelate structure. The immobilization of 8-hydroxyquinoline and its derivatives onto a chitosan-silica support converts the molecular-scale coordination ability into solid-phase Ga separation, enabling the separation of Ga and Al in a simulated Bayer solution [27]. Beyond classical multidentate coordination, N/O donor sites may also act cooperatively through multiple interfacial interactions. For example, in composites consisting of carbon nanotubes (CNTs) and amino-functionalized MIL-53(Fe), $-NH_2$ groups can form hydrogen bonds with hydroxyl-containing Ga species, while amino and carboxyl groups on the surface of the adsorbent further participate in ion exchange and chelation [39]. Overall, individual N- or O-donor groups provide primary interface binding sites, whereas multidentate N/O ligands can further stabilize Ga complexes and enhance interfacial recognition by regulating the electronic properties, spatial arrangement, and local coordination geometry of donor atoms. Accordingly, ligand design for Ga adsorption is shifting from simply increasing the density of functional groups toward precise regulation of the local coordination environment.

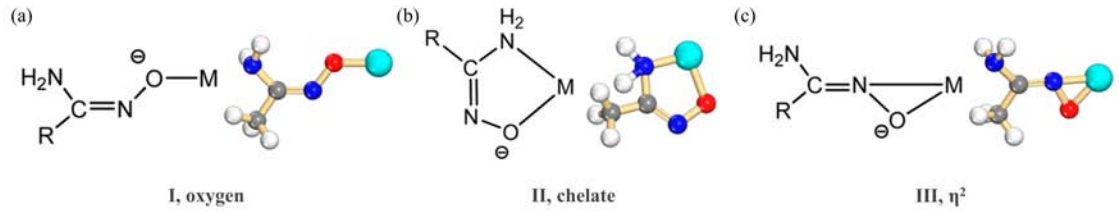


Fig. 2.4 Three possible bonding motifs between amidoxime and Ga ions.

2.2.1.2 Phosphorus-donor ligands

Currently, phosphorus-containing adsorbents for Ga recovery are mainly prepared by loading organic phosphorus extractants used in conventional liquid-liquid extraction onto porous supports such as activated carbon and silica (SiO_2) [40,41]. These synergistic extraction-type adsorbents combine the coordination affinity of organic phosphorus ligands toward Ga with the excellent mass transfer properties of porous supports, while reducing the direct use of organic solvents and the potential pollution risks. Although these materials are typically classified as phosphorus-containing adsorbents, the binding of Ga is actually primarily mediated by O donor atoms in phosphoryl (P=O) groups and dissociable P-OH/P-O^- moieties. Representative acidic organophosphorus extractants include di(2-ethylhexyl)phosphate (P204/D2EHPA), 2-ethylhexyl phosphonic acid mono-2-ethylhexyl ester (P507), and di(2,4,4-trimethylpentyl)phosphinic acid (Cyanex 272) [42,43]. After loading tributyl phosphate (TBP) onto a porous SiO_2-P support, the resulting TBP/SiO_2-P exhibited a Ga adsorption capacity of 22.01 mg g^{-1} in 8 mol L^{-1} HCl, with 95.58% desorption achievable using ultrapure water [44]. In comparison, the co-loading of P507 and TBP onto SiO_2-P significantly enhanced Ga capture capacity in acidic systems. P507-TBP/SiO_2-P achieved a Ga adsorption capacity of 64.2 mg g^{-1} at pH 3.3, with a distribution coefficient exceeding 1600, which was primarily attributed to the joint participation of P-O and P=O groups in Ga coordination [45]. The porous carbon support has expanded the application of organic phosphorous ligands in complex secondary resources [41]. P507@MAC, formed by impregnating mesoporous activated carbon (MAC) with P507, exhibited a Ga^{3+} adsorption capacity of 67.0 mg g^{-1} in leachate from waste Cu-In-Ga-Se (CIGS) photovoltaic modules, outperforming conventional P507-impregnated resins and maintaining relatively stable adsorption performance after six cycles. This excellent Ga capture capacity is ascribed to the abundant mesopores and high specific surface area of MAC, which provide ample adsorption sites for phosphonate groups and metal ions.

In recent years, the design of phosphorus-containing Ga adsorbents has gradually shifted from physical impregnation of extractants toward covalent immobilization of phosphorus-containing functional groups to improve ligand stability and minimize leaching during repeated use [46]. Using ethyl phenylphosphinate (EPP) as a precursor,

phosphoryl functionalities can be covalently introduced onto biomass-derived mesoporous activated carbon through a polydopamine (PDA) interfacial layer to construct EPP-PDA@MAC. When used in the recycling of end-of-life CIGS modules, this material enabled the nearly complete recovery of indium and Ga, with purities of 97.79% and 90.40%, respectively. The adsorption reaction was dominated by coordination between P=O groups and metal ions, while the strong interfacial adhesion of PDA and stable interfacial bonding helped suppress functional-layer loss and enhance cycling stability.

Table 2.1 Active functional groups, optimal pH, and maximum adsorption capacities (q_{max}) of various adsorbents for Ga recovery

Adsorbent	Active functional group	pH	q_{max} (mg g^{-1})	Ref.
4-amino-3-hydrazino1,2,4-triazol-5-thiolmodified graphene oxide	N-N	3.0	23.92	[30]
Ga(III) imprinted bio-adsorbent	-R-NH^{3+}	3.0	192.40	[47]
Zn^{2+}, quaternary ammonium and polyamine embellished lignin	-NH-	9.0	289.20	[31]
Polyurethane foam	-COONH-	6 mol L^{-1} HCl	21.34	[48]
Cellulose-based polyurethane	-COONH-	6 mol L^{-1} HCl	38.43	[49]
Corn stalk modified by iminodiacetic acid	-COOH、-OH	2.8	139.56	[29]
Polyacrylic acid functionalized graphene oxide	-COOH	2.8	196.84	[50]
Catechol derivative functionalized polymeric resins	-OH	3.0	28.71	[26]
Chitosan derived layered porous carbon	-OH	3.0	129.83	[51]
Gallotannin modified carbon nanotube composites	-OH	3.0	170.80	[52]
Mesoporous silica	-OH	3.0	90.00	[53]
Porous silica	Si-OH	3.0	73.88	[54]
Nanosized titanium dioxide	Ti-OH	3.0	2.50	[55]

3D-α-FeOOH	-OH	7.5	52.10	[56]
Persimmon peel-based imprinted material	C-OH, C=O	3.0	352.64	[57]
CNT/UiO-66-NH_2	-COOH, -OH	8.0	925.44	[58]
Hydroxamic acid-functionalized chitosan	C=O, C=N-OH, -OH	4.0	237.88	[59]
Propanediamine-cross linked graphene oxide	-OH, C=N	1.0	370.58	[60]
Amidoxime nanofiber membranes	C=N-OH	12.0	39.80	[35]
Amberlite type XAD7 polymeric resin with L-valine amino acid performance	-NH_2, -COOH	9.0	28.86	[61]
Poly(acrylonitrile)/silica composite	-NH_2, -OH	4.0	63.30	[32]
Magnetic chitosan-based ion-imprinted polymer	-NH_2, -OH	4.0	434.00	[62]
Acrylic modified magnetic chitosan	-NH_2, -NH, COO-, -OH	3.0	183.09	[63]
Dithiourea-bridged cross-linked COF-COF	-NH, -OH	9.0	112.40	[64]
Peptide-encapsulated sodium alginate hydrogel	Imidazole N, C=O, C-O	3.5	127.40	[65]
Pyrrole-polyphenol copolymer	Pyrrolic N, -OH	10.0	380.00	[66]
Ribose-pyrrole-terephthalaldehyde porous organic polymer	Pyrrolic N, -OH	9.0	222.76	[67]
Nitrogen-doped persimmon-powder activated carbon aerogel	C-NH_2, C=N-OH, -COOH, C-OH	11.0	250.69	[68]
Phosphoryl-functionalized waste biomass-derived mesoporous activated carbon	P=O	2.0	140.70	[46]
P507-TBP/SiO_2-P	P-O, P=O	3.3	64.20	[45]

P507-mesoporous activated carbon	P-OH, P=O	2.0	67.00	[41]

2.2.1.3 Ion-imprinting recognition

Ion imprinting technology is a simple and promising strategy for selective separation and enrichment of Ga from complex systems. During the imprinting process, target ions first interact with functional monomers through covalent or noncovalent interactions and are subsequently immobilized within a cross-linked polymer network. The template ions are then removed by physical or chemical means, leaving recognition cavities that are complementary to the target ions in terms of size, coordination geometry, and local chemical environment (Fig. 2.5) [69–71]. Because functional monomers must provide both binding groups capable of interacting with the target metal ions and reactive sites for polymerization or cross-linking, their chemical structure, coordination capability, and mode of incorporation directly influence the binding strength, site homogeneity, and selectivity of the resulting imprinted materials. Tannins are rich in phenolic hydroxyl groups and possess strong coordination and chelating affinity toward metal ions, making them widely used in the construction of metal ion recognition materials [52,72]. Given the high cost associated with the extraction and purification of high-purity tannins [73], tannin-rich biomass resources such as persimmon and bayberry can serve as low-cost functional matrices for the preparation of Ga-imprinted adsorbents [23]. In addition, Ga-imprinted composites and electrochemical sensors have been prepared using multiwalled carbon nanotubes as supporting substrates, together with Ga(III)-8-hydroxyquinoline complexes and β-cyclodextrin as components of the template-recognition system. These materials have been applied to the preconcentration of Ga(III) from coal fly ash samples and the selective detection of Ga(III) in real urine samples, respectively [74,75,76].

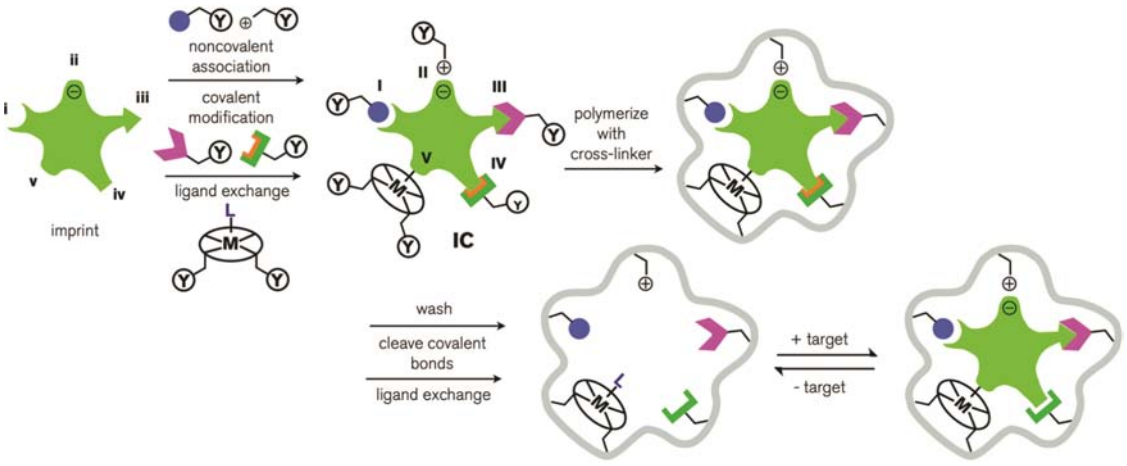


Fig. 2.5 Schematic illustration of the preparation and selective recognition mechanism of ion-imprinted materials.

The spatial recognition provided by ion imprinting is particularly valuable for distinguishing Ga from competing ions such as Al and Zn, which exhibit similar chemical properties, because donor-atom identity and intrinsic coordination affinity alone are often insufficient to achieve high selectivity. Nevertheless, the lack of unified criteria for selecting imprinting systems and optimizing the proportions of template ions, functional monomers, and cross-linkers can lead to limited adsorption capacity, inefficient utilization of recognition sites, difficult desorption, and poor cycling stability [77]. These limitations hinder their practical application and highlight the need for further investigation into the imprinting mechanism and structure-performance relationships [78].

2.2.2. Solid supports

2.2.2.1 Polymer resins

Polymeric resins have been widely employed for Ga adsorption because their porous networks provide high functional-group loading capacity and good chemical stability. Representative commercial resins include Duolite ES-346/345, Purolite A110, A143 Plus, Amberlite XAD7, LSC500, LSC700, and HF582 [26,27,79–81]. However, conventional commercial resins are often limited by slow intraparticle diffusion, competition from coexisting ions, and inefficient regeneration. In recent years, tailoring the degree of cross-linking and pore structure to construct highly porous functional resins has become an effective strategy for improving adsorption and mass-transfer

performance. For example, an amidoxime grafted polyacrylonitrile-styrene-divinylbenzene resin (A-PSD) prepared by suspension polymerization achieved a Ga adsorption capacity of 14.67 mg g^{-1} from Bayer liquor and exhibited favorable mass-transfer performance in dynamic column operation [82]. Acrylonitrile-divinylbenzene copolymers can also be functionalized with hydroxamic acid groups through hydrolysis and subsequent reaction with hydroxylamine, yielding chelating resins with high affinity for Ga [83]. Commercial resins can serve as versatile supports for surface modification. Catechol-derivative-modified Purolite A110 and A143 Plus selectively adsorbed Ga at pH 3, reaching a maximum adsorption capacity of 28.71 mg g^{-1} and showing good resistance to interference from coexisting Al, Zn, and Fe ions [26]. In addition, impregnation of L-valine onto Amberlite XAD7 resulted in a maximum Ga adsorption capacity of 28.88 mg g^{-1} [61]. Beyond the development of new resins, loading sec-octylphenoxy-substituted acetic acid onto microwave-treated waste polymeric resin offers an alternative approach for low-cost Ga recovery under acidic conditions [84].

2.2.2.2 Fibers

Cellulose is an attractive support material for Ga adsorption because of its low cost, abundance, environmental compatibility, and biodegradability. Pristine cellulose generally exhibits limited affinity for Ga and therefore requires chemical functionalization with active groups such as hydroxyl, carboxyl, oxime, and amide groups to enhance the adsorption performance [85]. Polyacrylonitrile (PAN), which contains abundant reactive cyano groups, can undergo nucleophilic addition with hydroxylamine to form amidoxime functionalities and is therefore widely used in the functionalization of fibrous adsorbents [86]. Previous studies have converted PAN fibers into amidoxime-functionalized fibers through heterogeneous reactions. Nevertheless, this process can cause substantial fiber shrinkage and reduce flexibility and mechanical strength [34]. To balance a high degree of functionalization with structural integrity, PAN can first be amidoximated with hydroxylamine hydrochloride, and the resulting spinning solution can then be processed into nanofiber membranes using electrostatic spinning technology, achieving a maximum Ga adsorption capacity of 39.80 mg g^{-1} under alkaline conditions [35]. In addition, natural polyphenols have also been employed for cellulose functionalization. Tannic-acid-functionalized microcrystalline cellulose has been demonstrated to selectively recover Ga(III) and

In(III) from simulated leachates of zinc refinery residues and semiconductor wastes, further extending the applicability of cellulose-based adsorbents to complex Ga-containing wastewater [87].

2.2.2.3 SiO_2

Porous SiO_2 is considered an ideal support for Ga adsorption because of its good acid resistance, large specific surface area, and high porosity. Its surface contains abundant silanol groups (Si-OH), which can serve as potential ion-exchange and functionalization sites for Ga binding and subsequent ligand modification [54]. Incorporating SiO_2 into materials such as PAN and chitosan can further improve the mechanical stability, pore structure, and Ga adsorption performance of the resulting adsorbents [27,32]. In addition, selective extractants can be loaded or impregnated onto porous SiO_2 to combine the selective recognition of Ga by functional ligands with the favorable structural and mass-transfer properties of SiO_2, thereby enabling the development of highly selective Ga adsorbents with good potential for reuse [45].

2.2.2.4 Carbon-based materials

Carbon-based materials have considerable potential for Ga adsorption and enrichment because of their structural diversity, tunable pore architecture, good chemical stability, and ease of functionalization. Representative materials include activated carbon, mesoporous carbon, biomass-derived porous carbon, graphene, and carbon nanotubes. Compared with predominantly microporous activated carbon, mesoporous and hierarchical porous structures can reduce intraparticle diffusion resistance and improve the utilization of adsorption sites. Díez et al. employed disordered mesoporous carbons for the adsorption-desorption preconcentration of Ga from aqueous solutions. Both carbons removed approximately 90% of Ga, while subsequent desorption enabled 82% Ga recovery and an approximately sevenfold preconcentration [88]. The pore structure of carbon materials can also be further tailored through precursor selection and activation. A hierarchical porous carbon, CS-800, prepared from chitosan by hydrothermal carbonization followed by KOH activation, exhibited a specific surface area of 2997 $m^2\ g^{-1}$ and a maximum Ga(III) adsorption capacity of 129.83 mg g^{-1}. The Ga recovery remained above 90% after six adsorption-desorption cycles, demonstrating the beneficial role of hierarchical porosity in Ga enrichment and reusability [51]. In addition, porous carbons derived from biomass wastes such as corn stalks, rice husks, and persimmon peels provide low-cost

feedstocks for the development of Ga adsorbents [29,57,68].

Graphene oxide and its derivatives have also attracted considerable attention due to their high specific surface area and abundant surface -OH and -COOH groups. Under low-pH conditions, however, graphene oxide nanosheets tend to stack and aggregate, which can impair Ga recovery performance. Grafting polyacrylic acid onto graphene oxide improves the dispersion stability under acidic conditions while introducing additional functional sites for Ga binding [50]. Using graphene oxide as the substrate and acrylic acid as a hydrophilic functional monomer, a hydrophilic ion imprinted polymer was prepared and exhibited a maximum Ga adsorption capacity of 221.56 mg g^{-1} [89]. Carbon nanotubes generally require surface functionalization to introduce selective binding sites for Ga. Xiong et al. prepared a gallnut-tannin-modified carbon nanotube composite by a rapid microwave-assisted hydrothermal method, which exhibited good Ga selectivity and reusability [52].

2.2.2.5 Metal-organic frameworks and covalent organic frameworks

Metal-organic frameworks (MOFs) are porous coordination materials formed through the self-assembly of metal ions or metal clusters with organic ligands. The ordered microporous structure of MOF crystals provides abundant and accessible recognition sites, facilitating the diffusion of target ions [58]. In recent years, MOF-based composites have been explored for efficient adsorption and separation of Ga ions, including UiO-66-NH_2 and NH_2-MIL-53(Fe) composites incorporating graphene oxide or carbon nanotubes [39,58,90], as well as tetradentate amidoxime-functionalized MIL-53(Al) nanofiber membranes [25].

Covalent organic frameworks (COFs) are constructed from organic building units linked by covalent bonds and offer a high degree of structural design flexibility. The pore architecture and local chemical properties can be tailored through monomer selection and post-synthetic functionalization, although the application in Ga recovery remains relatively limited. Recently reported dithiourea-bridged COF-COF materials have achieved selective adsorption of Ga(III) by constructing stable porous frameworks containing a high density of N- and O-containing recognition sites, reaching a maximum adsorption capacity of 112.4 mg g^{-1} [64]. Nevertheless, COFs constructed through Schiff-base condensation to form C=N bonds are susceptible to hydrolysis and degradation in aqueous media, particularly under alkaline conditions. Overall, MOFs and COFs offer promising platforms for integrating structural confinement with

selective recognition at the molecular scale, but their practical application remains limited by aqueous stability, processability, and synthesis cost.

2.2.2.6 Metal Oxides

Unlike adsorbents that rely primarily on externally introduced functional groups to provide recognition sites, metal oxides can directly utilize surface hydroxyl groups, lattice oxygen, and coordinatively unsaturated metal sites to interact with Ga species. The adsorption performance can also be modulated by tailoring the crystal phase, particle size, morphology, oxidation state, and defect structure [91]. Metal oxides such as nanosized TiO_2 and FeOOH have been applied to the adsorption of Ga from aqueous solutions, where nanoscale and hierarchical architectures can improve the accessibility of interfacial sites and shorten mass-transfer pathways [55,56]. For semiconducting metal oxides, light irradiation can further regulate the surface electronic state and interfacial adsorption behavior, providing additional opportunities for photo-assisted Ga capture. Previous studies have shown that nanosized TiO_2 with tailored structural and optical properties can exhibit superior Ga adsorption performance compared with commercial TiO_2, further demonstrating the considerable scope for structural regulation of metal oxides toward enhanced Ga adsorption [55].

2.2.3. Adsorption mechanism

2.2.3.1 Electrostatic Interactions

Electrostatic interactions during Ga adsorption are jointly governed by the charge states of aqueous Ga species and the surface charge of the adsorbent, both of which exhibit pronounced pH dependence. Fig. 2.6 illustrates the variation in aqueous Ga(III) speciation with pH based on the hydrolysis constants at 25 °C. Soluble Ga^{3+} predominates at pH < 2.0 [92]. As the pH increases to 3-4, the proportions of $[GaOH]^{2+}$ and $[Ga(OH)_2]^{+}$ progressively increase, accompanied by the possible formation of sparingly soluble $Ga(OH)_3$. In the intermediate pH range, $Ga(OH)_3$ precipitation may interfere with the determination of true adsorption capacity. Therefore, Ga adsorption studies are commonly conducted under acidic or strongly alkaline conditions to minimize the contribution of precipitation. Under strongly alkaline conditions, Ga is mainly present as the anionic species $[Ga(OH)_4]^{-}$ [16].

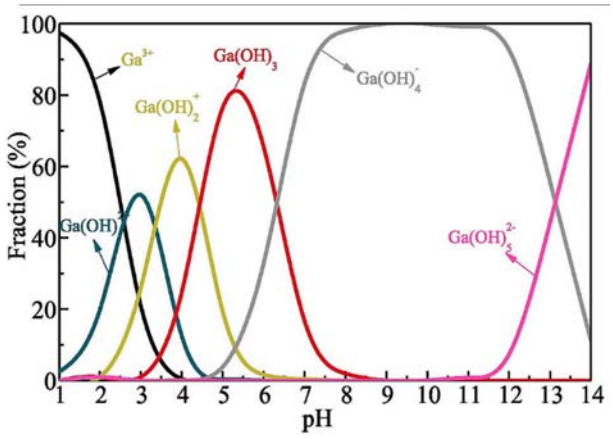


Fig. 2.6 pH-dependent distribution of Ga species.

Within the acidic range, a moderate increase in pH promotes the deprotonation of surface functional groups and weakens competition from H^+ for adsorption sites, thereby enhancing the electrostatic attraction between negatively charged surfaces and cationic Ga species. For example, biogenic elemental tellurium nanoparticles become increasingly negatively charged above the isoelectric point of pH 2.8, accompanied by an increase in Ga adsorption efficiency. The positive shift in zeta potential after Ga loading (from -31 mV to -20 mV) further indicates the involvement of electrostatic attraction in Ga capture [93]. In contrast, under strongly alkaline conditions, electrostatic repulsion can arise between anionic $[Ga(OH)_4]^-$ and negatively charged adsorbent surfaces. The decreased Ga adsorption efficiency of persimmon-peel-based ion-imprinted adsorbents at pH 10-11 has been attributed to this repulsive interaction [23].

2.2.3.2 Chemisorption

Ga chemisorption at adsorbent-solution interfaces predominantly involves coordination bonding and inner-sphere surface complexation. Simultaneous coordination of Ga by two or more donor sites within the same ligand can further generate stable chelate structures, which generally favors enhanced binding selectivity toward Ga. Theoretical calculations indicated that tetradentate amidoxime-functionalized MIL-53(Al) exhibited stronger binding toward Ga than the competing Al and V species examined. The shorter Ga-O coordination distance and more stable coordination configuration were considered important factors underlying its selectivity for Ga [25]. The adsorption kinetics of Ga on peptide-encapsulated sodium alginate hydrogel were well described by the pseudo-second-order model. Combined

spectroscopic characterization showed that, in addition to electrostatic interactions and ion exchange with Ca^{2+}, Ga can form coordination bonds with N/O donor sites in histidine residues along the peptide chains [65]. Similarly, preorganized Schiff-base N/O sites confined within graphene oxide nanochannels can coordinate with Ga^{3+}, thereby enhancing its discrimination against competing ions and yielding selectivity factors of $S_{Ga/Al}$=20 and $S_{Ga/Zn}$=30 in the presence of Al and Zn, respectively [60].

2.2.3.3 Ion exchange

Ion exchange is one of the important mechanisms involved in Ga adsorption and is essentially based on the reversible replacement of exchangeable ions at active sites by dissolved Ga species. Carboxyl, hydroxyl, and organophosphorus groups can provide exchangeable H^+. Therefore, under acidic conditions, cationic Ga species can be immobilized through the replacement of surface H^+ [29,50]. In alkaline solutions, OH^--form anion exchangers such as AN-31 and D-403 have been used for Ga capture, and the exchange process can be represented as R-OH + $[Ga(OH)_4]^-$ → R-$[Ga(OH)_4]$ + OH^- [94]. In addition, other exchangeable ions, including Cl^- and Ca^{2+}, may also participate in ion-exchange processes depending on the type of the fixed charges on the adsorbent and the speciation of Ga, thereby influencing its interfacial binding behavior [31,65].

2.2.4. Current limitations of the gallium adsorption method

Although the adsorption method offers the advantages of simple operation, low energy consumption, and diverse material options, its further application to Ga separation and enrichment remains constrained by several limitations.

(1) Practical Ga-containing solutions commonly contain coexisting components such as Al, Zn, Fe, In, and V. Similarities in hydrolysis and coordination behavior between Ga and metals, particularly Al and In, can lead to competitive adsorption and reduced separation selectivity.

(2) Ga speciation is highly sensitive to pH, and the surface charge of adsorbents and the protonation states of functional groups also vary with solution conditions, resulting in pronounced system-dependent adsorption behavior.

(3) In low-concentration Ga-containing solutions, the mass transfer flux of Ga from the bulk to the adsorbent interface decreases, reducing the effective contact with accessible adsorption sites. Liquid-film mass transfer and intraparticle diffusion can become important factors limiting practical Ga capture.

(4) Some high-performance adsorbents still suffer from complex preparation procedures, loss of active components, insufficient structural stability, and capacity decay during the regeneration cycles.

Adsorption primarily transfers Ga from the liquid phase to the solid phase, and subsequent desorption, concentration, and further conversion are still required to achieve resource recovery. In complex dilute solution systems, optimizing existing adsorbents or developing novel adsorbent materials to simultaneously enhance selective Ga recognition and interfacial mass-transfer efficiency, while reducing downstream desorption and conversion steps, remains a key challenge for the further development of Ga adsorption.

2.3. Electro-assisted gallium adsorption

2.3.1. Chemisorption and electrosorption coupling method

2.3.3.1 Recovery mechanism

For the efficient recovery of Ga from dilute wastewater, an ion-separation platform combining high throughput with high separation factors is required. Electrochemical separation offers several advantages, including fast kinetics, tunable electrode potentials, modular integration, and reusability, making it a promising approach for Ga recovery from dilute solutions [95]. In the field of electrochemical separations, chemisorption and electrosorption coupling method integrates material interfacial affinity with an applied electric field to promote ion transport, interfacial enrichment, and selective immobilization. Electrode polarization facilitates the migration of charged species toward the electrode interface and regulates their distribution within the electrical double layer, while specific binding sites on the electrode material further enable selective recognition and stable binding of target ions.

Table 2.2 Comparison between the three mass transfer processes

Mass-transfer mode	Driving force	Transported species
Diffusion	Concentration gradient	Any species
Electromigration	Electric potential gradient	Charged species
Convection	External force or fluid motion	Any species

Ion mass transfer in electrochemical systems mainly occurs through three mechanisms: diffusion, electromigration, and convection, as summarized in Table 2-2.

Diffusion is the spontaneous transport of a species driven by a concentration gradient. When a spatial concentration difference exists for component *i*, transport occurs from a region of higher concentration to one of lower concentration. According to Fick's first law, the diffusion flux can be expressed as

$$J_{i,\ d} = -D_i \nabla c_i \tag{2.1}$$

where $J_{i,\ d}$ is the diffusion flux of component *i*, mol $cm^{-2}s^{-1}$, D_i is the diffusion coefficient, c_i is the concentration of component *i*, and ∇c_i is the concentration gradient, mol cm^{-4}. The negative sign indicates that diffusion proceeds in the direction opposite to the concentration gradient. In dilute solutions, the concentration difference that can be sustained between the bulk and the interface is limited, making it difficult to maintain a high interfacial mass-transfer flux through diffusion alone.

Electromigration refers to the directional transport of charged species under an applied electric field. Its flux can be expressed in simplified form as

$$J_{i,\ e} = \pm c_i v_i = \pm c_i u_i E \tag{2.2}$$

where $J_{i,\ e}$ is the electromigration flux of component *i*, mol $cm^{-2}s^{-1}$, v_i is the migration velocity, cm s^{-1}, u_i is the ionic mobility, $cm^2\ s^{-1}V^{-1}$ and E is the electric-field strength, V cm^{-1}. The sign depends on the charge of the ion and its migration direction. Electromigration provides an additional directional driving force for charged metal ions and can therefore regulate their transport from the bulk toward the electrode interface.

Convection refers to mass transport arising from the relative motion between different regions of a solution. External stirring is a common means of inducing convection. Convection can alter the solute concentration in the liquid layer adjacent to the electrode surface and thereby influence the transport of species toward the electrode interface. For ion *i*, the convective flux can be expressed as

$$J_{i,\ c} = c_i v_x \tag{2.3}$$

where $J_{i,\ c}$ is the convective flux of component *i*, mol $cm^{-2}s^{-1}$, and v_x is the fluid velocity normal to the electrode surface, cm s^{-1}. Increasing the stirring rate, flow velocity, or electrode rotation rate can reduce the thickness of the diffusion boundary layer and promote mass exchange between the bulk and the electrode interface.

Electro-assisted interfacial enrichment can increase the probability of low-concentration target ions reaching the electrode surface. However, electrostatic interactions within the electrical double layer generally lack sufficient ion specificity, and background electrolytes and coexisting ions may also contribute to interfacial charge compensation. The introduction of chemisorption sites provides a basis for

improving the selectivity. Surface sites with appropriate coordination environments can preferentially bind Ga through coordination, chelation, or surface complexation, thereby immobilizing Ga species transported to the interface by the electric field. The overall recovery performance is jointly governed by Ga speciation, electrode polarity, interfacial charge state, the nature of active sites, and hydrodynamic conditions.

2.3.3.2 Application scope

The chemisorption and electrosorption coupling method has been applied to low-concentration metal systems containing Au(I), Ag(I), Cu(II), Ni(II), La(III), Y(III), and Gd(III), enabling direct interfacial capture of target ions without a separate preconcentration step [96–101]. As shown in Fig. 2.7, the marked differences in reduction potentials among metals give rise to two principal modes of electrochemical recovery. For relatively readily reducible metals, including Au, Ag, Cu, Pt, and Pd, electric-field-enhanced interfacial enrichment can be further coupled with cathodic electron transfer, enabling simultaneous separation and in situ reduction of the target metals. Previous studies have employed porous carbon and MoS_2 electrodes to directly recover low-concentration $[Au(CN)_2]^-$, $[Au(S_2O_3)_2]_3^-$ and Ag^+ through cathodic reduction at applied voltages of 0.6-1.2 V. Recovery efficiencies approaching 100% have been achieved from simulated or actual leachates derived from gold ores and electronic waste, simplifying conventional recovery and reduction processes [100,102]. In contrast, Cu can be further reduced under a constant current of 0.03 A, providing a basis for the stepwise separation of precious and base metals.

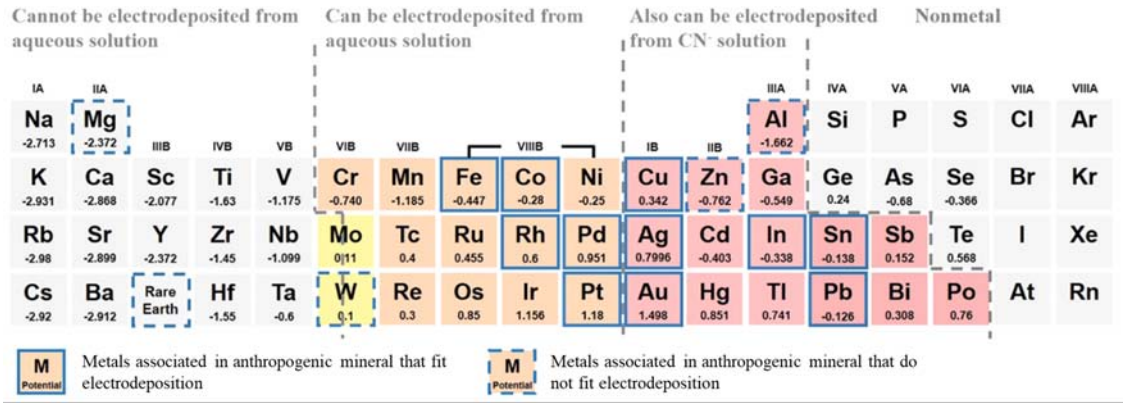


Fig. 2.7 Feasibility of aqueous electrodeposition of different metals based on their standard reduction potentials.

For REEs, Al, Zn, and other metals with relatively negative reduction potentials

[24,103], cathodic reduction is strongly affected by competing hydrogen evolution, resulting in lower current efficiencies for metal electrodeposition. This behavior is particularly pronounced in systems containing rare earth ions. O-doped MoS_2 electrodes have enabled efficient recovery of low-concentration La(III), Gd(III), and Y(III) through the synergistic effects of chemisorption and electrosorption. The different chemisorption behaviors of REEs toward the exposed S and O atoms on O-doped MoS_2 were attributed to differences in their outer-shell electronic configurations [97]. The applied electric field can weaken the limitation imposed by hydration shells on interfacial binding, thereby promoting the selective adsorption of REEs. Similar enhancement of mass transfer and interfacial enrichment has also been achieved using defect-rich MoS_2 and activated carbon-titanium phosphate composite electrodes [98,99]. Ga can undergo electrochemical reduction from aqueous solution under appropriate conditions. However, its relatively negative reduction potential, sluggish reduction kinetics, competition from hydrogen evolution, and mass-transfer limitations at low concentrations all reduce the efficiency of direct electrodeposition. Studies on Cu-In-Cd-Ga systems have shown that the reduction of Ga is markedly slower than that of Cu and In [24]. The hydrogen evolution reaction can be suppressed by introducing inhibitors, but the electrochemical recovery behavior of the metal may also be affected. Overall, the chemisorption and electrosorption coupling method provides a broadly applicable platform for the selective recovery of low-concentration metals with diverse electrochemical properties.

2.3.2. Design principles for electrode materials

The interfacial chemistry, pore structure, and electrochemical characteristics of electrode materials collectively govern the transport, enrichment, and selective binding of target ions, thereby determining the performance of chemisorption and electrosorption coupling systems. Carbon-based materials have been widely employed in electrochemical separations because of their favorable electrical conductivity, developed porous structures, and high specific surface areas [104]. However, ion enrichment in conventional carbon electrodes relies predominantly on charge accumulation within the electrical double layer, providing limited intrinsic ion selectivity. In contrast, redox-active materials introduce Faradaic reactions, ion exchange, and specific chemical interactions into the separation process, allowing ion affinity to be tailored through the chemical identity and local environment of active

sites [105]. Inorganic metal oxides provide a versatile platform for constructing selective electrochemical interfaces. Among them, molybdenum oxides (MoO_x) feature variable Mo valence states, abundant surface oxygen sites, and favorable electron transfer properties, with the interfacial reaction behavior capable of being optimized through the regulation of valence states, defects, and local coordination environments. Mixed-valence MoO_x has been shown to enable Mo(V) to act as an electron donor, allowing captured Ag^+ to be further reduced to metallic Ag. The material exhibited a maximum Ag^+ uptake of 2605.91 mg g^{-1} and achieved 97.9% Ag recovery from complex real wastewater, demonstrating the integration of metal capture and redox conversion within a single material [106]. In addition, incorporation of MoO_3 into biochar enhanced the affinity toward Pb(II) and yielded an adsorption capacity of 229.87 mg g^{-1} despite a decrease in specific surface area, indicating that metal recovery is governed not only by pore structure and surface area but also by interfacial chemical interactions [107].

Beyond providing specific binding sites, redox-active electrodes can couple ion binding with interfacial charge transfer through reversible modulation of the oxidation state of active centers, thereby combining rapid kinetics with high ion-storage capacity within relatively narrow potential windows [108]. Water splitting, however, represents a major parasitic reaction that limits the efficiency of chemisorption and electrosorption coupling. Irrespective of the occurrence of oxygen reduction, this ubiquitous process can be catalyzed on most conductive surfaces once the reduction potential reaches -0.83 V vs. SHE, leading to concomitant hydroxide formation and hydrogen evolution [109]. This parasitic process not only diverts current away from target-ion capture but also perturbs the local pH and interfacial chemical environment, thereby altering ion speciation and recovery performance. Accordingly, effective cathode design requires the suppression of water splitting. Introducing electrochemically active components with suitably tailored redox and interfacial properties can redirect cathodic reactions toward target-ion capture while suppressing competing hydrogen evolution.

Electrode design for chemisorption and electrosorption coupling should balance specific interfacial binding, target ion and electron transport, and controlled electrochemical reactivity. A large specific surface area and high electrical conductivity facilitate mass and charge transport, whereas selective separation mainly relies on the recognition and immobilization of target ions by specific active sites. Appropriate alignment of the operating potential, electrode redox properties, and the

electrochemical stability window of water further helps suppress water splitting and other competing Faradaic reactions. Notably, the loss of active components from the electrodes during repeated polarization cycles, as well as changes in electrode structure, can affect long-term performance, making material immobilization methods and structural stability important considerations in electrode design.

2.4. Summary and perspectives

The rapid technological evolution is driving sustained growth in global demand for Ga, increasing the value of recovering this critical metal from industrial wastewater and other secondary aqueous resources. Ga is typically present at low concentrations in industrial effluents and often coexists with much higher levels of competing metal ions, making its selective separation and effective enrichment particularly challenging. Adsorption is an important approach for Ga separation and recovery from aqueous systems. In recent years, extensive efforts have focused on improving the affinity, selectivity, and mass-transfer performance of Ga adsorbents, leading to the development of diverse material systems, including polymeric resins, fibrous materials, SiO_2-based materials, carbon-based materials, porous frameworks, and ion-imprinted materials. Ga adsorption performance is jointly governed by the chemical nature and spatial configuration of active sites, pore structure, site accessibility, and interfacial mass transfer. Despite substantial progress, practical separation performance remains constrained by mass-transfer limitations at low concentrations, competitive adsorption by coexisting metals, and insufficient cycling stability, indicating that further optimization of both adsorbent materials and separation processes is still required.

Inorganic metal oxides possess tunable surface chemistry and electronic structures, providing a versatile material platform for constructing selective Ga-capture interfaces, particularly MoO_x. Nevertheless, a comprehensive understanding of Ga recovery by metal oxides remains limited, particularly with respect to enhancing Ga recognition and separation through precise regulation of local coordination environments and improving Ga transport to the interface under low-concentration conditions by optimizing hierarchical and accessible transport pathways. As Ga recovery increasingly targets more dilute and compositionally complex aqueous streams, chemisorption and electrosorption coupling offers a promising strategy by combining electric-field-driven ion transport with selective interfacial capture. Rational control of electrode composition, interfacial properties, and operating potential can further enhance the

rapid enrichment and preferential capture of low-concentration Ga.

2.5. References

[1] Gian Andrea Blengini, Study on the EU's List of Critical Raw Materials 2020. https://doi.org/https://op.europa.eu/ en/publication-detail/-/publication/c0d5292a-ee54-11ea-991b- 01aa75ed71a1/language-en.

[2] J. Nakano, The Geopolitics of Critical Minerals Supply Chains (CSIS,2021). https://doi.org/https://www.csis.org/analysis/geopolitics-critical- minerals-supply-chains.

[3] Canada's Critical Minerals List 2021 (Government of Canada, 2021). https://doi.org/https://www.nrcan.gc.ca/our-natural-resources/minerals-mining/critical-minerals/23414.

[4] Australian Critical Minerals Prospectus 2021 (Australian Government, 2021). https://doi.org/https://www.austrade.gov.au/news/publications/australian-critical-minerals-prospectus-2021.

[5] Final List of Critical Minerals 2018 (Federal Register, US Department of the Interior, 2018). https://doi.org/https://www.federalregister.gov/documents/2018/05/18/2018-10667/final-list-of-critical-minerals-2018.

[6] J.P.H. Perez, K. Folens, K. Leus, F. Vanhaecke, P. Van Der Voort, G. Du Laing, Progress in hydrometallurgical technologies to recover critical raw materials and precious metals from low-concentrated streams, Resour. Conserv. Recycl. 142 (2019) 177–188. https://doi.org/10.1016/j.resconrec.2018.11.029.

[7] R.M. DuChanois, N.J. Cooper, B. Lee, S.K. Patel, L. Mazurowski, T.E. Graedel, M. Elimelech, Prospects of metal recovery from wastewater and brine, Nat. Water 1 (2023) 37–46. https://doi.org/10.1038/s44221-022-00006-z.

[8] S. Bao, Q. Huang, B. Chen, Y. Jiang, Hydrometallurgical recovery of gallium from gallium-containing secondary resources: Leaching, separation and purification, Sep. Purif. Technol. 376 (2025). https://doi.org/10.1016/j.seppur.2025.134068.

[9] H. Song, C. Wang, B. Sen, G. Liu, China Factor: Exploring the Byproduct and Host Metal Dynamics for Gallium-Aluminum in a Global Green Transition, Environ. Sci. Technol. 56 (2022) 2699–2708. https://doi.org/10.1021/acs.est.1c04784.

[10] A.N. Løvik, E. Restrepo, D.B. Müller, Byproduct Metal Availability Constrained by Dynamics of Carrier Metal Cycle: The Gallium-Aluminum Example, Environ. Sci.

Technol. 50 (2016) 8453–8461. https://doi.org/10.1021/acs.est.6b02396.

[11] N.T. Nassar, T.E. Graedel, E.M. Harper, By-product metals are technologically essential but have problematic supply, Sci. Adv. 1 (2015). https://doi.org/10.1126/sciadv.1400180.

[12] T.E. Graedel, Report, Recycling Rates of Metals—A Status, n.d. https://doi.org/https://wedocs.unep.org/handle/20.500.11822/8702.

[13] S. Lin, M. Hatzell, R. Liu, G. Wells, X. Xie, Mining resources from water, Resour. Conserv. Recycl. 175 (2021) 105853. https://doi.org/10.1016/j.resconrec.2021.105853.

[14] T.E. Graedel, B.K. Reck, A. Miatto, Alloy information helps prioritize material criticality lists, Nat. Commun. 13 (2022). https://doi.org/10.1038/s41467-021-27829-w.

[15] Z. Han, Q. Liu, X. Ouyang, H. Song, T. Gao, Y. Liu, B. Wen, T. Dai, Tracking two decades of global gallium stocks and flows: A dynamic material flow analysis, Resour. Conserv. Recycl. 202 (2024) 107391. https://doi.org/10.1016/j.resconrec.2023.107391.

[16] F. Lu, T. Xiao, J. Lin, Z. Ning, Q. Long, L. Xiao, F. Huang, W. Wang, Q. Xiao, X. Lan, H. Chen, Resources and extraction of gallium: A review, Hydrometallurgy 174 (2017) 105–115. https://doi.org/10.1016/j.hydromet.2017.10.010.

[17] A.N. Løvik, E. Restrepo, D.B. Müller, The global anthropogenic gallium system: Determinants of demand, supply and efficiency improvements, Environ. Sci. Technol. 49 (2015) 5704–5712. https://doi.org/10.1021/acs.est.5b00320.

[18] R. Jain, S. Fan, P. Kaden, S. Tsushima, H. Foerstendorf, R. Barthen, F. Lehmann, K. Pollmann, Recovery of gallium from wafer fabrication industry wastewaters by Desferrioxamine B and E using reversed-phase chromatography approach, Water Res. 158 (2019) 203–212. https://doi.org/10.1016/j.watres.2019.04.005.

[19] S. Rao, D. Wang, Z. Liu, K. Zhang, H. Cao, J. Tao, Selective extraction of zinc, gallium, and germanium from zinc refinery residue using two stage acid and alkaline leaching, Hydrometallurgy 183 (2019) 38–44. https://doi.org/10.1016/j.hydromet.2018.11.007.

[20] S. Saikia, R.B. Costa, A. Sinharoy, M.P. Cunha, M. Zaiat, P.N.L. Lens, Selective removal and recovery of gallium and germanium from synthetic zinc refinery residues using biosorption and bioprecipitation, J. Environ. Manage. 317 (2022) 115396. https://doi.org/10.1016/j.jenvman.2022.115396.

[21] L. Cui, L. Feng, H. Yuan, H. Cheng, F. Cheng, Efficient recovery of aluminum, lithium, iron and gallium from coal fly ash leachate via coextraction and stepwise

stripping, Resour. Conserv. Recycl. 202 (2024). https://doi.org/10.1016/j.resconrec.2023.107380.

[22]H. Zhou, K. Huang, Extraction and separation of low-concentration Ga (III) in concentrated hydrochloric acid using supported liquid membrane via controlling the dissociation behavior of GaCl4- ions at interface, Chem. Eng. Res. Des. 186 (2022) 1–12. https://doi.org/10.1016/j.cherd.2022.07.046.

[23]L. Gao, L. Wang, Y. Cao, S. Li, Persimmon peel-based ion-imprinted adsorbent with enhanced adsorption performance of gallium ions, Miner. Eng. 176 (2022) 107354. https://doi.org/10.1016/j.mineng.2021.107354.

[24]Q. Song, L. Zhang, C. Yang, Z. Xu, Novel Electrodeposition Method for Cu-In-Cd-Ga Sequential Separation from Waste Solar Cell: Mechanism, Application, and Environmental Impact Assessment, Environ. Sci. Technol. 55 (2021) 10724–10733. https://doi.org/10.1021/acs.est.1c02496.

[25]C. Shi, K. Wang, C. Chen, Y. Cao, G. Zhou, J. Wang, C. Li, Highly selective capture of gallium from aqueous solutions using tetradentate amidoxime functionalized MIL-53(Al) nanofiber membranes, Sep. Purif. Technol. 330 (2024). https://doi.org/10.1016/j.seppur.2023.125303.

[26]P. Raj, M. Patel, A.K. Karamalidis, Chemically modified polymeric resins with catechol derivatives for adsorption, separation and recovery of gallium from acidic solutions, J. Environ. Chem. Eng. 11 (2023) 110790. https://doi.org/10.1016/j.jece.2023.110790.

[27]J. Roosen, S. Mullens, K. Binnemans, Chemical immobilization of 8-hydroxyquinoline and 8-hydroxyquinaldine on chitosan-silica adsorbent materials for the selective recovery of gallium from Bayer liquor, Hydrometallurgy 171 (2017) 275–284. https://doi.org/10.1016/j.hydromet.2017.05.026.

[28]M. Fomina, G.M. Gadd, Biosorption: Current perspectives on concept, definition and application, Bioresour. Technol. 160 (2014) 3–14. https://doi.org/10.1016/j.biortech.2013.12.102.

[29]Y. Zhang, L. Zhu, Y. Wang, Z. Lou, W. Shan, Y. Xiong, Y. Fan, Preparation of a biomass adsorbent for gallium(III) based on corn stalk modified by iminodiacetic acid, J. Taiwan Inst. Chem. Eng. 91 (2018) 291–298. https://doi.org/10.1016/j.jtice.2018.05.030.

[30]X. Zhu, Y. Guo, B. Zheng, Preparation of 4-Amino-3-hydrazino-1,2,4-triazol-5-thiol-Modified Graphene Oxide and Its Greatly Enhanced Selective Adsorption of

Gallium in Aqueous Solution, Molecules 29 (2024). https://doi.org/10.3390/molecules29122778.

[31] S. Fang, B. Zhang, W. Li, J. Ke, Adsorption of Ga(III) by Zn2+, quaternary ammonium and polyamine embellished lignin with the crosslinking agent of epichlorohydrin, Int. J. Biol. Macromol. 310 (2025). https://doi.org/10.1016/j.ijbiomac.2025.143108.

[32] S. Lu, L. Chen, M.F. Hamza, C. He, X. Wang, Y. Wei, E. Guibal, Amidoxime functionalization of a poly(acrylonitrile)/silica composite for the sorption of Ga(III) – Application to the treatment of Bayer liquor, Chem. Eng. J. 368 (2019) 459–473. https://doi.org/10.1016/j.cej.2019.02.094.

[33] K. Saeed, S. Haider, T.J. Oh, S.Y. Park, Preparation of amidoxime-modified polyacrylonitrile (PAN-oxime) nanofibers and their applications to metal ions adsorption, J. Memb. Sci. 322 (2008) 400–405. https://doi.org/10.1016/j.memsci.2008.05.062.

[34] T. Yang, L. Wang, M. Liang, Y. Chen, H. Zou, Cross-linked polyvinyl amidoxime fiber: a highly selective and recyclable adsorbent of gallium from Bayer liquor, Iran. Polym. J. (English Ed. 27 (2018) 589–597. https://doi.org/10.1007/s13726-018-0635-4.

[35] Z. Qin, Y. Liao, Z. Wang, S. Wang, L. Song, K. Ma, D. Luo, H. Yue, Innovative Amidoxime Nanofiber Membranes for Highly Effective Adsorption of Ga(III) from Waste Bayer Solution, Ind. Eng. Chem. Res. 62 (2023) 11140–11150. https://doi.org/10.1021/acs.iecr.3c01410.

[36] A. Nilchi, R. Rafiee, A.A. Babalou, Adsorption behavior of metal ions by amidoxime chelating resins, Macromol. Symp. 274 (2008) 101–108. https://doi.org/10.1002/masy.200851414.

[37] H. Long, Z. Zhao, Y. Chai, X. Li, Z. Hua, Y. Xiao, Y. Yang, Binding mechanism of the amidoxime functional group on chelating resins toward Gallium(III) in bayer liquor, Ind. Eng. Chem. Res. 54 (2015) 8025–8030. https://doi.org/10.1021/acs.iecr.5b01835.

[38] L. Qu, L. Li, Y. Wu, F. Liu, Y. Wang, Study on the Adsorption Mechanism and Desorption Process of Gallium and Vanadium in Practical Bayer Liquor by Amidoxime Porous Resin, Jom 77 (2025) 3457–3471. https://doi.org/10.1007/s11837-025-07205-5.

[39] C. Li, C. Zhou, D. French, I.T. Graham, Z. Wang, Y. Li, F. Wang, G. Liu, Synthesis of a carbon nanotube-modified NH2-MIL-53(Fe) adsorbent and efficient adsorption and separation of gallium ions, J. Mater. Chem. A 13 (2025) 19864–19877.

https://doi.org/10.1039/d5ta02348c.

[40] J.H. Chen, Y.H. Chang, K.C. Hsu, J.C. Lin, Extraction of Ga(III) by Di-(2-ethylhexyl)phosphoric acid (D2EHPA)-Modified XAD-4 Resins Prepared by Solvent-Nonsolvent Modification, Chem. Eng. Technol. 44 (2021) 2257–2268. https://doi.org/10.1002/ceat.202100226.

[41] W. Wang, X. Xu, D. Lai, Q. Xu, J. Li, Y. Wang, Selective isolation of gallium and indium from waste photovoltaic modules facilitated by extractant-mesoporous activated carbon composites, Sep. Purif. Technol. 330 (2024) 125510. https://doi.org/10.1016/j.seppur.2023.125510.

[42] X. Zhang, Z. Zhang, J. Fu, G. Zhou, G. Li, Y. Cao, G. Fan, P. Li, D. Teng, Toward circular Gallium: Recovery pathways from Bayer Liquor, red Mud, fly Ash, and e-waste, Waste Manag. 218 (2026) 115543. https://doi.org/10.1016/j.wasman.2026.115543.

[43] Z. Zhao, L. Cui, Y. Guo, H. Li, F. Cheng, Recovery of gallium from sulfuric acid leach liquor of coal fly ash by stepwise separation using P507 and Cyanex 272, Chem. Eng. J. 381 (2020) 122699. https://doi.org/10.1016/j.cej.2019.122699.

[44] J.J. Meng, C.L. He, J. Zhou, T. Fujita, S.Y. Ning, Y.Z. Wei, Recovery of gallium by silica-based polymer TBP/SiO2-P obtained from hydrochloric acid solution, J. Appl. Polym. Sci. 138 (2021) 49732. https://doi.org/10.1002/app.49732.

[45] J. Meng, C. He, Y. Li, J. Zhou, J. Li, C. Zheng, J. Zhao, T. Fujita, S. Ning, Y. Wei, Enhanced adsorption and separation of gallium using silica-based P507-TBP/SiO2–P adsorbent from sulfuric acid solution, Microporous Mesoporous Mater. 314 (2021) 110859. https://doi.org/10.1016/j.micromeso.2020.110859.

[46] W. Wang, X. Xu, J. Li, T. Liu, H. Wang, Y. Wang, Green and facile modification of mesoporous activated carbon for selective indium and gallium recovery from waste photovoltaic modules, Green Chem. 27 (2024) 485–497. https://doi.org/10.1039/d4gc04204b.

[47] Y. Wang, L. Zhu, Y. Song, Z. Lou, W. Shan, Y. Xiong, Novel chitosan-based ions imprinted bio-adsorbent for enhanced adsorption of gallium(III) in acidic solution, J. Mol. Liq. 320 (2020) 114413. https://doi.org/10.1016/j.molliq.2020.114413.

[48] S. Yang, J. Qiao, C. Kang, M. Sun, S. Dong, Y. Zhao, W. Sun, Y. Yang, C. Duan, Study on the preparation of polyurethane foam and adsorption of gallium ions in gangue acid leach solution, Mater. Today Commun. 43 (2025). https://doi.org/10.1016/j.mtcomm.2025.111563.

[49] S. Yang, K. Lou, L. Luo, X. Zhao, B. Li, C. Duan, M. Sun, C. Kang, L. Wang, J.

Qiao, Preparation of cellulose-based polyurethane adsorbent by crude glycerol enhanced composite liquefaction system: Efficient synthesis and gallium adsorption mechanism, Colloids Surfaces A Physicochem. Eng. Asp. 748 (2026). https://doi.org/10.1016/j.colsurfa.2026.141022.

[50] Y. Zhang, X. Liu, Y. Wang, Z. Lou, W. Shan, Y. Xiong, Polyacrylic acid-functionalized graphene oxide for high-performance adsorption of gallium from aqueous solution, J. Colloid Interface Sci. 556 (2019) 102–110. https://doi.org/10.1016/j.jcis.2019.08.032.

[51] J. Cui, X. Cong, X. Li, X. Chen, Y. Wang, J. Gao, Y. Xiong, Chitosan derived layered porous carbon and its performance on gallium adsorption, J. Chem. Technol. Biotechnol. 98 (2023) 1387–1394. https://doi.org/10.1002/jctb.7355.

[52] Y. Xiong, X. Cui, M. Zhang, Y. Wang, Z. Lou, W. Shan, Microwave hydrothermal synthesis of gallotannin/carbon nanotube composites for the recovery of gallium ion, Appl. Surf. Sci. 510 (2020) 145414. https://doi.org/10.1016/j.apsusc.2020.145414.

[53] I. Protsak, M. Stockhausen, A. Brewer, M. Owton, T. Hofmann, F. Kleitz, Enhanced selective extraction of indium and gallium using mesoporous sorbents, Chem. Eng. J. 498 (2024). https://doi.org/10.1016/j.cej.2024.154468.

[54] X. Liao, L. Shi, X. Qiu, S. Qin, X. Huang, D. Liang, X. Li, Porous silica with high specific surface area derived from calcium silicate for highly selective adsorption of gallium from acidic solutions, Colloids Surfaces A Physicochem. Eng. Asp. 744 (2026). https://doi.org/10.1016/j.colsurfa.2026.140624.

[55] I.B. Dorosheva, P. V. Kel, N. V. Pechishcheva, I.D. Popov, S.A. Petrova, A.A. Rempel, Nanosized titanium dioxide modification for gallium ions photoadsorption, J. Alloys Compd. 1010 (2025). https://doi.org/10.1016/j.jallcom.2024.177537.

[56] X. Wu, M. Yuan, X. Guo, L. Zhang, Fast Coadsorption and Selective Separation of Gallium(III) and Germanium(IV) from Aqueous Solutions by 3D Hierarchical Porous Hoya-like α-FeOOH, ACS Sustain. Chem. Eng. 7 (2019) 15939–15947. https://doi.org/10.1021/acssuschemeng.9b02199.

[57] N. Chai, L. Gao, S. Li, Y. Cao, Z. Ma, L. Li, M. Hu, In-suit ion-imprinted bio-sorbent with superior adsorption performance for gallium(III) capture, J. Clean. Prod. 387 (2023) 135861. https://doi.org/10.1016/j.jclepro.2023.135861.

[58] W. Li, C. Zhou, C. Li, W. Zhu, J. Shi, G. Liu, Synthesis of CNT/UiO-66-NH2 adsorbent and the selective adsorption of gallium in solution, Sep. Purif. Technol. 323 (2023) 124464. https://doi.org/10.1016/j.seppur.2023.124464.

[59]Y. Guo, M. Ma, Q. Gong, G. Li, G. Zhou, G. Fan, Y. Cao, P. Li, D. Teng, Sustainable gallium recovery using functionalized chitosan-based adsorbents: Comparative evaluation of single and multiple hydroxamic acids on adsorption capacity and selectivity, Sep. Purif. Technol. 366 (2025). https://doi.org/10.1016/j.seppur.2025.132772.

[60]C. Li, M. Qiu, C. Shi, F. Qiu, Q. He, Z. Li, W. Li, J. Wang, G. Zhou, Construction of Schiff-base binding site in confined 2D nanochannels for efficient gallium adsorption, Desalination 637 (2026). https://doi.org/10.1016/j.desal.2026.120438.

[61]C. Vancea, L. Ciocarlie, A. Negrea, G. Mosoarca, M. Ciopec, N. Duteanu, P. Negrea, B. Pascu, N.S. Nemes, Evaluation of Functionalized Amberlite Type XAD7 Polymeric Resin with L-Valine Amino Acid Performance for Gallium Recovery, Polymers (Basel). 16 (2024). https://doi.org/10.3390/polym16060837.

[62]D. Teng, C. Liu, L. Ma, P. Jin, G. Fan, P. Li, Y. Cao, W. Wang, Selective adsorption of Ga(III) from aqueous solutions using magnetic chitosan-based ion-imprinted polymers: Synthesis optimization and mechanistic insights, Int. J. Biol. Macromol. 298 (2025). https://doi.org/10.1016/j.ijbiomac.2025.139957.

[63]M. Dang, J. Yin, M. Wu, C. Liu, Study on the preparation of a novel acrylic modified magnetic chitosan adsorbent and the adsorption behavior on Ga (III), Sep. Purif. Technol. 358 (2025). https://doi.org/10.1016/j.seppur.2024.130245.

[64]J. Luo, Y. Wu, D. Xiang, S. Wang, J. Ye, H. Liu, L. Zhang, Dithiourea-bridged cross-linked COF-COF for efficient and selective gallium recovery, Sep. Purif. Technol. 387 (2026). https://doi.org/10.1016/j.seppur.2025.136690.

[65]Y. Liu, Z. Xin, L. Tian, D. Villa-Gomez, W. Wang, Y. Cao, Fabrication of peptide-encapsulated sodium alginate hydrogel for selective gallium adsorption, Int. J. Biol. Macromol. 263 (2024) 130436. https://doi.org/10.1016/j.ijbiomac.2024.130436.

[66]H. Yuan, S. Wang, Y. Wu, J. Luo, X. Ding, Y. Chen, X. Yang, X. Tang, G. Luo, Design of a Pyrrole–Phenol Copolymer Adsorbent with Ultrahigh Capacity and Reusability for Efficient Ga(III) Capture, ACS Appl. Polym. Mater. (2026). https://doi.org/10.1021/acsapm.6c01536.

[67]H. Yuan, J. Luo, S. Wang, Y. Wu, X. Ding, Y. Chen, H. Liu, S. Yan, One-step synthesized ribose-pyrrole-terephthalaldehyde porous organic polymer with synergistic O/N coordination for exceptionally selective and recyclable Ga(III) adsorption, Sep. Purif. Technol. 402 (2026). https://doi.org/10.1016/j.seppur.2026.138684.

[68]J. Fan, L. Gao, S. Li, N. Chai, D. Lei, Efficient recovery of gallium(Ⅲ) from

alkaline solution by electrosorption using biomass-derived carbon aerogel electrodes, Sep. Purif. Technol. 353 (2025) 128297. https://doi.org/10.1016/j.seppur.2024.128297.

[69] G. Yuan, H. Tu, J. Liu, C. Zhao, J. Liao, Y. Yang, J. Yang, N. Liu, A novel ion-imprinted polymer induced by the glycylglycine modified metal-organic framework for the selective removal of Co(II) from aqueous solutions, Chem. Eng. J. 333 (2018) 280–288. https://doi.org/10.1016/j.cej.2017.09.123.

[70] N.B. Mabaso, P.N. Nomngongo, L. Nyaba, Recent Advances in Synthesising and Applying Magnetic Ion-Imprinted Polymers to Detect, Pre-Concentrate, and Remove Heavy Metals in Various Matrices, Processes 12 (2024). https://doi.org/10.3390/pr12081601.

[71] Y. Chen, X. Ma, J. Peng, Highly selective removal and recovery of Ni(II) from aqueous solution using magnetic ion-imprinted chitosan nanoparticles, Carbohydr. Polym. 271 (2021). https://doi.org/10.1016/j.carbpol.2021.118435.

[72] C. Cheng, M. Jia, L. Cui, Y. Li, L. Xu, X. Jin, Adsorption of Cr(VI) ion on tannic acid/graphene oxide composite aerogel: kinetics, equilibrium, and thermodynamics studies, Biomass Convers. Biorefinery 12 (2022) 3875–3885. https://doi.org/10.1007/s13399-020-00899-4.

[73] L. Guo, T. Qiang, Y. Ma, L. Ren, T. Dai, Purification and characterization of hydrolysable tannins extracted from Coriaria nepalensis bark using macroporous resin and their application in gallic acid production, Ind. Crops Prod. 162 (2021) 113302. https://doi.org/10.1016/j.indcrop.2021.113302.

[74] Z. Zhang, H. Zhang, Y. Hu, X. Yang, S. Yao, Novel surface molecularly imprinted material modified multi-walled carbon nanotubes as solid-phase extraction sorbent for selective extraction gallium ion from fly ash, Talanta 82 (2010) 304–311. https://doi.org/10.1016/j.talanta.2010.04.038.

[75] Y. Hu, Z. Zhang, H. Zhang, L. Luo, M. Zhang, X. Yang, S. Yao, Electrochemical sensor for sensitive determination of Ga(III) ion based on β-cyclodextrin incorporated multi-walled carbon nanotubes and imprinted sol-gel composite film, Chinese J. Chem. 30 (2012) 377–385. https://doi.org/10.1002/cjoc.201180474.

[76] L. Chen, X. Wang, W. Lu, X. Wu, J. Li, Molecular imprinting: Perspectives and applications, Chem. Soc. Rev. 45 (2016) 2137–2211. https://doi.org/10.1039/c6cs00061d.

[77] T. Jiang, P. Wang, Z. Liu, W. Zhang, F. Liu, C. Liao, Unconventional technologies for the separation of germanium and gallium from solutions: A review, Sep. Purif.

Technol. 377 (2025). https://doi.org/10.1016/j.seppur.2025.134399.

[78]X. Zhou, B. Wang, R. Wang, Insights into ion-imprinted materials for the recovery of metal ions: Preparation, evaluation and application, Sep. Purif. Technol. 298 (2022) 121469. https://doi.org/10.1016/j.seppur.2022.121469.

[79]F. Lu, T. Xiao, J. Lin, A. Li, Q. Long, F. Huang, L. Xiao, X. Li, J. Wang, Q. Xiao, H. Chen, Recovery of gallium from Bayer red mud through acidic-leaching-ion-exchange process under normal atmospheric pressure, Hydrometallurgy 175 (2018) 124–132. https://doi.org/10.1016/j.hydromet.2017.10.032.

[80]S. Li, W. Wu, H. Li, X. Hou, The direct adsorption of low concentration gallium from fly ash, Sep. Sci. Technol. 51 (2016) 395–402. https://doi.org/10.1080/01496395.2015.1102282.

[81]Z. Zhao, X. Li, Y. Chai, Z. Hua, Y. Xiao, Y. Yang, Adsorption Performances and Mechanisms of Amidoxime Resin toward Gallium(III) and Vanadium(V) from Bayer Liquor, ACS Sustain. Chem. Eng. 4 (2016) 53–59. https://doi.org/10.1021/acssuschemeng.5b00307.

[82]Z. Qin, S. Wang, S. Zhang, J. Xie, C. an Zhou, C. Wang, L. Song, K. Ma, D. Luo, H. Yue, Cross-linked amidoxime porous resin for selective gallium separation in Bayer solutions: Reaction mechanism and kinetic study, Chem. Eng. J. 481 (2024). https://doi.org/10.1016/j.cej.2023.148340.

[83]P. Selvi, M. Ramasami, M.H.P. Samuel, R. Sripriya, K. Senthilkumar, P. Adaikkalam, G.N. Srinivasan, Gallium Recovery from Bayer's Liquor Using Hydroxamic Acid Resin, J. Appl. Polym. Sci. 92 (2004) 847–855. https://doi.org/10.1002/app.20047.

[84]C. He, Y. Liu, C. Zheng, Y. Liao, T. Fujita, Y. Wei, G. Wang, S. Ma, Utilization of an amidoxime resin waste to prepare solvent-impregnated resins (CA−12/SIRs) for the extraction of Ga(III) from acid solutions, J. Environ. Chem. Eng. 11 (2023). https://doi.org/10.1016/j.jece.2023.110871.

[85]W. Guo, J. Zhang, F. Yang, F. Tan, Z. Zhao, Highly efficient and selective recovery of gallium achieved on an amide-functionalized cellulose, Sep. Purif. Technol. 237 (2020) 116355. https://doi.org/10.1016/j.seppur.2019.116355.

[86]W. Zhang, C. Xu, X. Che, T. Wang, S. Willför, M. Li, C. Li, Encapsulating Amidoximated Nanofibrous Aerogels within Wood Cell Tracheids for Efficient Cascading Adsorption of Uranium Ions, ACS Nano 16 (2022) 13144–13151. https://doi.org/10.1021/acsnano.2c06173.

[87]J. Du, M. Zhang, Z. Dong, X. Yang, L. Zhao, Facile fabrication of tannic acid functionalized microcrystalline cellulose for selective recovery of Ga(III) and In(III) from potential leaching solution, Sep. Purif. Technol. 286 (2022). https://doi.org/10.1016/j.seppur.2022.120442.

[88]E. Díez, J.M. Gómez, A. Rodríguez, I. Bernabé, J. Galán, Recovery of Gallium from Aqueous Solution through Preconcentration by Adsorption/Desorption on Disordered Mesoporous Carbon, J. Sustain. Metall. 7 (2021) 227–242. https://doi.org/10.1007/s40831-021-00336-4.

[89]M. Zhang, X. Zhang, C. Liang, L. Qin, D. Fu, M. Wang, Y. Bai, W. Liu, X. Liu, Preparation of graphene-based surface ion-imprinted adsorbent for Ga(Ⅲ) selective extraction from acid leaching of fly ash, Sep. Purif. Technol. 325 (2023) 124681. https://doi.org/10.1016/j.seppur.2023.124681.

[90]W. Li, C. Zhou, C. Li, W. Zhu, J. Shi, G. Liu, Synthesis of UiO-66 series metal–organic framework composites and the adsorption effect on gallium, Chem. Eng. J. 455 (2023). https://doi.org/10.1016/j.cej.2022.140881.

[91]N. Wang, J. Li, F. Jia, H. Zhou, Y. Xie, P. Chen, S. Song, M. Quintana, Unraveling nitrogen-doped and vacancy-engineered synergistically modified molybdenum oxide promoting gallium selective adsorption, Sep. Purif. Technol. 358 (2025) 130158. https://doi.org/10.1016/j.seppur.2024.130158.

[92]S.A. Wood, I.M. Samson, The aqueous geochemistry of gallium, germanium, indium and scandium, Ore Geol. Rev. 28 (2006) 57–102. https://doi.org/10.1016/j.oregeorev.2003.06.002.

[93]S. Saikia, A. Sinharoy, P.N.L. Lens, Adsorptive removal of gallium from aqueous solution onto biogenic elemental tellurium nanoparticles, Sep. Purif. Technol. 286 (2022) 120462. https://doi.org/10.1016/j.seppur.2022.120462.

[94]K. Bagdaulet, A. Kuralai, G. Sergei, A. Yerkezhan, Sorption Extraction of Gallium from Alumina-Alkaline Solutions, Trans. Indian Inst. Met. 77 (2024) 919–929. https://doi.org/10.1007/s12666-023-03219-2.

[95]X. Su, H.J. Kulik, T.F. Jamison, T.A. Hatton, Anion-Selective Redox Electrodes: Electrochemically Mediated Separation with Heterogeneous Organometallic Interfaces, Adv. Funct. Mater. 26 (2016) 3394–3404. https://doi.org/10.1002/adfm.201600079.

[96]P. Li, Y. Gui, D.J. Blackwood, Development of a Nanostructured α-MnO2/Carbon Paper Composite for Removal of Ni2+/Mn2+ Ions by Electrosorption, ACS Appl. Mater. Interfaces 10 (2018) 19615–19625. https://doi.org/10.1021/acsami.8b02471.

[97] W. Zhan, X. Zhang, Y. Yuan, Q. Weng, S. Song, M. de J. Martínez-López, J.L. Arauz-Lara, F. Jia, Regulating Chemisorption and Electrosorption Activity for Efficient Uptake of Rare Earth Elements in Low Concentration on Oxygen-Doped Molybdenum Disulfide, ACS Nano 18 (2024) 7298–7310. https://doi.org/10.1021/acsnano.4c00691.

[98] W. Zhan, Y. Yuan, Q. Weng, Y. Pan, S. Song, J.L. Arauz-Lara, F. Jia, W. Zhang, Enhanced trace gadolinium(III) extraction via tailored chemisorption on defect-engineered molybdenum disulfide electrodes, Chem. Eng. J. 512 (2025) 162632. https://doi.org/10.1016/j.cej.2025.162632.

[99] H. Zhu, J. Li, H. Zhang, Z. Wang, N. Wang, C. Wang, F. Jia, S. Song, Coordination-mediated interfacial enrichment for efficient extraction of ultra-dilute rare earth ions via high-density affinity sites electrode, Chem. Eng. J. 521 (2025) 166678. https://doi.org/10.1016/j.cej.2025.166678.

[100] D. Wang, Y. Liang, Y. Zeng, C. Liu, C. Zhan, P. Chen, S. Song, F. Jia, Highly selective recovery of gold and silver from E-waste via stepwise electrodeposition directly from the pregnant leaching solution enabled by the MoS2 cathode, J. Hazard. Mater. 465 (2024) 133430. https://doi.org/10.1016/j.jhazmat.2024.133430.

[101] X. Zhang, W. Zhan, Q. Weng, S. Wang, S. Song, L. Arauz-lara, F. Jia, Electro reduction-recovery of Au(S2O3)23– within a low concentration range via multi-porous activated carbon electrodes, Sep. Purif. Technol. 354 (2025) 129134. https://doi.org/10.1016/j.seppur.2024.129134.

[102] Q. Weng, W. Zhan, X. Zhang, S. Song, Z. Zeng, H.M. Lwin, J.L. Arauz-Lara, F. Jia, Electrochemical reduction and recovery of trace gold(I) from environmentally friendly thiosulfate leaching solutions using carbon electrodes, Carbon N. Y. 232 (2025) 119799. https://doi.org/10.1016/j.carbon.2024.119799.

[103] S. Trasatti, Work function, electronegativity, and electrochemical behaviour of metals. III. Electrolytic hydrogen evolution in acid solutions, J. Electroanal. Chem. 39 (1972) 163–184. https://doi.org/10.1016/S0022-0728(72)80485-6.

[104] J. Fan, L. Gao, S. Li, N. Chai, D. Lei, Efficient recovery of gallium(Ⅲ) from alkaline solution by electrosorption using biomass-derived carbon aerogel electrodes, Sep. Purif. Technol. 353 (2025). https://doi.org/10.1016/j.seppur.2024.128297.

[105] X. Su, T.A. Hatton, Redox-electrodes for selective electrochemical separations, Adv. Colloid Interface Sci. 244 (2017) 6–20. https://doi.org/10.1016/j.cis.2016.09.001.

[106] P. Shao, Z. Chang, M. Li, X. Lu, W. Jiang, K. Zhang, X. Luo, L. Yang, Mixed-valence molybdenum oxide as a recyclable sorbent for silver removal and recovery

from wastewater, Nat. Commun. 14 (2023) 1362. https://doi.org/10.1038/s41467-023-37143-2.

[107] Y. Li, S.M. Shaheen, M. Azeem, L. Zhang, C. Feng, J. Peng, W. Qi, J. Liu, Y. Luo, Y. Peng, E.F. Ali, K. Smith, J. Rinklebe, Z. Zhang, R. Li, Removal of lead (Pb+2) from contaminated water using a novel MoO3-biochar composite: Performance and mechanism, Environ. Pollut. 308 (2022) 119693. https://doi.org/10.1016/j.envpol.2022.119693.

[108] X. Su, K.J. Tan, J. Elbert, C. Rüttiger, M. Gallei, T.F. Jamison, T.A. Hatton, Asymmetric Faradaic systems for selective electrochemical separations, Energy Environ. Sci. 10 (2017) 1272–1283. https://doi.org/10.1039/c7ee00066a.

[109] M.G. Walter, E.L. Warren, J.R. McKone, S.W. Boettcher, Q. Mi, E.A. Santori, N.S. Lewis, Solar water splitting cells, Chem. Rev. 110 (2010) 6446–6473. https://doi.org/10.1021/cr1002326.

Chapter 3. Nitrogen-doped and vacancy-engineered molybdenum oxide for selective gallium adsorption

3.1. Introduction

Sophisticated high-tech applications such as integrated circuits and optoelectronic devices are critically dependent on the strategic and critical raw material gallium, already extensively used in diodes, photodetectors, solar cells, aerospace applications, industrial, medical and telecommunication equipment [1,2]. The ever-increasing demand for technology is driving the demand for gallium, with global demand for gallium resources projected to exceed 700 tons by 2025 [1,3,4]. Notably, the scarcity and fine-grained nature of gallium render it extremely difficult to mineralize, and gallium mainly exists in the form of hosted minerals in bauxite, coal and zinc ores, commonly recovered as the by-product of mineral processing [5,6]. Growing market demand and limited natural resources have triggered a dynamic global competition for gallium resources, propelled by the non-substitutability of gallium with high-efficiency optical excitation and high electron mobility.

The efficient extraction of low-grade gallium from secondary sources such as Bayer solution, aluminum slag, fly ash, zinc slag and waste electronics has been the essential means of alleviating the supply-demand imbalance in the gallium market [3,7]. Numerous methods are devoted to the recovery of gallium, such as precipitation [8], solvent extraction [2,9], ion exchange [10], electrochemical method [11,12] and adsorption [13–16]. Graded precipitation and tannic acid precipitation methods have triggered the demand for new technologies for their drawbacks such as the generation of secondary pollution, high consumption of tannic acid and poor selectivity. Solvent extraction method based on the extraction of gallium into organic phase by cation exchange mechanism plays the important role for the recovery of gallium in industry, yet the volatilization of toxic organic solvents poses a threat to the environment. Although ion-exchange resins (e.g. commercial amidoxime resins) exhibit affinity and high selectivity for gallium, elution difficulty and high cost have limited the development. Mercury cathodic electrolysis has been forbidden in numerous countries owing to the high toxicity [6]. Adsorption, as a simple, efficient and economically feasible method, has attracted much attention in the recovery of gallium-containing

wastewater. To selectively recover gallium, considerable attempts have been undertaken to establish specific interactions between gallium ions and adsorbents. For example, imprinted multi-walled nanotubes and perspex ion-imprinted adsorbents participated in selective adsorption of gallium by constructing specific cavities matched to gallium ions [14,17]. The synergistic interaction of organics diethanolamine [18], amide [19] and amidoxime [16] with natural cellulose enhanced the adsorption properties of gallium ions and probably involved the binding of gallium ions in solution to protonated oxygen atoms, the formation of cyclic chelates of gallium ions with oxime-based oxygen and amine-based nitrogen, and the formation of η^2 bonds of gallium ions with oxygen and nitrogen on the oxime group. The potential of poly(acrylic acid)-modified graphene oxide with a high density of carboxyl groups for the recovery of gallium ions verified that the carboxyl and hydroxyl groups could attract positively charged gallium ions ($Ga(OH)_2^+$, $Ga(OH)^{2+}$, or Ga^{3+}) via ion exchange and chelation [20]. Despite the good selectivity of these adsorbents for the adsorption of gallium ions, the shortcomings such as cumbersome preparation process, poor adsorption capacity for low concentrations (<100 mg L^{-1}), and complex post-treatment procedures of the eluent prone to secondary contamination, triggered an urgent need for highly efficient, environmentally friendly gallium adsorbents that can selectively recover gallium from complex solutions.

Molybdenum oxide (α-MoO_x) with low toxicity has been used as the absorbents for wastewater treatment and resource recovery due to the unique nanoscale size and high specific surface area. The structural and functional adjustability allow α-MoO_x to realize various adsorption applications. The introduction of oxygen vacancies can provide electron donors, which can enhance the adsorption activity and reaction rate [21]. Amorphous α-MoO_x exposes richer *OH, *O and *OOH active sites and larger specific surface area, which facilitates the adsorption of metal ions, as confirmed in a closed-loop silver recovery study of amorphous α-MoO_x [22]. It has been reported that the main binding groups of gallium ions are hydroxyl and carboxyl groups, etc., and the ligand atom is oxygen [23], so the abundant oxygen-containing active sites in α-MoO_x could be predicted to be conducive to the adsorption of gallium ions. Additionally, designing stable adsorbents is the critical step in boosting the economic and environmental benefits as well as the widespread applicability of adsorbents. Amine molecules can be used as complexing agents or structural anisotropies owing to the excellent chelating ability with several transition metal ions, and non-metal nitrogen-

doping achieved by post-annealing treatment has been reported to contribute significantly to the enhancement of chemical stability, electrochemical properties and the adsorption of metal cations (e.g., Pt^{4+}) [24–26]. However, limited information is available regarding the adsorption processes and mechanism of nitrogen-doped and vacancy-engineered synergistically modified molybdenum oxide (α-MoO_x/N) on strategic metal gallium.

Herein, α-MoO_x/N was proposed as the efficient adsorbent for selective recovery of gallium in acidic systems containing multiple coexisting ions (Cu^{2+}, Zn^{2+}, Al^{3+}, Ni^{2+}, In^{3+}, Fe^{3+}, Cr^{3+}). The adsorption mechanism of gallium ions captured by α-MoO_x/N was elucidated by combining adsorption isotherms, adsorption kinetics, and X-ray diffraction (XRD), fourier transform infrared spectroscopy (FTIR), X-ray photoelectron spectroscopy (XPS), electron paramagnetic resonance (EPR) analyses. In addition, the evaluation of the cyclic stability of α-MoO_x/N further demonstrated the potential for practical applications. The results may provide insights for establishing the efficient recovering industry and promoting the low-carbon and sustainable development of the gallium industry chain.

3.2. Experimental section

3.2.1. Reagents and materials

Ammonium molybdate tetrahydrate ($(NH_4)_6Mo_7O_{24}•4H_2O$) and 1,2-Ethylenediamine (EDA, $C_2H_8N_2$) and gallium standard solution (1000 μg ml^{-1} in 1mol L^{-1} HCl) were purchased from Aladdin Co., Ltd (Shanghai, China). All the other chemicals and organic solvents were purchased from Sinopharm Chemical Reagent Co., Ltd, China and were of analytical grade or higher.

3.2.2. Syntheses of α-MoO_x and α-MoO_x/N

The α-MoO_x/N was synthesized by the hybrid strategy of hydrothermal synthesis and low-temperature pyrolysis [27,28]. 1 M HCl was added dropwise to 15 mL of the aqueous solution containing ammonium molybdate tetrahydrate ($(NH_4)_6Mo_7O_{24}•4H_2O$, 1 mmol) and ethylenediamine (EDA, 14 mmol) under magnetic stirring at room temperature until observing the white precipitate (pH = 5). And the reaction was sustained at 50 ℃ for 3 h. Upon filtration, the product was washed with ethanol and exposed to oven at 60 ℃ for drying to obtain the precursor $(C_2H_{10}N_2)Mo_3O_{10}$.

Subsequently, the precursor was placed in the tube furnace and heated to 370 °C at a rate of 1 °C min^{-1} under argon atmosphere for 5 h and then cooled naturally. The method employed EDA as the nitrogen source, with the advantages of safety, cost-effectiveness and simplicity of operation. Meanwhile, $(NH_4)_6Mo_7O_{24}•4H_2O$ and EDA with varying Mo/EDA molar ratios (0, 1.05, 0.53, 0.35) were added to regulate the nitrogen loading of α-MoO_x nanowires. The α-MoO_x/N with different EDA levels were denoted as α-MoO_x/N-x.

3.2.3. Adsorption experiment

The synthesized 30 mg of α-MoO_x/N was added to 100 mL of nitric acid system containing 1-200 mg L^{-1} gallium ions, adjusting the pH (2.0, 2.5, 3.0, 3.4, 3.8) of the solutions with sodium hydroxide or dilute nitric acid. The batch adsorption experiments were carried out under natural light with stirring for 240 min at 250 rpm. The reaction suspensions obtained at different time intervals were filtered through 0.22 μm filter membranes, and the analysis of gallium ion concentration based on atomic absorption spectrophotometry (AAS, Shimadzu AA-6680, Japan) was performed to evaluate the adsorption capacities of the synthesized absorbents.

The adsorption efficiency and capacity were calculated from the initial concentration of metal ions (C_0, mg L^{-1}), the concentration of metal ions after 4h of adsorption (C_e, mg L^{-1}), the volume of solution (V, L) and the mass of adsorbent (m, g) by using the following Eq. 3.1 and Eq. 3.2, respectively.

$$A = \frac{(C_0 - C_e)}{C_0} \times 100\% \tag{3.1}$$

$$q_e = \frac{(C_0 - C_e)V}{m} \tag{3.2}$$

Adsorption isotherms for gallium ions were fitted using the Langmuir (Eq. 3.3)and Freundlich model (Eq. 3.4).

$$q_e = \frac{q_{max} b C_e}{1 + bC_e} \tag{3.3}$$

$$\log q_e = \log K_f + \frac{1}{n} \log C_e \tag{3.4}$$

Where q_{max} was the maximum adsorbed value of metal ion on the adsorbate; b was the Langmuir adsorption constant related to the binding energy. By plotting log versus $\log q_e$, the constant K_f and the exponent $1/n$ could be calculated.

Dynamic adsorption of α-MoO_x/N-0.53 on gallium ions were fitted using pseudo-first-order kinetic (Eq. 3.5), pseudo-second-order kinetic (Eq. 3.6) and intraparticle

diffusion model (Weber-Morris model, Eq. 3.7).

Pseudo-first-order model:

$$q_t = q_e \times \left(1\text{-}e^{-k_1 t}\right) \tag{3.5}$$

Pseudo-second-order model:

$$\frac{t}{q_t} = \frac{1}{k_2 q_e^2} + \frac{t}{q_e} \tag{3.6}$$

Where q_t and q_e (mg·g^{-1}) were the adsorption capacity of gallium ions at time t (min) and the final equilibrium; k_1 and k_2 were the rate constant of pseudo-first-order model and pseudo-second-order model, respectively.

Intra-particle diffusion model:

$$q_t = k_3 \times t^{1/2} + C \tag{3.7}$$

Where q_t was the same as above; k_3 was the rate constant of the intraparticle diffusion model; C (mg·g^{-1}) was a constant revealing the number of boundary layers of the adsorbent.

Activation energy (E_a, kJ mol^{-1}) reflects the strength of the interaction of the adsorbent with metal ions and whether the adsorption process is a physical or chemical reaction, usually calculated using the Arrhenius equation:

$$ln\, k = ln\, A - \frac{E_a}{RT} \tag{3.8}$$

where A is the preexponential factor; T (K) represents the temperature; and R is the ideal gas constant (8.314 J mol^{-1} K^{-1}).

The adsorption thermodynamics of α-MoO_x/N-0.53 on gallium was studied at different temperatures (298-318 K), including free energy of adsorption (ΔG^0), enthalpy change (ΔH^0) and entropy of adsorption (ΔS^0) which can be obtained from the following Eq. (3.9) and Eq. (3.10).

$$\Delta G^0 = \Delta H^0 - T \times \Delta S^0 \tag{3.9}$$

$$lnk = \Delta S^0/R - \Delta H^0/(RT) \tag{3.10}$$

Where k is the equilibrium constant, q_e is the concentration of gallium ions on α-MoO_x/N-0.53 at equilibrium (mg g^{-1}), C_e is the equilibrium concentration of gallium ions in solution (mg L^{-1}).

3.2.4. Selective adsorption

Competitive adsorption was performed using coexisting metal ions (i.e., Cu^{2+}, Zn^{2+}, Al^{3+}, Ni^{2+}, In^{3+}, Fe^{3+}, Cr^{3+}) from the Gallium-polluted wastewater. Binary

solutions and multivariate solution were employed to evaluate the selectivity of α-MoO_x/N. The concentrations of each metal ion in the binary and multivariate solutions were 50 mg L^{-1} and 20 mg L^{-1}, respectively. Distribution coefficient k_d was calculated from the initial concentration of metal ions (C_0, mg L^{-1}), the equilibrium concentration (C_e, mg L^{-1}), the volume of solution (V, mL) and the mass of adsorbent (m, mg) by using the following Eq. 3.11:

$$k_d = \frac{(C_0 - C_e)V}{mC_e} \tag{3.11}$$

The adsorption selectivity of gallium ions in the existence of other metal ions could be represented by the selection coefficient k as shown in the following Eq. 3.12:

$$k = \frac{k_{d1}}{k_{d2}} \tag{3.12}$$

where k_{d1} and k_{d2} are the distribution coefficients for gallium ions and another competing metal ion, respectively.

3.2.5. Circulation recovery of gallium

For the recyclability test, α-MoO_x/N of adsorbed gallium was immersed in 0.1 M HNO_3 solution for 1 h. The regenerated adsorbent was reused in the next cycle of the adsorption batch experiment containing 50 mg L^{-1} gallium ions. The stability of α-MoO_x/N was investigated by detecting the concentration of molybdenum and nitrogen in solution after adsorption. The dissolution loss rates of molybdenum and nitrogen were calculated according to Eq. 3.13:

$$\text{Dissolution loss rate} = \frac{C \times V}{m \times w} \times 100 \tag{3.13}$$

where C (g L^{-1}) is the concentration of molybdenum or nitrogen in the circulating solution, V (L) and m (g) are the same as above, and w (%) is the mass fraction of molybdenum or nitrogen in α-MoO_x/N.

3.2.6. Characterizations

The measurements of metal ions concentrations were carried out using the Inductively Coupled Plasma-Optical Emission Spectrometer (ICP-OES, Agilent 5110, American) and Atomic Absorption Spectrophotometry (AAS, Shimadzu AA-6680, Japan). The surface morphology of samples α-MoO_x and α-MoO_x/N was observed using a JSM-IT300 scanning electron microscope (SEM, JEOL, Japan). The crystal structure and chemical composition of samples were characterised by X-ray diffractometer of Cu Kα radiation (XRD, Rigaku SmartLab SE, Japan), X-ray

photoelectron spectroscopy (XPS, Thermo Scientific K-Alpha, USA), and Fourier transform infrared spectroscopy (FTIR, Thermo Scientific Nicolet iS20, USA). Electron paramagnetic resonance (EPR, Bruker EMXplus-6/1, Germany) test was performed to obtain information on oxygen vacancies. And zeta potential analyser (Malvern Zetasizer Nano ZSE) was employed to obtain the surface potential of α-MoO_x/N nanowires at varying pH.

3.3. Results and discussion

3.3.1. Characterization of α-MoO_x and α-MoO_x/N

To avoid the formation of metal nanoparticles and agglomerates, α-MoO_x/N nanowires were obtained by low-temperature pyrolysis (370 °C) of hydrothermally synthesized precursor $(C_2H_{10}N_2)Mo_3O_{10}$ under argon atmosphere (Fig. 3.1). The prevailing consensus is that the unoccupied 4d orbital of the Mo atom from MoO_x can establish covalent Mo-N bonds with the lone pairs of electrons on the N atoms of organic molecules [29], making the interface between MoO_x and EDA tightly bound.

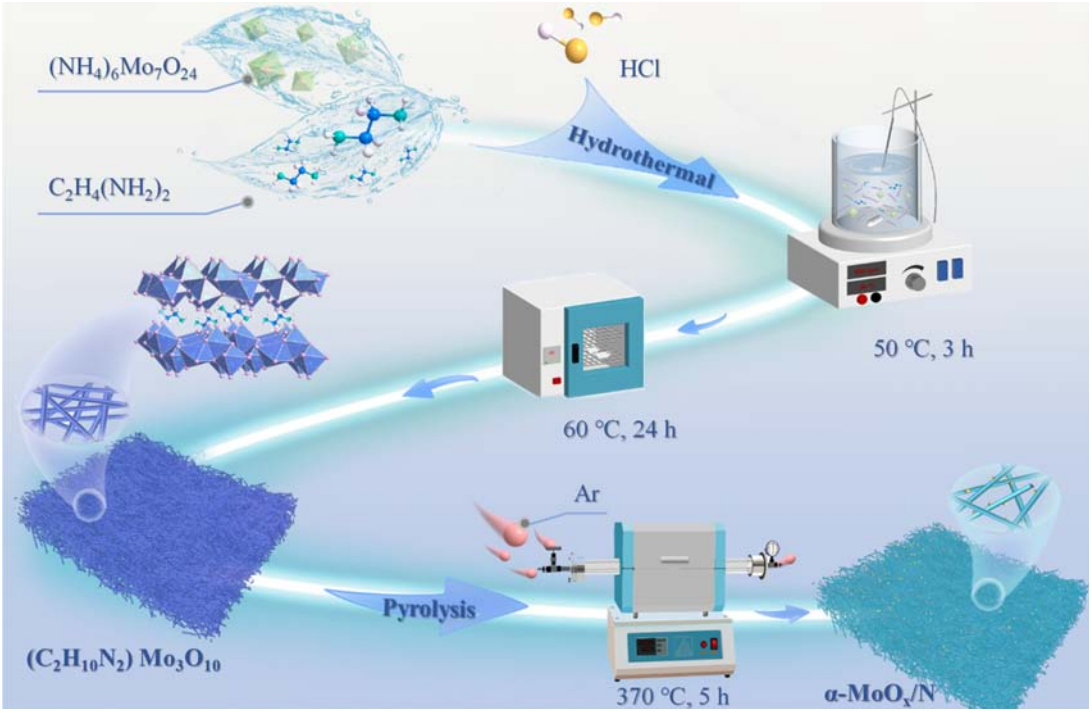


Fig. 3.1 The schematic illustration of the fabrication strategy for α-MoO_x/N.

The XRD patterns of the fabricated α-MoO_x and α-MoO_x/N were shown in Fig. 3.2a, the diffraction peaks corresponding to the orthorhombic phase MoO_3 (JCPDs No.

05-0508) with the crystallographic cell constants of a = 3.962 Å, b = 13.858 Å, c = 3.697 Å, and α = β = γ = 90° were observed in the XRD pattern of α-MoO_x without EDA. After introducing small amounts of EDA, all the peaks of α-MoO_x/N-1.05 and α-MoO_x/N-0.53 appeared with small peak intensities and wide peak widths, showing amorphous features. It implied that EDA attached to the surface of precursor particles through complexation and hindered the formation of interconnected polycrystalline structures. Note that the amorphous α-MoO_x has more unsaturated atoms or defective atoms, facilitating the trapping of more metal ions compared to the regularly arranged crystal structure [22]. Additionally, the slight shift angle could be observed at the 23.3° peak corresponding to (110) crystal plane of α-MoO_x with the increase of EDA, and this phenomenon has been reported to be attributed to the doping of nitrogen atoms with larger radius than that of oxygen atoms as well as to the interactions formed by the construction of heterojunction interface between α-MoO_x and EDA [29]. As EDA in the precursor solution increased, the smooth along with symmetrical diffraction peaks in the XRD pattern of α-MoO_x/N-0.35 confirmed the transition to crystalline features. The diffraction peak (040) may be the preferred orientation growth surface for α-MoO_x/N-0.35. Factors determining α-MoO_x nanostructure, crystalline phase transition and morphology were found to be intimately related to the various decomposition steps of the molybdenum ion-complexes in the precursor solution as well as to control of the post-annealing temperature [30–32].

For FT-IR measurement as seen in Fig. 3.2b, the peaks at 3450 cm^{-1} and 1623 cm^{-1} were ascribed to the O-H stretching vibrations and H-O-H in-plane bending vibration of water molecules [29,33]. The Mo=O stretching vibration, Mo-O-Mo bridging oxygen stretching vibration and Mo-O-Mo stretching vibration on α-MoO_x induced stretching vibrations of 995 cm^{-1}, 865 cm^{-1} and 603 cm^{-1}, respectively. Typical stretching vibrations of C-H and C≡N bonds observed at 2921 cm^{-1} and 2852 cm^{-1} for α-MoO_x/N indicated strong doping of nitrogen [34]. Furthermore, the characteristic peaks of α-MoO_x/N downshifted from 995 cm^{-1} to 964 cm^{-1} for Mo=O stretching vibration and upshifted from 863 cm^{-1} to 883 cm^{-1} for Mo-O-Mo bridging oxygen stretching vibration, potentially attributed to the complexation of amino groups (NH_2 or NH_3^+) in EDA with molybdenum or oxygen in $(C_2H_{10}N_2)Mo_3O_{10}$ [29,33].

XPS analysis was performed to determine the chemical state and surface composition of α-MoO_x/N-0.53, and the presence of Mo 3d, O 1s, N 1s, C 1s in the hybrid nanomaterials was supported by Fig. 3.2c. High-resolution Mo 3d XPS

spectroscopy results (Fig. 3.2d) demonstrated that both deconvoluted peaks centered at 235.88 eV and 232.78 eV correspond to $3d_{3/2}$ and $3d_{5/2}$ of Mo(VI), and the other two peaks at 234.68 eV and 231.58 eV were assigned to $3d_{3/2}$ and $3d_{5/2}$ of Mo(V) [22,35]. As shown in the N 1s state spectra of α-MoO_x/N-0.53 (Fig. 3.2e), four non-symmetrical peaks at 396.27 eV, 397.58 eV, 398.82 eV, and 400.8 eV were ascribed to Mo 3p, Mo-N, pyridinic N, and pyrrolic N, respectively, reflecting the successful doping of nitrogen and the formation of the interfacial Mo-N bonds [29,34,36,37]. Apart from the deconvolution of O 1s into peaks corresponding to C-O and Mo-O at 532.73 eV and 530.49 eV, the presence of oxygen vacancies was observed (531.29 eV), which was also clearly confirmed by the characteristic EPR signal near g = 2.003 (Figs. 3.2f and g) [28,38].

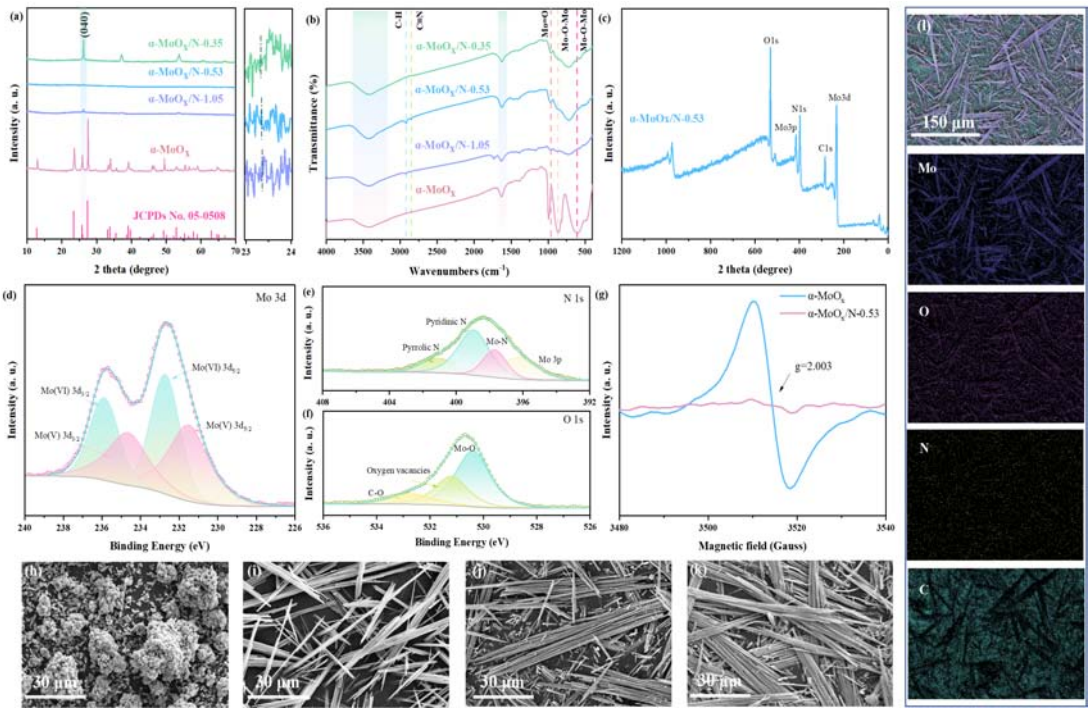


Fig. 3.2 (a) XRD patterns of α-MoO_x/N synthesised by hydrothermal synthesis and low-temperature pyrolysis with different amount of EDA; (b) FT-IR spectra of α-MoO_x/N; XPS spectra of α-MoO_x/N-0.53: (c) survey spectra and high-resolution spectra of (d) Mo 3d, (e) N 1s, (f) O 1s; (g) EPR spectra of α-MoO_x and α-MoO_x/N-0.53; SEM images of (h) α-MoO_x, (i) α-MoO_x/N-1.05, (j) α-MoO_x/N-0.53, (k) α-MoO_x/N-0.35 and (l) EDS element mapping images of α-MoO_x/N-0.53 for Mo, O, N, C.

The microstructures, morphology, and compositional analyses of α-MoO_x and α-MoO_x/N were shown in Figs. 3.2h-k. Typical nanorods were observed in the SEM of α-MoO_x undoped with EDA, being consistent with previous reports [30]. The addition of EDA achieved the transformation of α-MoO_x to one-dimensional nanowires, which has traditionally been considered as anisotropic growth due to the preferential adsorption of the crystal structure anisotropic agent EDA to certain planes of the hybrid crystals, yet lacking plausible explanations for the preferential adsorption of EDA [39]. Diverging from the traditional mechanism, Gao et al. proposed that the anisotropic molybdate anion ($Mo_3O_{10}^{2-}$) led to one-dimensional growth behavior independent of amine molecules (EDA, aniline, pyrrole) [27]. In-solution H^+ was crucial for triggering the different molybdate anion species. $Mo_3O_{10}^{2-}$ was susceptible to condensation at low pH levels (<4) to form the anisotropic clusters $Mo_8O_{26}^{4-}$ and $Mo_6O_{19}^{2-}$, accompanying the inhibition of one-dimensional growth. The XRD analysis of precursors synthesized with different Mo/EDA ratios (Fig. 3.2a) showed the predominant presence of $(C_2H_{10}N_2)Mo_3O_{10}$ at pH of 5. Moreover, the formation of Mo-O-Mo bonds in the $Mo_3O_{10}^{2-}$ chain is more likely than the molybdate anion to interact with $(C_2H_{10}N_2)^{2+}$ to form Mo-O⋯H-N, similar to the formation of Ge-O⋯H-N and W-O⋯H-N by ethylenediamine intercalation of GeO_x and WO_x [40,41]. The $(C_2H_{10}N_2)^{2+}$ in the one-dimensional ordered structure $(C_2H_{10}N_2)Mo_3O_{10}$ underwent carbonization during heating to form nitrogen-doped carbon, partial conversion of oxygen to H_2O, CO_2 and NO_2 were removed with argon gas flow. And the one-dimensional nanowires were retained during low-temperature pyrolysis. With the decrease of Mo/EDA, the nanowires were susceptible to agglomeration and rough surfaces accompanied by fine particles. One possible reason is that excessive EDA destabilized the precursor generated by the complexation of EDA with $(NH_4)_6Mo_7O_{24}•4H_2O$, thus leading to the occurrence of precipitation during heating [33]. Energy dispersive spectroscopy (EDS) analysis of α-MoO_x/N-0.53 indicated that molybdenum and oxygen were evenly distributed on the surface (Fig. 3.2l). α-MoO_x/N exhibited specific surface areas lower than 10.6 $m^2\ g^{-1}$, and pore sizes were predominantly less than 48.4 nm (Fig. 3.3 and Table 3.1), presenting low porosity structures. Compared to α-MoO_x, α-MoO_x/N with higher specific surface area and pore size might facilitate the infiltration of solute and provide more available active sites for gallium ions.

Table 3.1 Porous structural parameters for α-MoO_x and α-MoO_x/N

Sample	BET surface area (m^2/g)	Pore volume (cm^3/g)	Average pore width (nm)	BJH average pore width (nm)
α-MoO_x	4.95	0.04	30.71	25.84
α-MoO_x/N-1.05	7.08	0.06	31.17	27.69
α-MoO_x/N-0.53	7.99	0.08	48.44	46.08
α-MoO_x/N-0.35	10.59	0.11	42.51	39.32

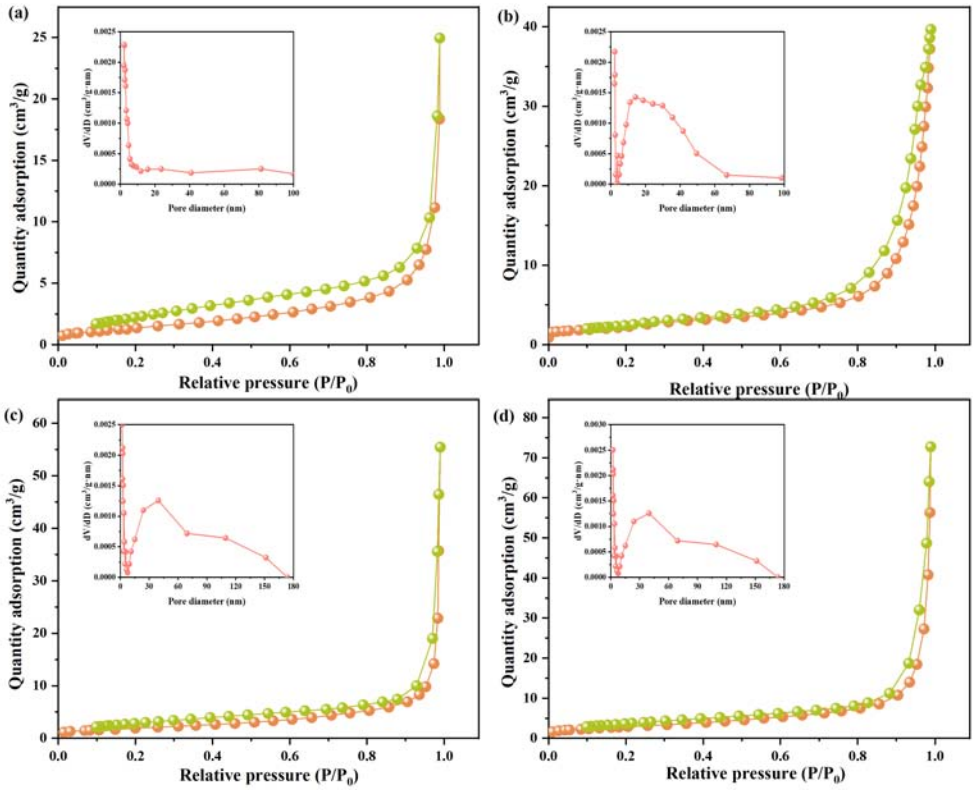


Fig. 3.3 N_2 adsorption-desorption isotherm (inset is the pore size distribution) of (a) α-MoO_x, (b) α-MoO_x/N-1.05, (c) α-MoO_x/N-0.53 and (d) α-MoO_x/N-0.35.

3.3.2. Anti-interference performance

Effect of pH on gallium ions adsorption: The effect of pH on the adsorption capacity of gallium ions was evaluated in the pH range of 2-4 (Fig. 3.4a). The adsorption performance of α-MoO_x and α-MoO_x/N for gallium ions increased significantly with increasing pH from 3.0 to 3.8. The adsorption of α-MoO_x/N for gallium ions at pH of 3.8 all exceeded 97.1%, superior to the adsorption of α-MoO_x (90.4%), reflecting that nitrogen-doping enhanced the adsorption of gallium ions [25].

The interpretation was supported by the enhancement of hydrophilicity (reduced contact angle) after nitrogen-doping (Fig. 3.5). The adsorption rate of α-MoO_x/N increased with the increase of nitrogen-doping amount, with the shortening of the contact time to reach the adsorption equilibrium (Fig. 3.6). α-MoO_x/N-1.05 and α-MoO_x/N-0.53 reached the adsorption equilibrium at 45 min and 60 min, corresponding to the adsorption capacity of 163.0 mg $g^{-1}$and 162.6 mg g^{-1}, respectively. Comparing the cost of agents and time, the adsorbent α-MoO_x/N-0.53 and pH of 3.8 could be selected as the optimal adsorbent and acidity for the adsorption of gallium ions.

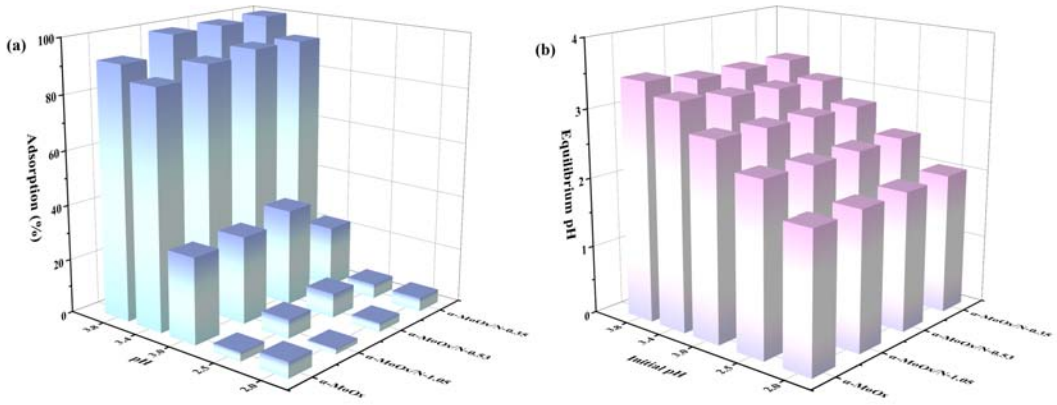


Fig. 3.4 (a) Adsorption performance of α-MoO_x and α-MoO_x/N for gallium ions at varying pH; (b) variation of pH during adsorption (solid-liquid ratio = 0.3 : 1 g L^{-1}, 50 mg L^{-1} gallium ions, time = 240 min).

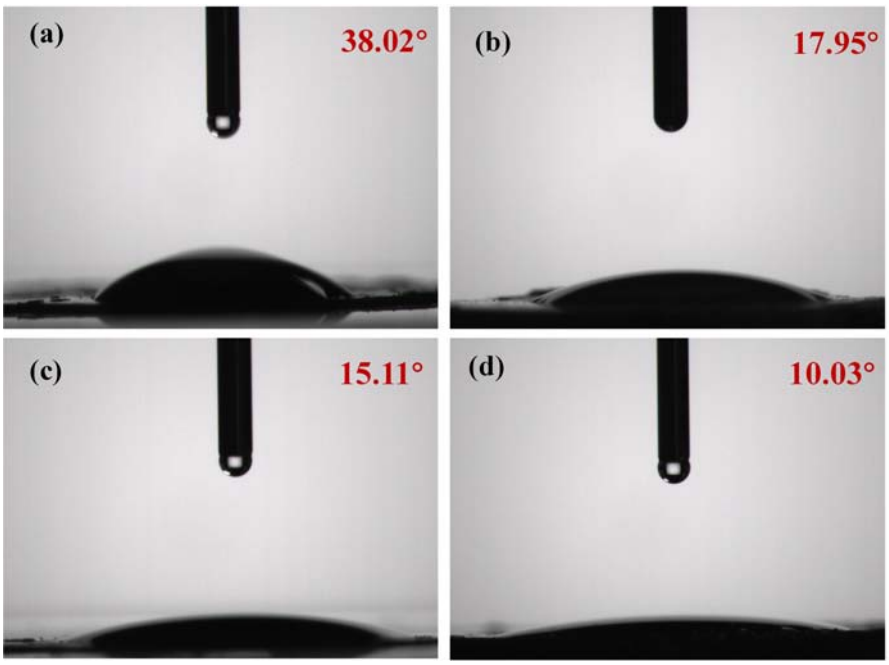


Fig. 3.5 Water contact angle of (a) α-MoO_x, (b) α-MoO_x/N-1.05, (c) α-MoO_x/N-0.53 and (d) α-MoO_x/N-0.35.

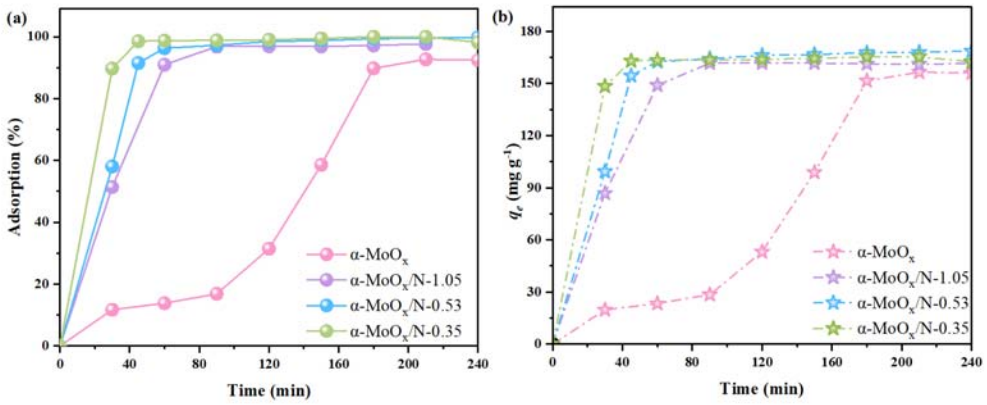


Fig. 3.6 (a) Adsorption efficiency and (b) adsorption capacity of different adsorbents for gallium ions (pH = 3.8, 0.3 : 1 g L^{-1}, 50 mg L^{-1} gallium ions, time = 240 min).

As shown in Fig. 3.4b, the adsorption process was accompanied by the decrease of pH. One possible explanation is that adsorbent surface groups (e.g., -OH, -COOH) behave as weak Bronsted acids to acidify the medium, which confirmed the occurrence of the proton exchange process [13,42]. The significant decrease in pH and increase in adsorption efficiency at the initial pH of 3-4 offered the possibility of α-MoO_x/N-0.53 capturing gallium ions by exchanging ions with H^+. While the loss of adsorbent surface charge weakened the driving force of the adsorption process (Fig. 3.7), and high concentration of H^+ in solution might compete with gallium ions for adsorption sites at low pH (<3.0), resulting in poor adsorption capacity [43,44].

Adsorption process of gallium ions was also controlled by the pH-determined metal species and surface properties of the adsorbent [42]. The species of gallium present at different pH values include Ga^{3+}, $Ga(OH)^{2+}$, $Ga(OH)_2^+$, $Ga(OH)_3$, $Ga(OH)_4^-$, and Ga $(OH)_5^{2-}$. Ga^{3+} is dominant at pH values below 3, and the protonated hydrolyzed species $Ga(OH)^{2+}$, $Ga(OH)_2^+$ progressively become predominant at controlled pH values between 3 and 4. When pH is in the range of 4-10, $Ga(OH)_3$ precipitates occur in solution and account for up to about 80.0% between 5 and 6 [14,45]. Gallium ions exist mainly as anionic hydrolysates (i.e., $Ga(OH)_4^-$, and Ga $(OH)_5^{2-}$) under alkaline conditions. The excellent adsorption performance of α-MoO_x/N-0.53 for gallium ions at pH lower than 4 was related to the surface electronegativity (Fig. 3.7). Similarly, the

effective adsorption of Cr^{6+} by α-MoO_x has been demonstrated to be due to the negatively charged surface [46]. Hydrolysis of α-MoO_x to form $HMoO_4^-$ and MoO_4^{2-} ($MoO_3 + H_2O \rightleftharpoons HMoO_4^- + H^+$, pK_{a1} = 3.61-4.00 and $HMoO_4^- \rightleftharpoons MoO_4^{2-} + H^+$, pK_{a2} = 3.89-4.37) would enhance the negative electronegativity of the α-MoO_x/N-0.53 surface [47].

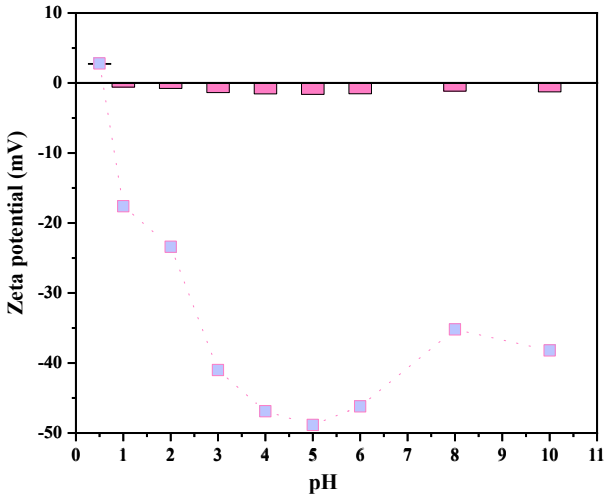


Fig. 3.7 Zeta potentials of α-MoO_x/N-0.53 obtained at different pH values.

Effect of coexisting ions on gallium ions adsorption: Control experiments without added adsorbent were conducted to assess the possibility of chemical precipitation during adsorption, and only 0-2.8% contribution of chemical precipitation was observed in all batch experiments. As shown in Fig. 3.8a, the weak selectivity of α-MoO_x/N-0.53 for Ga^{3+} was observed in the binary system containing Ga^{3+} and In^{3+} ($k_{Ga/In}$ = 6) and multivariate system. Based on the subtle variations in the physicochemical properties of gallium and indium, combining various separation techniques was the current feasible strategy to solve the problem of separating gallium and indium [48]. The combination of electrochemical techniques with dehydration and distillation for the separation of gallium and indium from spent photovoltaic cells benefited from the high solubility of $GaCl_3$ and low solubility of $InCl_3$ in $SOCl_2$ [49]. The high selectivity and capturing capacity of the extractants allowed the stepwise recovery of gallium and indium by impregnating solid adsorbents with the extractants while avoiding the environmental problems caused by the volatilization of organic solvents in solvent extraction [50,51]. In contrast, coupling targeted extractant-modified adsorbents with electrochemical methods may be the promising strategy for

one-step separation. The effective separation of Ga^{3+} from Fe^{3+} and Cr^{3+} was reflected by *k* values higher than 10 ($k_{Ga/Fe}$ = 14.5, $k_{Ga/Cr}$ = 18.5), superior to the carbonized and diethanolamine-functionalized rice husk [52]. Aiming at the separation and purification of Ga^{3+} and Fe^{3+}, numerous studies have been conducted to pre-remove Fe^{3+} from the leaching solution by employing extractants such as tri-n-butyl phosphate (TBP), Cyanex 921, Cyanex 923, P204, and N235 [53–55]. Ultrasound-assisted ferrous precipitation by addition of iron powder to reduce Fe^{3+} in solution to Fe^{2+} avoided gallium loss due to co-extraction/precipitation/occlusion as compared to solvent extraction, in which > 96% of Fe^{3+} was removed as $FeC_2O_4 \cdot 2H_2O$ with 1.4% gallium loss [56]. Considering the minor presence of Cr^{3+} in gallium-containing raw materials such as bauxite, Bayer's solution, zinc slag, and fly ash, there was no significant effect on gallium adsorption. High values of *k* ($k_{Ga/Zn}$ = 299, $k_{Ga/Al}$ = 91, $k_{Ga/Cu}$ = 58, and $k_{Ga/Ni}$ = 102) indicated that α-MoO_x/N-0.53 selectively adsorbed gallium ions in the binary systems containing Zn^{2+}, Al^{3+}, Cu^{2+}, Ni^{2+} ions. The adsorption of metal ions is related to the hydration radius, metal ions with smaller hydration radius and larger charge density are usually adsorbed better due to higher electrostatic force on the adsorbent surface, and the order of hydration radius of coexisting metal ions is Al^{3+} (0.50 Å) < Ga^{3+} (0.62 Å) < Fe^{3+} (0.64 Å) < Cr^{3+} (0.69 Å) < Cu^{2+} (0.72 Å) = Ni^{2+} (0.72 Å) < Zn^{2+} (0.74 Å) < In^{3+} (0.74 Å) [14]. Specifically, the preferential adsorption of Al^{3+}, In^{3+} and Ga^{3+} followed the order of stability of metal ions and ligand complexes. According to the ligand field theory, the full $4d^{10}$ orbital of In^{3+} can form more stable complexes with the same ligand than the $3d^{10}$ orbital of Ga^{3+}, thus hindering the selective adsorption of Ga^{3+} by the adsorbent [50]. And the ligand complexes formed by Al^{3+} belonging to s^2p^6 inert gas type outer electron are weaker in stability than Ga^{3+} belonging to the d^{10} outer electron [57]. Consequently, α-MoO_x/N-0.53 exhibited good selectivity, which was corroborated by 93.4% of Ga^{3+} being adsorbed in multivariate system containing Cu^{2+}, Zn^{2+}, Al^{3+}, Ni^{2+}, In^{3+}, Fe^{3+}, Cr^{3+} (Fig. 3.8b).

Given that gallium-containing wastewater usually has coexistence properties with high concentrations of Zn^{2+} and Al^{3+}, the effects on Ga^{3+} adsorption were investigated using different concentrations of Zn^{2+} and Al^{3+} (Fig. 3.8c). The adsorption of Ga^{3+} was hindered by the increase in Al^{3+} concentration, as reflected in the decrease in the adsorption efficiency of Ga^{3+} from 86.6% to 24.8% ($k_{Ga/Al}$ from 91 to 22). The probable reason for the inhibition of Ga^{3+} adsorption might be that high concentrations of Al^{3+} with smaller hydration radius adsorbed more readily on the surface of the adsorbent,

and the limited active sites were occupied by relatively high concentrations of Al^{3+}. It is well known that ion-imprinted materials (e.g., Ga-IIP-PP and Ga-AA-CS) [14,44], polymeric resins [10] and peptide-encapsulated sodium alginate hydrogel (H_6GaBP@SA) [58] showed excellent selectivity. However, the $k_{Ga/Al}$ values (mean value of 91) under the condition of 1:1 Ga/Al concentration ratio were 4.2-37.9 times higher than these reported materials, and slightly lower than gallotannin modified carbon nanotube (CNT-GT) adsorbents (mean value of 100) [57]. In contrast, high concentrations of Zn^{2+} (Ga/Zn concentration ratios as high as 1:10 and 1:100) presented weak inhibitory effects on Ga^{3+} adsorption. The $k_{Ga/Zn}$ value of α-MoO_x/N-0.53 at Ga/Zn concentration ratio of 1:10 was up to 1951, which was about 1.3-156.0 times higher than that of the reported adsorbents (Fig. 3.8d). The remarkable adsorption capacity and selectivity provide the possibility for selective recovery of trace gallium from industrial zinc refining wastewater and zinc slag leachate by α-MoO_x/N-0.53, which is of great significance in resource recycling and environmental protection.

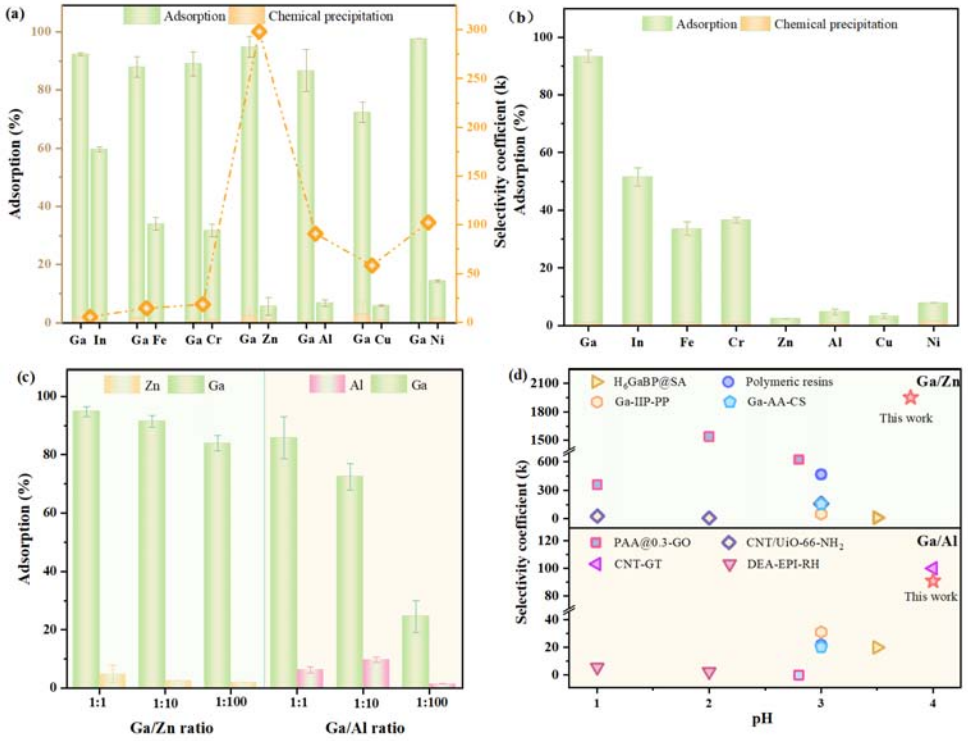


Fig. 3.8 (a) Adsorption efficiencies and selectivity coefficients (k) of α-MoO_x/N-0.53 for Ga^{3+} and coexisting ions In^{3+}, Fe^{3+}, Cr^{3+}, Zn^{2+}, Al^{3+}, Cu^{2+}, Ni^{2+} in binary systems; (b) Adsorption efficiencies of α-MoO_x/N-0.53 for Ga^{3+}, In^{3+}, Fe^{3+}, Cr^{3+}, Zn^{2+}, Al^{3+}, Cu^{2+}, Ni^{2+} in multivariate system; (c) Adsorption efficiencies of Ga^{3+}, Zn^{2+} and Al^{3+} in

binary systems of Ga/Zn and Ga/Al (concentration ratios of 1:1, 1:10 and 1:100); (d) Comparison of α-MoO_x/N-0.53 with other gallium adsorbents for $k_{Ga/Zn}$ and $k_{Ga/Al}$.

3.3.3. Gallium ions uptake capacity

Adsorption isotherm: The adsorption capacities of α-MoO_x/N-0.53 for gallium ions (Fig. 3.9) increased as the initial concentrations of gallium ions (ranging from 1 to 200 mg L^{-1}) increased, attributed to the increasing concentration gradient between the high levels of gallium ions in the native solution and the interface of α-MoO_x/N-0.53 providing driving force for diffusion of gallium ions into the adsorbent. And temperature was the critical factor to increase the adsorption efficiency and capacity (Fig. 3.9a and Fig. 3.10). Analyzing the distribution of gallium ions in the liquid and solid phases at different temperature (298-318 K) when adsorption reaches equilibrium using the Langmuir and Freundlich isotherm models, the experimental results fitted better with the Langmuir isotherm model reflecting single-molecule adsorption (Table 3.2), suggesting that chemisorption involved in the adsorption of gallium ions (Fig. 3.9). Intriguingly, the calculated maximum adsorption capacity (q_{max}) at 298 K was up to 464.8 mg g^{-1}, which was 2.4-136.7 times larger than that of previously reported gallium adsorbents (carbon-based materials, silicon-based materials, celluloses, ion-imprinted materials, polymer resins, etc., Table 3.3).

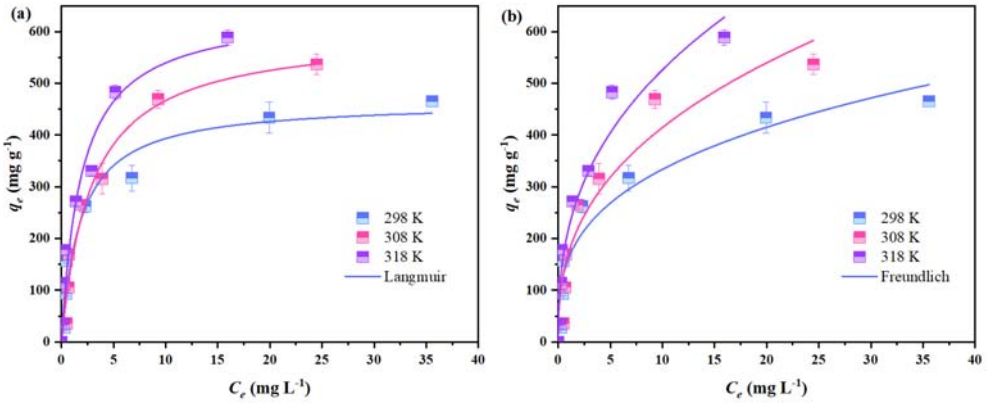


Fig. 3.9 Langmuir (a) and Freundlich (b) isotherm models for adsorption of gallium ions on α-MoO_x/N-0.53.

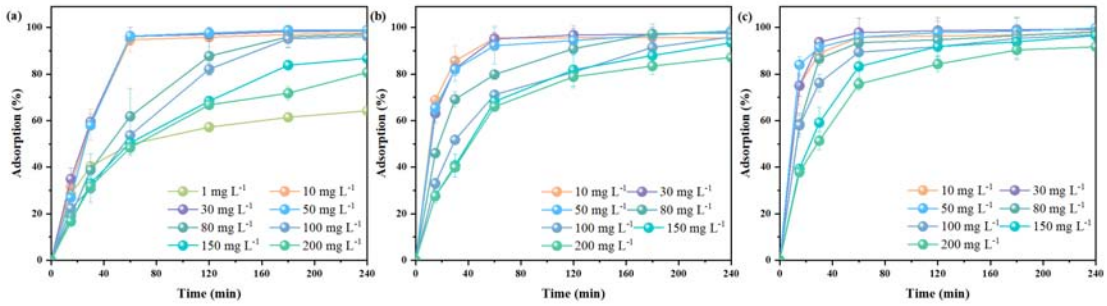


Fig. 3.10 Adsorption performances of α-MoO_x/N-0.53 for different initial concentrations of gallium ions at (a) 298 K, (b) 308 K, and (c) 318 K.

Table 3.2 Adsorption isotherm parameters on α-MoO_x/N-0.53

T	Langmuir			Freundlich		
	q_{max}	b	R^2	K_f	n	R^2
298 K	464.8	0.55	0.97	161.7	3.18	0.94
308 K	599.8	0.35	0.97	172.6	2.63	0.92
318 K	642.7	0.52	0.96	219.7	2.64	0.94

Table 3.3 Comparison of the gallium ions adsorption performance by α-MoO_x/N-0.53 and other adsorbents

Adsorbent	Concentration	pH	Equilibration time	q_{max} (mg g^{-1})	Ref.
Amide-functionalized cellulose	5 - 60 mg L^{-1}	3.4	30 min	3.4	[19]
Disordered mesoporous carbon	25 - 150 mg L^{-1}	3.0	15 min	4.4	[13]
Polymeric resins with catechol derivatives	5 - 60 mg L^{-1}	4.0	24 h	28.7	[10]
Amidoxime nanofiber membranes	200 mg L^{-1}	12.0	180 min	39.8	[16]
3D-α-FeOOH	5 - 40 mg L^{-1}	7.5	20 min	52.1	[73]
PAO/SiO_2	20 - 40 mg L^{-1}	4.0	60 min	63.3	[42]
P507-TBP/SiO_2-P	9 - 80 mmol	3.3	60 min	64.2	[74]
P507-mesoporous activated carbon	3 - 205 mg L^{-1}	2.0	90 min	67.0	[50]
Biogenic elemental tellurium nanoparticles	10 - 50 mg L^{-1}	4.0	60 min	74.1	[59]

Peptide-encapsulated sodium alginate hydrogel	10 - 200 mg L^{-1}	3.5	11 h	127.4	[58]
Persimmon peel-based ion-imprinted adsorbent	8 - 80 mg L^{-1}	3.0	240 min	128.0	[14]
Diethanolamine functionalized cellulose based on rice husk	20 mg L^{-1}	3	4 h	130.4	[18]
Gallotannin modified carbon nanotube composites (CNT-GT)	50 mg L^{-1}	3.0	4 h	170.8	[57]
Ga (III) imprinted bio-adsorbent based on acrylic-functionalized chitosan (Ga(III)-AA-CS)	25 - 400 mg L^{-1}	3.0	24 h	192.4	[44]
Polyacrylic acid functionalized GO (PAA/GO) composites	5 - 400 mg L^{-1}	2.8	-	196.8	[20]
α-MoO_x/N-0.53	1 - 200 mg L^{-1}	3.8	60 min	464.8	This work

Adsorption kinetics: For selected experimental conditions (pH = 3.8, 30 mg of α-MoO_x/N-0.53, 50 mg L^{-1} gallium ions), the adsorption capacity of α-MoO_x/N-0.53 for gallium ions within 60 min increased with contact time, and the adsorption rate exceeded that of poly (acrylonitrile)/silica composites and biogenic elemental tellurium nanoparticles reaching equilibrium at the same time (Table 3.3) [42,59]. As shown in Figs. 3.11a and b, the pseudo-second-order kinetic model ($R^2 = 0.98$) fitted the dynamic adsorption of gallium ions by α-MoO_x/N-0.53 significantly well than the pseudo-first-order model ($R^2 = 0.91$) and the adsorption capacity calculated by pseudo-second-order kinetic approximated to the calculated by adsorption experiments, suggesting that chemisorption may be involved in the adsorption of gallium ions. Based on the relationship between the pseudo-second-order kinetic rate constants (k_2) and temperatures (298-318 K), the reaction activation energy (E_a) calculated using the Arrhenius equation was approximately 54.599 kJ mol^{-1} (Fig. 3.12), which further confirmed the involvement of chemisorption [60]. The relatively low E_a implied that the activated molecules in the system were more prone to overcome the energetic barriers to effective collision [61].

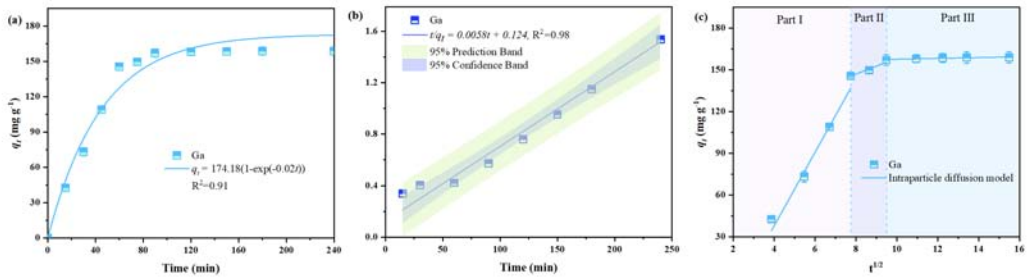


Fig. 3.11 (a) Pseudo-first-order kinetic model, (b) pseudo-second-order kinetic model, and (c) intraparticle diffusion model for adsorption of gallium ions on α-MoO_x/N-0.53.

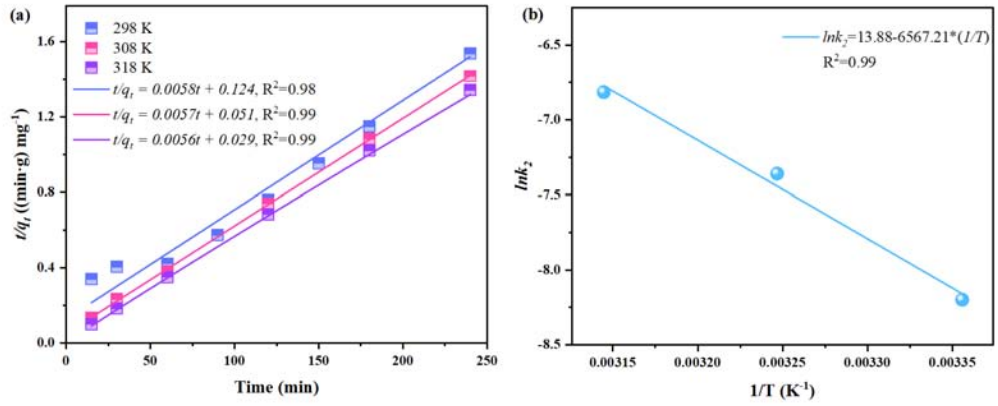


Fig. 3.12 (a) Fitting curves of pseudo-second-order kinetic model for the adsorption of gallium ions by α-MoO_x/N-0.53 at different temperatures and (b) fitting curve between lnk_2 and $1/T$.

Table 3.4 Adsorption thermodynamics parameters on α-MoO_x/N-0.53

T	298 K	308 K	318 K
ΔG^0 (kJ mol^{-1})	-370.618	-383.933	-397.248
ΔH^0 (kJ mol^{-1})		26.164	
ΔS^0 (kJ mol^{-1} K^{-1})		1.331	

The adsorption process of gallium ions diffusing the surface and attachment to the active sites of α-MoO_x/N-0.53 was determined by the amount of gallium ions, the external diffusion resistance, etc [43]. Fitting the experimental data to intraparticle diffusion model, external diffusion (part I), intraparticle diffusion (pore diffusion, part

II), and equilibrium stage (part III) of gallium ions were observed, accompanied by linear curve-fitting slopes $k_{part\ I}$ = 26.4 > $k_{part\ II}$ = 5.7 > $k_{part\ III}$ = 0.3 and non-zero intercepts (Fig. 3.11c), suggesting that external diffusion might dominate the adsorption process of gallium ions.

Adsorption thermodynamics: The calculated thermodynamic parameters of adsorption were listed in Table 3.4. The adsorption of gallium ions by α-MoO_x/N-0.53 was endothermic and spontaneous process, which was excited by increasing the temperature (298-318 K), as evidenced by free energy $\Delta G^0 < 0$ (calculated by Eq. 3.9) and enthalpy change $\Delta H^0 > 0$ (calculated by Eq. 3.10). The calculated reaction entropy of 1.331 kJ mol^{-1} K^{-1} indicated the increased disorder of the system and also the existence of more degrees of freedom for gallium ions on the α-MoO_x/N-0.53 surface [62].

3.3.4. Adsorption mechanism

No significant variations in the XRD patterns (Fig. 3.13) revealed that α-MoO_x/N-0.53 was stable during the adsorption process. FTIR and XPS of the samples before and after adsorption of gallium ions were analyzed to elucidate the adsorption mechanism. As shown in Fig 3.14a, absorption peak at 3425 cm^{-1} attributed to -OH stretching vibration in the FTIR pattern showed broad peak intensity reduction and shifted to lower wavenumber region (3397 cm^{-1}) after the adsorption of gallium ions, suggesting the involvement of -OH in the adsorption reaction of gallium ions. Combined with the Ga-O and Ga-OH stretching vibration peaks generated at 486 cm^{-1} and 1066 cm^{-1} [63,64], the gallium ions adsorption mechanism of α-MoO_x/N-0.53 involved the ion exchange of gallium ions with H^+ in the -OH group. The enhanced adsorption performance by nitrogen-doping was further confirmed as the corresponding C≡N stretching vibration peak decreased significantly and the weak peak observed at 570 cm^{-1} was reported to be attributed to the Ga-N stretching vibration [63].

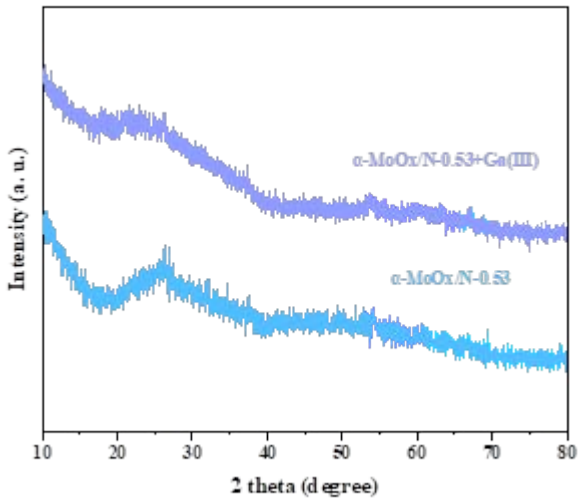


Fig. 3.13 XRD patterns of α-MoO_x/N-0.53 before and after adsorption of gallium ions.

The gallium ions in the liquid phase were successfully adsorbed on the surface of α-MoO_x/N-0.53, as evidenced by XPS spectra of the gallium-loading sample, which revealed Ga $2p_{1/2}$, Ga $2p_{3/2}$, and Ga 3d peaks at 1145 eV, 1119 eV, and 21 eV, respectively (Fig. 3.14b). High-resolution XPS spectra of Ga 2p and Ga 3d presented typical peaks with binding energy gaps of about 26.9 eV and 0.46 eV, respectively (Figs. 3.14c and d), and Ga $2p_{3/2}$ peaks were further deconvoluted into double peaks assigned to Ga-O and Ga-N [65], demonstrating that there was no discernible shift in the valence state of gallium ions. Additionally, high-resolution Mo 3d XPS spectra were analyzed after adsorption of gallium ions (Fig. 3.14e). The deconvolution peaks centered at 234.08 eV and 230.98 eV were assigned to $3d_{3/2}$ and $3d_{5/2}$ of Mo(V). Interestingly, the peak positions of both $3d_{3/2}$ and $3d_{5/2}$ of Mo(V) were shifted by 0.6 eV to lower binding energies and accompanied by a decrease in relative content from 49.4% to 40.9%. Whereas the relative content of Mo(VI), without any shift in peak position, increased from 50.6% to 59.1%, as the result of the oxidation reaction of Mo(V) to Mo(VI). On the other hand, the shifts of the peaks could be due to the interfacial electron transfer between gallium ions and Mo(V) species, which might induce partial structural evolution of the external Mo-O and lead to larger binding energy [22,66]. Hence, the capture of gallium ions by α-MoO_x/N-0.53 probably involved self-reinforced adsorption mechanism. It has been reported that metal ions act as acceptors of electrons adsorbed on the lattice oxygen of α-MoO_x, leading to the decrease of the crystal lattice oxygen content [66]. Analysis of high-resolution O 1s XPS spectra before and after

adsorption (Fig. 3.14f) revealed the decrease in the relative content of Mo-O from 56.4% to 44.4% and the appearance of Ga-O, which was presumably involved the formation of Mo-O-Ga by complexation between partial gallium ions and Mo-O. Similar adsorption mechanisms were present in the adsorption of Ag^+ by MoO_x (forming Mo-O-Ag) [22]. Moreover, the decrease in the relative content of oxygen vacancies (from 29.6% to 24.9%) coupled with decreasing signals in the EPR of oxygen vacancies (Fig. 3.15) demonstrated that oxygen vacancies in α-MoO_x/N-0.53 could act as adsorption traps for gallium ions. Oxygen vacancies are usually positively charged due to the negative charge taken away by oxygen atoms, and gallium ions arriving at the surface and near-surface regions of α-MoO_x/N-0.53 by electrostatic and chemical adsorption might diffuse and fill the oxygen vacancies and charge-compensate with the positive charge of the oxygen vacancies to reach charge equilibrium [21,67].

Higher content of Pyridinic N can also act as active sites, thus improving the adsorption performance of the adsorbent [37]. As shown in Figs. 3.2e and 3.14g, the decrease in the relative content of Pyridinic N from 28.4% to 25.3% (shift of peak position from 398.82 eV to 398.59 eV) after adsorption indicated that Pyridinic N was involved in the adsorption process of gallium ions by complexation. In summary, ion exchange and surface complexation were the major mechanisms for the adsorption of gallium ions by α-MoO_x/N-0.53, and the presence of oxygen vacancies stimulated the adsorption of a small fraction of gallium ions.

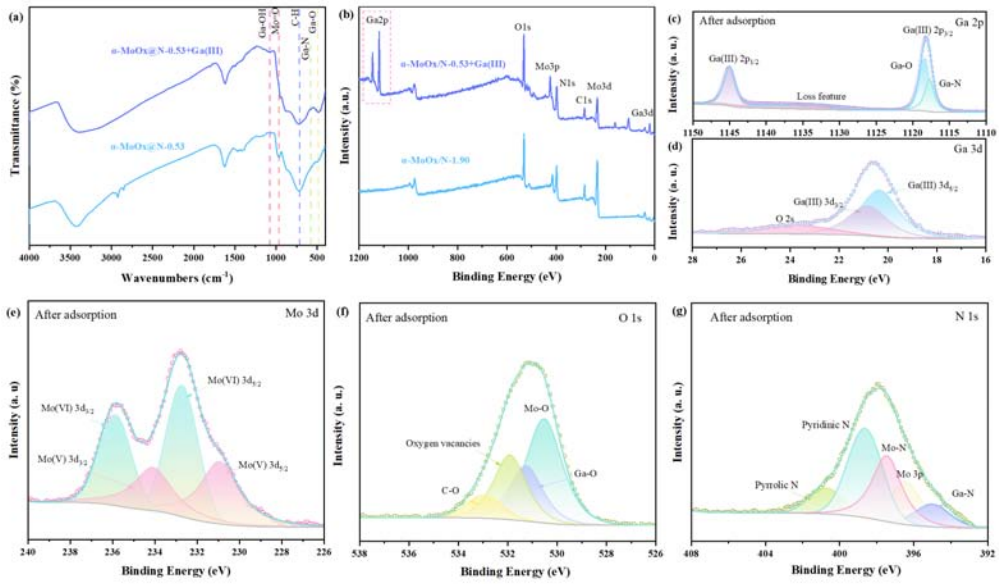


Fig. 3.14 (a) FTIR patterns and (b) XPS spectra of α-MoO_x/N-0.53 before and after adsorption of gallium ions; High-resolution XPS spectra of (c) Ga 2p, (d) Ga 3d, (e)

Mo 3d, (f) O 1s and (g) N 1s after adsorption.

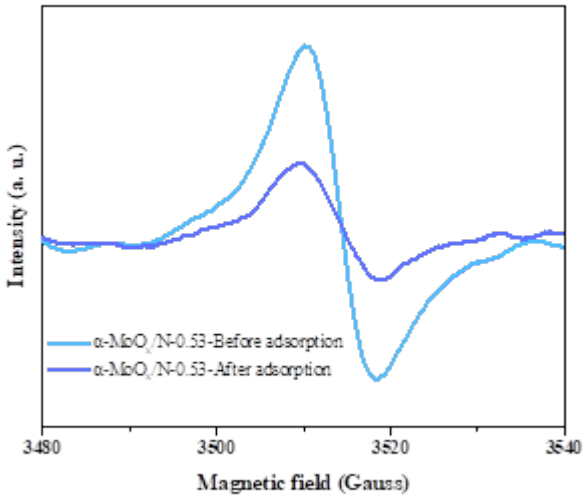


Fig. 3.15 EPR spectra of α-MoO_x/N-0.53 before and after adsorption for gallium ions.

3.3.5. Adsorption and desorption Cycles

Outstanding elution and regeneration performance are essential for the material to yield greater economic benefits. 0.1 M HNO_3 could effectively desorb gallium ions from α-MoO_x/N-0.53 adsorbent, and the desorption efficiency exceeded 90.8% after 1 h of desorption (Fig. 3.16a). In spite of the decrease in the adsorption efficiency of gallium ions after taking five adsorption-desorption cycles, 94.5% of gallium ions were still adsorbed. The average molybdenum and nitrogen dissolution loss of α-MoO_x/N-0.53 were 0.5% and 0.09%, respectively, during the adsorption process (Fig. 3.16b), indicating that α-MoO_x/N-0.53 exhibited excellent recycling stability. Nevertheless, 2.1%-3.2% of molybdenum and 0.1% of nitrogen in α-MoO_x/N-0.53 were observed to be dissolved during desorption under acidic conditions (0.1 M HNO_3). The morphology of α-MoO_x/N-0.53 after adsorption-desorption was characterized by SEM-EDS (Fig. 3.17), revealing the nanowires occurred to be agglomerated and the nanowire structure on the surface of the agglomerates was destroyed owing to the chemical solubilization in the acidic conditions. Notably, the insertion/extraction of ions during cycling introduces a large volume change, thus generating additional stress [68], which corresponds to the decrease in molybdenum solubility with increasing cycling. The surface reconstruction, leaching and degradation of the active species have been reported to cause instability of transition metal oxides (e.g., MoO_3, WO_3, Co_3O_4, and NiO) in acidic conditions [68,69].

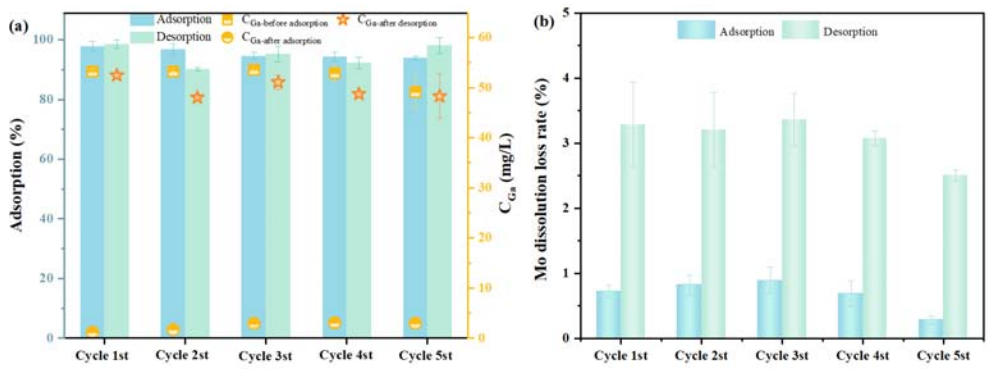


Fig. 3.16 (a) Cyclic adsorption performance of gallium ions on α-MoO_x/N-0.53 and desorption efficiency of gallium ions on α-MoO_x/N-0.53 by 0.1 M HNO_3; (b) molybdenum dissolution loss rates during the adsorption and desorption process.

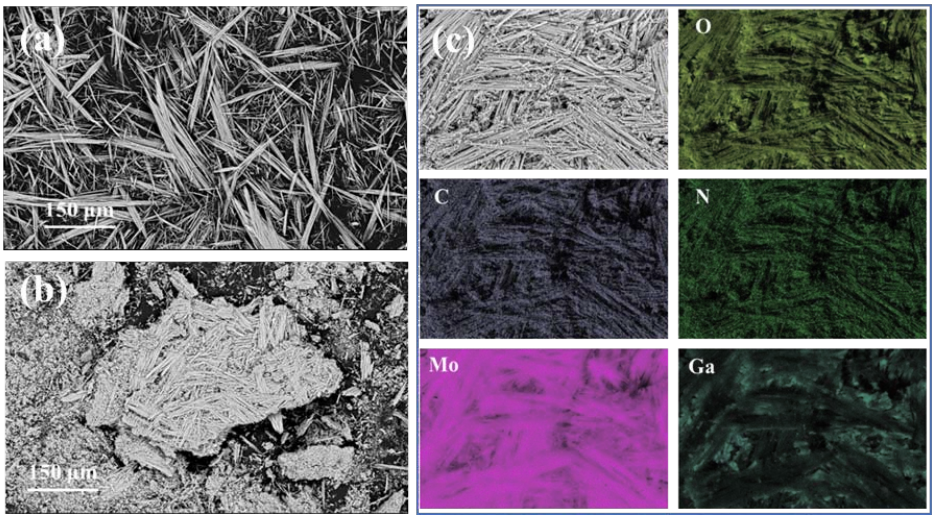


Fig. 3.17 SEM images of α-MoOx/N-0.53 (a) before and (b) after adsorption of gallium ions; (c) EDS element mapping images of α-MoO_x/N-0.53 for O, C, N, Mo, Ga after adsorption.

Although α-MoO_x/N-0.53 exhibited excellent adsorption and desorption performance for gallium ions, further improvement of the stability of the adsorbent is crucial for the long-term adsorption capacity in practical applications. It was reported that annealing of MoO_x in the inert environment at 450-500 °C improved the doping strength and stability [70]. Comparatively, enhanced crystal stability and decreased probability of surface remodeling and leaching of MoO_x could be more easily achieved by metal-doping (e.g., Ni, Ti) [71,72]. Given the characteristic groups (-OH and -COOH) and ligand atoms (O and N) that bind to gallium ions, synthesis of MoO_x/N

/carbon-based materials (carbon nanotube or graphene) nanocomposites and surface modification of MoO_x/N using gallium adsorbent SiO_2 are alternatives to enhance chemical resistance and prospectively promote gallium adsorption of the materials [34,70].

3.3.6. Gallium ions adsorption from zinc slag leachate

Simulated zinc slag leachate (composition shown in Table 3.5) according to the ratio of each component of zinc slag from one smelter in Guangdong Province was performed to further evaluate the potential of α-MoO_x/N-0.53 for gallium capture from gallium-containing wastewater. Under the provided conditions (pH = 3.8, solid-liquid ratio = 1 : 1 g L^{-1}), 92.3% of gallium ions were adsorbed by α-MoO_x/N-0.53 with the concentration decreasing to 3.8 mg L^{-1} after 240 min. No significant concentration changes were observed for the competing ions Zn^{2+} and Cu^{2+}, and the concentration of Al^{3+} decreased from 203.2 mg L^{-1} to 177.6 mg L^{-1} (adsorption efficiency of 12.6%), which was consistent with the above batch test results. The decrease in Fe^{3+} concentration from 1609.1 mg L^{-1} to 154.0 mg L^{-1} was mainly attributed to the observed precipitation reaction during adsorption at pH 3-4, thus pre-removal of iron is an essential step to optimize the adsorption of gallium ions.

Table 3.5 Major elements in simulated zinc slag leachate (mg L^{-1})

Ga	Zn	Fe	Cu	Al	As	Pb
49.3	2511.2	1609.1	1234.8	203.2	100.0	22.2

3.4. Conclusions

Overall, α-MoO_x/N were synthesized by the hybrid strategy of hydrothermal synthesis and low-temperature pyrolysis, with the content of EDA in the precursor being the key factor determining the α-MoO_x/N nanostructure, crystalline phase transition and morphology. Amorphous α-MoO_x/N-0.53 with abundant oxygen vacancies and active sites exhibited excellent adsorption performance (maximum adsorption capacity of 464.8 mg g^{-1} predicted by the Langmuir model) and selectivity ($k_{Ga/Zn}$ value up to 1951) under acidic conditions, providing feasibility for the recovery of gallium from zinc smelting wastewater, zinc slag leachate and other gallium-containing effluents. pH was the switch that triggered the negatively charged α-MoO_x/N-0.53 to achieve excellent adsorption performance, and the gallium ions

adsorption process was accompanied by the proton release process. Synergistic effects of electrostatic adsorption, ion exchange and surface complexation were crucial to stimulate gallium ions adsorption. Furthermore, the capture of gallium ions by α-MoO_x/N-0.53 remained at 94.5% for five consecutive adsorption cycles, highlighting the potential for gallium ions recovery, but further efforts are needed to improve the stability of α-MoO_x/N.

3.5. References

[1] Study on the Critical Raw Materials for the EU 2023, 2023.

[2] Z. Zhao, L. Cui, Y. Guo, H. Li, F. Cheng, Recovery of gallium from sulfuric acid leach liquor of coal fly ash by stepwise separation using P507 and Cyanex 272, Chem. Eng. J. 381 (2020) 122699. https://doi.org/10.1016/j.cej.2019.122699.

[3] K. Zheng, M.F. Benedetti, E.D. van Hullebusch, Recovery technologies for indium, gallium, and germanium from end-of-life products (electronic waste) – A review, J. Environ. Manage. 347 (2023) 119043. https://doi.org/10.1016/j.jenvman.2023.119043.

[4] K.N. Sheaffer, Mineral commodity summaries 2023, 2023. http://pubs.er.usgs.gov/publication/mcs2023.

[5] M. Frenzel, M.P. Ketris, T. Seifert, J. Gutzmer, On the current and future availability of gallium, Resour. Policy. 47 (2016) 38–50. https://doi.org/10.1016/j.resourpol.2015.11.005.

[6] F. Lu, T. Xiao, J. Lin, Z. Ning, Q. Long, L. Xiao, F. Huang, W. Wang, Q. Xiao, X. Lan, H. Chen, Resources and extraction of gallium: A review, Hydrometallurgy. 174 (2017) 105–115. https://doi.org/10.1016/j.hydromet.2017.10.010.

[7] R.P. de Oliveira, J. Benvenuti, D.C.R. Espinosa, A review of the current progress in recycling technologies for gallium and rare earth elements from light-emitting diodes, Renew. Sustain. Energy Rev. 145 (2021) 111090. https://doi.org/10.1016/j.rser.2021.111090.

[8] S. Saikia, R.B. Costa, A. Sinharoy, M.P. Cunha, M. Zaiat, P.N.L. Lens, Selective removal and recovery of gallium and germanium from synthetic zinc refinery residues using biosorption and bioprecipitation, J. Environ. Manage. 317 (2022) 115396. https://doi.org/10.1016/j.jenvman.2022.115396.

[9] A.S. Hoang, H.N. Nguyen, N. Quoc Bui, H.S. Vu, T.P. Vo, T.V. Nguyen, C. Minh Phan, Extraction of gallium from Bayer liquor using extractant produced from cashew nutshell liquid, Miner. Eng. 79 (2015) 88–93.

https://doi.org/10.1016/j.mineng.2015.05.012.

[10]P. Raj, M. Patel, A.K. Karamalidis, Chemically modified polymeric resins with catechol derivatives for adsorption, separation and recovery of gallium from acidic solutions, J. Environ. Chem. Eng. 11 (2023) 110790. https://doi.org/10.1016/j.jece.2023.110790.

[11]L. Liu, B. Dong, C. Cai, Effect and Mechanism of Cu Foams with Different Porosity on Kinetic Parameters of Ga Electrodeposition: Accompanied by Hydrogen Evolution Reaction, J. Electrochem. Soc. 170 (2023) 022507. https://doi.org/10.1149/1945-7111/acbba3.

[12]Z. Liu, Q. Tian, X. Guo, Y. Huang, Z. Xu, Pulse cyclone electrowinning of gallium recovery for higher current efficiency and lower energy consumption, Sep. Purif. Technol. 326 (2023) 124801. https://doi.org/10.1016/j.seppur.2023.124801.

[13]E. Díez, J.M. Gómez, A. Rodríguez, I. Bernabé, J. Galán, Recovery of Gallium from Aqueous Solution through Preconcentration by Adsorption/Desorption on Disordered Mesoporous Carbon, J. Sustain. Metall. 7 (2021) 227–242. https://doi.org/10.1007/s40831-021-00336-4.

[14]L. Gao, L. Wang, Y. Cao, S. Li, Persimmon peel-based ion-imprinted adsorbent with enhanced adsorption performance of gallium ions, Miner. Eng. 176 (2022) 107354. https://doi.org/10.1016/j.mineng.2021.107354.

[15]W. Li, C. Zhou, C. Li, W. Zhu, J. Shi, G. Liu, Synthesis of CNT/UiO-66-NH_2 adsorbent and the selective adsorption of gallium in solution, Sep. Purif. Technol. 323 (2023) 124464. https://doi.org/10.1016/j.seppur.2023.124464.

[16]Z. Qin, Y. Liao, Z. Wang, S. Wang, L. Song, K. Ma, D. Luo, H. Yue, Innovative Amidoxime Nanofiber Membranes for Highly Effective Adsorption of Ga(III) from Waste Bayer Solution, Ind. Eng. Chem. Res. 62 (2023) 11140–11150. https://doi.org/10.1021/acs.iecr.3c01410.

[17]Z. Zhang, H. Zhang, Y. Hu, X. Yang, S. Yao, Novel surface molecularly imprinted material modified multi-walled carbon nanotubes as solid-phase extraction sorbent for selective extraction gallium ion from fly ash, Talanta. 82 (2010) 304–311. https://doi.org/10.1016/j.talanta.2010.04.038.

[18]Y. Xiong, X. Cui, D. Wang, Y. Wang, Z. Lou, W. Shan, Y. Fan, Diethanolamine functionalized rice husk for highly efficient recovery of gallium(III) from solution and a mechanism study, Mater. Sci. Eng. C. 99 (2019) 1115–1122. https://doi.org/10.1016/j.msec.2019.02.028.

[19] W. Guo, J. Zhang, F. Yang, F. Tan, Z. Zhao, Highly efficient and selective recovery of gallium achieved on an amide-functionalized cellulose, Sep. Purif. Technol. 237 (2020) 116355. https://doi.org/10.1016/j.seppur.2019.116355.

[20] Y. Zhang, X. Liu, Y. Wang, Z. Lou, W. Shan, Y. Xiong, Polyacrylic acid-functionalized graphene oxide for high-performance adsorption of gallium from aqueous solution, J. Colloid Interface Sci. 556 (2019) 102–110. https://doi.org/10.1016/j.jcis.2019.08.032.

[21] G. Zhuang, Y. Chen, Z. Zhuang, Oxygen vacancies in metal oxides : recent progress towards advanced catalyst design, 63 (2020) 2089–2118.

[22] P. Shao, Z. Chang, M. Li, X. Lu, W. Jiang, K. Zhang, X. Luo, L. Yang, Mixed-valence molybdenum oxide as a recyclable sorbent for silver removal and recovery from wastewater, Nat. Commun. 14 (2023) 1362. https://doi.org/10.1038/s41467-023-37143-2.

[23] J.P.H. Perez, K. Folens, K. Leus, F. Vanhaecke, P. Van Der Voort, G. Du Laing, Progress in hydrometallurgical technologies to recover critical raw materials and precious metals from low-concentrated streams, Resour. Conserv. Recycl. 142 (2019) 177–188. https://doi.org/10.1016/j.resconrec.2018.11.029.

[24] K. Zhu, X. Wang, J. Liu, S. Li, H. Wang, L. Yang, S. Liu, T. Xie, Novel Amorphous MoS_2/MoO_3/Nitrogen-Doped Carbon Composite with Excellent Electrochemical Performance for Lithium Ion Batteries and Sodium Ion Batteries, ACS Sustain. Chem. Eng. 5 (2017) 8025–8034. https://doi.org/10.1021/acssuschemeng.7b01595.

[25] S. Chen, K. Huang, H.F. Wang, H. Wang, H. Yu, J. Huang, Y. Cao, Electric-field enhanced three-dimensional flexible carbon felt as a host for Pt^{4+} ions extraction, Chem. Eng. J. 490 (2024) 151835. https://doi.org/10.1016/j.cej.2024.151835.

[26] Y. Li, S.M. Shaheen, M. Azeem, L. Zhang, C. Feng, J. Peng, W. Qi, J. Liu, Y. Luo, Y. Peng, E.F. Ali, K. Smith, J. Rinklebe, Z. Zhang, R. Li, Removal of lead (Pb^{+2}) from contaminated water using a novel MoO_3-biochar composite: Performance and mechanism, Environ. Pollut. 308 (2022) 119693. https://doi.org/10.1016/j.envpol.2022.119693.

[27] Q. Gao, S. Wang, H. Fang, J. Weng, Y. Zhang, J. Mao, Y. Tang, One-dimensional growth of MoO_x-based organic-inorganic hybrid nanowires with tunable photochromic properties, J. Mater. Chem. 22 (2012) 4709–4715. https://doi.org/10.1039/c2jm15443a.

[28] J. Xu, C. Zhang, H. Liu, J. Sun, R. Xie, Y. Qiu, F. Lü, Y. Liu, L. Zhuo, X. Liu, J.

Luo, Amorphous MoO_x-Stabilized single platinum atoms with ultrahigh mass activity for acidic hydrogen evolution, Nano Energy. 70 (2020) 104529. https://doi.org/10.1016/j.nanoen.2020.104529.

[29] C. Hu, J. Yin, S. Xun, L. Zhu, H. Li, M. He, P. Wu, H. Li, W. Zhu, Constructing interface chemical coupling S-scheme heterojunction MoO_{3-x}@PPy for enhancing photocatalytic oxidative desulfurization performance: Adjusting LSPR effect via oxygen vacancy engineering, Appl. Catal. B Environ. 355 (2024) 124155. https://doi.org/10.1016/j.apcatb.2024.124155.

[30] S. Cong, T. Sugahara, T. Wei, J. Jiu, Y. Hirose, S. Nagao, K. Suganuma, Growth and Extension of One-Step Sol-Gel Derived Molybdenum Trioxide Nanorods via Controlling Citric Acid Decomposition Rate, Cryst. Growth Des. 15 (2015) 4536–4542. https://doi.org/10.1021/acs.cgd.5b00790.

[31] I.A. de Castro, R.S. Datta, J.Z. Ou, A. Castellanos-Gomez, S. Sriram, T. Daeneke, K. Kalantar-zadeh, Molybdenum Oxides – From Fundamentals to Functionality, Adv. Mater. 29 (2017) 1701619. https://doi.org/10.1002/adma.201701619.

[32] V.H.V. Quy, I.R. Jo, S.H. Kang, K.S. Ahn, Amorphous-crystalline dual phase WO_3 synthesized by pulsed-voltage electrodeposition and its application to electrochromic devices, J. Ind. Eng. Chem. 94 (2021) 264–271. https://doi.org/10.1016/j.jiec.2020.10.047.

[33] D. Zhou, L. Yang, Enhanced Electrochromic Properties of Nanocrystalline Molybdenum Oxide Films Modified by Dopamine, Coatings. 13 (2023) 1292. https://doi.org/10.3390/coatings13071292.

[34] L. Gurusamy, G.J. Lee, S. Anandan, N. Liu, J.J. Wu, Fabrication of molybdenum oxycarbide nanoparticles dispersed on nitrogen-doped carbon hollow nanotubes through anion exchange mechanism for enhanced performance in supercapacitor, J. Energy Storage. 27 (2020) 101122. https://doi.org/10.1016/j.est.2019.101122.

[35] P. Gao, Q. Ru, Z. Pan, J. Zhang, W. Xu, F. Chi-Chung Ling, L. Wei, Robust hetero-MoO_3/MoO_2@N-doped carbon nanobelts decorated with oxygen deficiencies as high-performance anodes for potassium/sodium storage, J. Colloid Interface Sci. 599 (2021) 730–740. https://doi.org/10.1016/j.jcis.2021.04.110.

[36] A. Xie, X. Lin, C. Zhang, S. Cheng, W. Dong, F. Wu, Oxygen vacancy mediated polymerization of pyrrole on MoO_3 to construct dielectric nanocomposites for electromagnetic waves absorption application, J. Alloys Compd. 938 (2023) 168523. https://doi.org/10.1016/j.jallcom.2022.168523.

[37] P. Zhang, S. Guo, J. Liu, C. Zhou, S. Li, Y. Yang, J. Wu, D. Yu, L. Chen, Highly uniform nitrogen-doped carbon decorated MoO_2 nanopopcorns as anode for high-performance lithium/sodium-ion storage, J. Colloid Interface Sci. 563 (2020) 318–327. https://doi.org/10.1016/j.jcis.2019.12.062.

[38] J.C. Liu, H. Li, M. Batmunkh, X. Xiao, Y. Sun, Q. Zhao, X. Liu, Z.H. Huang, T.Y. Ma, Structural engineering to maintain the superior capacitance of molybdenum oxides at ultrahigh mass loadings, J. Mater. Chem. A. 7 (2019) 23941–23948. https://doi.org/10.1039/c9ta04835a.

[39] H. Bin Yao, M.R. Gao, S.H. Yu, Small organic molecule templating synthesis of organic-inorganic hybrid materials: Their nanostructures and properties, Nanoscale. 2 (2010) 323–334. https://doi.org/10.1039/b9nr00192a.

[40] W. Li, F. Xia, J. Qu, P. Li, D. Chen, Z. Chen, Y. Yu, Y. Lu, R.A. Caruso, W. Song, Versatile inorganic-organic hybrid WO_x-ethylenediamine nanowires: Synthesis, mechanism and application in heavy metal ion adsorption and catalysis, Nano Res. 7 (2014) 903–916. https://doi.org/10.1007/s12274-014-0452-9.

[41] B.Q. Gao, P. Chen, Y. Zhang, Y. Tang, Synthesis and Characterization of Organic – Inorganic Hybrid GeO x / Ethylenediamine Nanowires, (2008) 1837–1842. https://doi.org/10.1002/adma.200701646.

[42] S. Lu, L. Chen, M.F. Hamza, C. He, X. Wang, Y. Wei, E. Guibal, Amidoxime functionalization of a poly(acrylonitrile)/silica composite for the sorption of Ga(III) – Application to the treatment of Bayer liquor, Chem. Eng. J. 368 (2019) 459–473. https://doi.org/10.1016/j.cej.2019.02.094.

[43] Y. Zhu, W. Wang, H. Zhang, X. Ye, Z. Wu, A. Wang, Fast and high-capacity adsorption of Rb+ and Cs+ onto recyclable magnetic porous spheres, Chem. Eng. J. 327 (2017) 982–991. https://doi.org/10.1016/j.cej.2017.06.169.

[44] Y. Wang, L. Zhu, Y. Song, Z. Lou, W. Shan, Y. Xiong, Novel chitosan-based ions imprinted bio-adsorbent for enhanced adsorption of gallium(III) in acidic solution, J. Mol. Liq. 320 (2020) 114413. https://doi.org/10.1016/j.molliq.2020.114413.

[45] Y. Zhang, L. Zhu, Y. Wang, Z. Lou, W. Shan, Y. Xiong, Y. Fan, Preparation of a biomass adsorbent for gallium(III) based on corn stalk modified by iminodiacetic acid, J. Taiwan Inst. Chem. Eng. 91 (2018) 291–298. https://doi.org/10.1016/j.jtice.2018.05.030.

[46] X. Zhang, Z. Song, H. Hao Ngo, W. Guo, Z. Zhang, Y. Liu, D. Zhang, Z. Long, Impacts of typical pharmaceuticals and personal care products on the performance and

microbial community of a sponge-based moving bed biofilm reactor, Bioresour. Technol. 295 (2020) 122298. https://doi.org/10.1016/j.biortech.2019.122298.

[47] E.Z. Kedves, E. Bárdos, T. Gyulavári, Z. Pap, K. Hernadi, L. Baia, Dependence of cationic dyes' adsorption upon α-MoO_3 structural properties, Appl. Surf. Sci. 573 (2022) 151584. https://doi.org/10.1016/j.apsusc.2021.151584.

[48] Z. Li, Z. Chen, W. Ma, C. Cai, S. Li, Y. Wang, Efficient separation and recovery of valuable gallium and indium from gallium-based liquid metal waste, J. Clean. Prod. 408 (2023) 137053. https://doi.org/10.1016/j.jclepro.2023.137053.

[49] S. Gu, B. Fu, G. Dodbiba, T. Fujita, B. Fang, Promising Approach for Recycling of Spent CIGS Targets by Combining Electrochemical Techniques with Dehydration and Distillation, ACS Sustain. Chem. Eng. 6 (2018) 6950–6956. https://doi.org/10.1021/acssuschemeng.8b00787.

[50] W. Wang, X. Xu, D. Lai, Q. Xu, J. Li, Y. Wang, Selective isolation of gallium and indium from waste photovoltaic modules facilitated by extractant-mesoporous activated carbon composites, Sep. Purif. Technol. 330 (2024) 125510. https://doi.org/10.1016/j.seppur.2023.125510.

[51] D. Hu, B. Ma, X. Li, Y. Lv, W. Zhang, Y. Chen, C. Wang, Efficient separation and recovery of gallium and indium in spent CIGS materials, Sep. Purif. Technol. 282 (2022) 120087. https://doi.org/10.1016/j.seppur.2021.120087.

[52] Y. Xiong, X. Cui, D. Wang, Y. Wang, Z. Lou, W. Shan, Y. Fan, Diethanolamine functionalized rice husk for highly efficient recovery of gallium(III) from solution and a mechanism study, Mater. Sci. Eng. C. 99 (2019) 1115–1122. https://doi.org/10.1016/j.msec.2019.02.028.

[53] R.K. Mishra, P.C. Rout, K. Sarangi, K.C. Nathsarma, A comparative study on extraction of Fe(III) from chloride leach liquor using TBP, Cyanex 921 and Cyanex 923, Hydrometallurgy. 104 (2010) 298–303. https://doi.org/10.1016/j.hydromet.2010.07.003.

[54] K.Y. Macías-Macías, A.E. Ceniceros-Gómez, M.E. Gutiérrez-Ruiz, J.L. González-Chávez, L.G. Martínez-Jardines, Extraction and recovery of the strategic element gallium from an iron mine tailing, J. Environ. Chem. Eng. 7 (2019) 102964. https://doi.org/10.1016/j.jece.2019.102964.

[55] X. Sun, Y. Sun, J. Yu, Removal of ferric ions from aluminum solutions by solvent extraction, part I: Iron removal, Sep. Purif. Technol. 159 (2016) 18–22. https://doi.org/10.1016/j.seppur.2015.12.054.

[56]F. Liu, Z. Liu, Y. Li, B.P. Wilson, M. Lundström, Recovery and separation of gallium(III) and germanium(IV) from zinc refinery residues: Part I: Leaching and iron(III) removal, Hydrometallurgy. 169 (2017) 564–570. https://doi.org/10.1016/j.hydromet.2017.03.006.

[57]Y. Xiong, X. Cui, M. Zhang, Y. Wang, Z. Lou, W. Shan, Microwave hydrothermal synthesis of gallotannin/carbon nanotube composites for the recovery of gallium ion, Appl. Surf. Sci. 510 (2020) 145414. https://doi.org/10.1016/j.apsusc.2020.145414.

[58]Y. Liu, Z. Xin, L. Tian, D. Villa-Gomez, W. Wang, Y. Cao, Fabrication of peptide-encapsulated sodium alginate hydrogel for selective gallium adsorption, Int. J. Biol. Macromol. 263 (2024) 130436. https://doi.org/10.1016/j.ijbiomac.2024.130436.

[59]S. Saikia, A. Sinharoy, P.N.L. Lens, Adsorptive removal of gallium from aqueous solution onto biogenic elemental tellurium nanoparticles, Sep. Purif. Technol. 286 (2022) 120462. https://doi.org/10.1016/j.seppur.2022.120462.

[60]P. Saha, S. Chowdhury, S. Gupta, I. Kumar, Insight into adsorption equilibrium, kinetics and thermodynamics of Malachite Green onto clayey soil of Indian origin, Chem. Eng. J. 165 (2010) 874–882. https://doi.org/10.1016/j.cej.2010.10.048.

[61]H. Li, C. Liu, Z. Peng, Q. Chen, R.M. Kasomo, Y. Jin, X. Weng, N.M. Ondiaka, Y. Chen, S. Song, Utilization of methyltrichlorosilane as a novel and efficient reagent to enhance fluorine recovery from wet-process phosphoric acid, J. Clean. Prod. 444 (2024) 141295. https://doi.org/10.1016/j.jclepro.2024.141295.

[62]K. Sun, W. Peng, H. Li, S. Song, Recovery of $Au(CN)_2^-$ with magnetic reduced graphene oxide hydrogel in aqueous leach solution, Hydrometallurgy. 176 (2018) 208–215. https://doi.org/10.1016/j.hydromet.2018.02.001.

[63]H. Di Xiao, H.L. Ma, C.S. Xue, H.Z. Zhuang, J. Ma, F.J. Zong, W.R. Hu, Thermal oxidation behaviors of GaN powders, Mater. Lett. 59 (2005) 4041–4043. https://doi.org/10.1016/j.matlet.2005.07.061.

[64]X. Liu, G. Qiu, Y. Zhao, N. Zhang, R. Yi, Gallium oxide nanorods by the conversion of gallium oxide hydroxide nanorods, J. Alloys Compd. 439 (2007) 275–278. https://doi.org/10.1016/j.jallcom.2006.08.062.

[65]W. Chen, J. Du, H. Zhang, H. Wang, K. Xu, Z. Gao, J. Tong, J. Wang, J. Xue, T. Zhi, L. Wang, Surface treatment of GaN nanowires for enhanced photoelectrochemical water-splitting, Chinese Chem. Lett. 35 (2024) 109168. https://doi.org/10.1016/j.cclet.2023.109168.

[66]Z. Li, R. Hong, T. Liu, Q. Wang, C. Tao, H. Lin, D. Zhang, The enhancement of

nonlinear absorption of Ag thin film on laser induced defective MoO_x buffer layer, Chem. Phys. Lett. 754 (2020) 137727. https://doi.org/10.1016/j.cplett.2020.137727.

[67] J. Qu, W. Liu, R. Liu, J. He, D. Liu, Z. Feng, Z. Feng, R. Li, C. Li, Evolution of oxygen vacancies in cerium dioxide at atomic scale under CO_2 reduction, Chem Catal. 3 (2023) 100759. https://doi.org/10.1016/j.checat.2023.100759.

[68] D. Zhou, B. Che, J. Kong, X. Lu, A nanocrystalline tungsten oxide electrochromic coating with excellent cycling stability prepared via a complexation-assisted sol-gel method, J. Mater. Chem. C. 4 (2016) 8041–8051. https://doi.org/10.1039/c6tc03194c.

[69] D. Chen, R. Yu, D. Wu, H. Zhao, P. Wang, J. Zhu, P. Ji, Z. Pu, L. Chen, J. Yu, S. Mu, Anion-modulated molybdenum oxide enclosed ruthenium nano-capsules with almost the same water splitting capability in acidic and alkaline media, Nano Energy. 100 (2022) 107445. https://doi.org/10.1016/j.nanoen.2022.107445.

[70] R.S. Park, H.J.K. Kim, G. Pitner, C. Neumann, S. Mitra, H.S.P. Wong, Molybdenum oxide on carbon nanotube: Doping stability and correlation with work function, J. Appl. Phys. 128 (2020) 045111. https://doi.org/10.1063/5.0013778.

[71] Y. Yan, S. Li, B. Yuan, R. Hu, L. Yang, J. Liu, J. Liu, Y. Wang, Z. Luo, H. Ying, S. Zhang, W.Q. Han, M. Zhu, Flowerlike Ti-Doped MoO_3 Conductive Anode Fabricated by a Novel NiTi Dealloying Method: Greatly Enhanced Reversibility of the Conversion and Intercalation Reaction, ACS Appl. Mater. Interfaces. 12 (2020) 8240–8248. https://doi.org/10.1021/acsami.9b20922.

[72] J.T. Ren, X.M. Wu, T. Liu, L. Chen, R. Hao, Y.J. Song, Y.P. Liu, Z.Y. Yuan, Interfacing nickel with molybdenum oxides as monolithic catalyst to accelerate alkaline hydrogen electrocatalysis with robust stability, Appl. Catal. B Environ. 317 (2022) 121786. https://doi.org/10.1016/j.apcatb.2022.121786.

[73] X. Wu, M. Yuan, X. Guo, L. Zhang, Fast Coadsorption and Selective Separation of Gallium(III) and Germanium(IV) from Aqueous Solutions by 3D Hierarchical Porous Hoya-like α-FeOOH, ACS Sustain. Chem. Eng. 7 (2019) 15939–15947. https://doi.org/10.1021/acssuschemeng.9b02199.

[74] J. Meng, C. He, Y. Li, J. Zhou, J. Li, C. Zheng, J. Zhao, T. Fujita, S. Ning, Y. Wei, Enhanced adsorption and separation of gallium using silica-based P507-TBP/SiO_2–P adsorbent from sulfuric acid solution, Microporous Mesoporous Mater. 314 (2021) 110859. https://doi.org/10.1016/j.micromeso.2020.110859.

Chapter 4. Electro-assisted preferential gallium capture at bimetallic oxide heterointerfaces

4.1. Introduction

The inherent coexisting properties of gallium result in the production being extremely constrained by the scale and economic viability of the host metals (aluminum and zinc) [1–3]. The fragility of the supply chain is becoming more apparent as demand for gallium continues to surge in the photovoltaic, telecommunications, and semiconductor sectors. Given the low feasibility of functional recycling of gallium from end-of-life products, shifting the recovery process to the discharge streams has become a critical approach to mitigate supply risks and enhance resource resilience. However, the high-volume, continuous nature of industrial wastewater demands rapid treatment cycles, while the trace gallium concentration (1-35 ppm) in complex solutions poses formidable obstacles to selective separation and efficient recovery [4–6]. Although adsorption using chemical coordination between gallium ions and chelating functional groups has attracted considerable attention [7–10], the concentration gradient in dilute streams is insufficient to provide adequate driving force for ion migration toward the adsorbent. Furthermore, the active site coverage by competing cations leads to electrostatic repulsion and pore blockage, resulting in severe kinetic limitations and reduced available capacity.

Chemisorption and electrosorption coupling (CEC) is a promising platform to overcome the low mass transfer coefficient and enhance selectivity. An applied electric field drives ion migration and induces sustained interfacial enrichment within the electrical double-layer, efficiently alleviating diffusion limitations by enhancing the local activity of target ions (Fig. 4.1a). Concurrently, chelating sites on the electrode material undergo specific coordination with target ions, reducing site loss caused by competing ions [11]. It has been demonstrated that efficient separation without preconcentration was possible for $Au(S_2O_3)_2^{3-}$, Ag^+, La^{3+}, Y^{3+}, Gd^{3+}, Cu^{2+}, Ni^{2+} [11–15]. Nevertheless, hydrogen evolution reaction is a typical competitive reaction limiting the efficiency of CEC processes. Since metals such as gallium, nickel, and rare earth elements typically require more negative cathodic polarization in electrochemical recovery (Fig. 4.1b), and protons preferentially compete for electrons and active sites,

thereby reducing the current efficiency of target ions and suppressing effective interfacial capture [16,17]. Additionally, interface poisoning induced by hydrogen evolution can alter the species distribution and coordination chemistry, further eroding available capacity and ion selectivity [18]. Therefore, achieving both efficient selective recovery of gallium ions and effective suppression of hydrogen evolution reaction has become a major challenge in cathode design for electrochemical separation.

Current research on electro-assisted gallium recovery focused on carbon-based materials (e.g., biochar-derived aerogel) that rely on electrical double-layer capacitance, in which noteworthy ion selectivity was neglected in favor of total ion capacity at high gallium concentrations [19]. In contrast, redox-active electrodes can provide opportunities to simultaneously improve ion selectivity and capture capacity across a wide concentration range through interfacial electronic buffering and dynamic coordination regulation [20,21]. Among various candidate materials, molybdenum trioxide (MoO_3) is considered a promising active component for electro-assisted gallium capture due to its tunable redox behavior and excellent electron transfer capability [22,23]. According to the Hard-Soft Acid-Base theory, the hard basic oxygen donors (*OH, *O) and hard acidic Mo centers in MoO_3 can strongly interact with gallium species ($Ga(OH)_2^+$, $Ga(OH)^{2+}$, Ga^{3+} and $Ga(OH)_4^-$) [24]. However, pure MoO_3 is prone to structural collapse and capacity fading during electrochemical cycling, and the affinity toward protons can lead to the hydrogen evolution competition under cathodic polarization [25,26]. Tin dioxide (SnO_2) possesses excellent structural stability and inertness toward hydrogen evolution [27,28]. Constructing a bimetallic oxide with MoO_3 can not only stabilize the crystalline structure of MoO_3 but also help increase the energy barrier for the hydrogen evolution reaction. Meanwhile, electron rearrangement induced by the n-n heterojunction can modulate the electron density and oxygen coordination microenvironment around Mo sites. And oxygen vacancies introduced by the lattice mismatch between MoO_3 and SnO_2 serve as additional coordination sites for gallium ions adsorption [24,29–31]. Although the MoO_3/SnO_2 bimetallic oxide as the CEC electrode offers a promising platform for coupling electric-field-driven ion enrichment with interfacial specific recognition, thereby enabling selective gallium recovery beyond conventional electrical double-layer storage, limited information is available regarding the recovery performance and preferential immobilization mechanism under hydrogen evolution suppression.

Here, we constructed an asymmetric CEC platform centered on the MoO_3/SnO_2

heterostructure for efficient and selective recovery of gallium ions from dilute streams (Fig. 4.1c). The key role of SnO_2 in mitigating parasitic hydrogen evolution-induced interface poisoning and enhancing current efficiency of gallium was systematically elucidated. The facile electrochemical switching behavior of the MoO_3/SnO_2 adsorbent provided kinetic support for the directional enrichment and efficient immobilization of trace gallium. Under optimized microenvironments, the stepwise separation strategy implemented via potential modulation was evaluated for gallium selective recovery amidst coexisting common competing metals (Al, Pb, Zn and Ge). Combining electrochemical analysis with multielement valence state characterization, this study systematically elucidated the gallium separation mechanism driven synergistically by electro-assisted interfacial enrichment and oxygen coordination immobilization, providing a theoretical framework for designing efficient electrochemical separation systems for low-concentration critical metals.

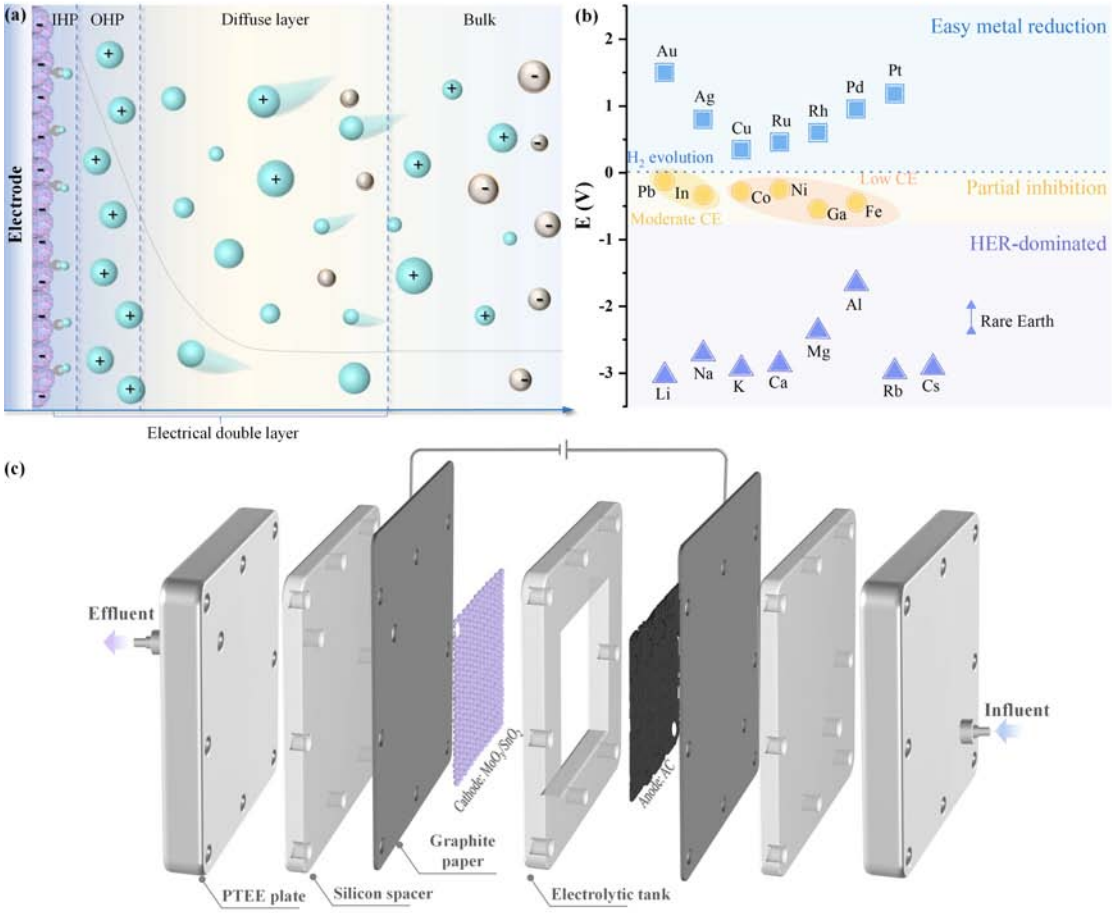


Fig. 4.1 (a) Schematic of ion migration driven by electric fields and enrichment at the electrical double-layer interface during CEC process. The electrochemical interface structure is commonly partitioned into five distinct regions: electrode, inner

Helmholtz plane (IHP), outer Helmholtz plane (OHP), diffusion layer, and bulk. (b) General electrochemical features of corresponding metals (standard reduction potentials referenced from CRC Handbook of Chemistry and Physics) (c) Configuration of the customized recovery cell.

4.2. Experimental section

4.2.1. Reagents and materials

Sodium molybdate dihydrate ($Na_2MoO_4•2H_2O$), oxalic acid ($H_2C_2O_4$), tin dichloride ($SnCl_2$), zinc nitrate hexahydrate ($Zn(NO_3)_2•6H_2O$), copper nitrate trihydrate ($Cu(NO_3)_2•3H_2O$), aluminum nitrate nonahydrate ($Al(NO_3)_3•9H_2O$), sulfuric acid (H_2SO_4), nitric acid (HNO_3), sodium hydroxide (NaOH) were supplied by Sinopharm Chemical Reagent Co., Ltd., China. Gallium nitrate ($Ga(NO_3)_3•xH_2O$), gallium sulphate ($Ga_2(SO_4)_3•xH_2O$) hydrate, gallium chloride ($GaCl_3•xH_2O$) and standard solutions (gallium, germanium, lead, 1000 μg mL^{-1} in 1mol L^{-1} HNO_3) were purchased from Aladdin Co., Ltd (Shanghai, China). Conductive carbon black was obtained from the Cabot Corporation.

4.2.2. Fabrication of composite MoO_3/SnO_2 electrodes

Hydrothermal preparation of MoO_3, SnO_2 and composite MoO_3/SnO_2 involved only analytical grade reagents. 4 mL of H_2SO_4 (35% v/v) and 11.0 mmol of oxalic acid ($H_2C_2O_4$) were sequentially added to 40 mL of the aqueous solution containing sodium molybdate dihydrate ($Na_2MoO_4•2H_2O$, 4.8 mmol). Stannous chloride ($SnCl_2$, 1.2, 2.4, 3.6 and 4.8 mmol) was added with continuous stirring for 30 min and then the resulting brown solution was transferred to the autoclave and reacted at 200 °C for 24 h. The composites were labeled by the Sn/Mo ratio. Analogously, MoO_3, SnO_2 were prepared except without the addition of $SnCl_2$ and $Na_2MoO_4•2H_2O$, respectively.

MoO_3/SnO_2 (cathode)/commercial activated carbon (anode), conductive carbon black and polyvinylidene fluoride (dissolved in dimethylacetamide) in the mass ratio of 8:1:1 were sufficiently grinded. The mixed samples were subsequently sprayed onto 5 cm × 5 cm graphite paper and dried at 60 °C for 10 h. The loadings of the samples were weighed before testing and were approximately 37.9 ± 2.0 mg.

4.2.3. Chemisorption and electrosorption coupling recovery experiments

Gallium ions recovery experiments were conducted in the customized electrolytic

cell connected to an external constant voltage power supply, with the effective volume of 25 cm^3 (Fig.4.1c). The asymmetric electrode configuration consisted of MoO_3/SnO_2 as the cathode and commercial activated carbon as the anode. A total of 100 mL of electrolyte was circulated between an external reservoir and the cell using a peristaltic pump at a flow rate of 7.5 mL min^{-1}, ensuring continuous contact between the gallium-containing solution (0.5-200.0 mg L^{-1}) and the electrodes under controlled hydrodynamic conditions. Gallium ion concentration in periodically collected 2 mL aliquots was determined using Atomic Absorption Spectrophotometry (AAS, Shimadzu AA-6680, Japan), and the corresponding adsorption efficiency and capacity normalized by the cathode material mass were calculated by Eq. 4.1 and Eq. 4.2. The current was monitored in real-time throughout the experiment to calculate the current efficiency (Eq. 4.3) [32].

$$A = \frac{(C_0 - C_e)}{C_0} \times 100\% \tag{4.1}$$

$$q_e = \frac{(C_0 - C_e)V}{m} \tag{4.2}$$

$$Current\ efficiency = \frac{n \times M \times F}{Q_{total}} \times 100\% \tag{4.3}$$

Where C_0, C_e (mg L^{-1}) represent initial concentration and residual concentration after 240 min, respectively. V (L) is the volume of solution, and m (g) indicates the mass of cathode. M (mol) is the total amount of gallium recovery, F is the Faraday constant (96485 C mol^{-1}), Q_{total} is the total charge passed during recovery, and n is the charge transfer number.

4.2.4. Characterization of composite MoO_3/SnO_2

The surface morphology of the electrode material was obtained using a SEM (ZEISS GeminiSEM 300) operated at an accelerating voltage of 3 kV and equipped with an EDS with an accelerating voltage of 15 kV. Field emission transmission electron microscopy and the associated scanning energy dispersive spectroscopy (FETEM-EDS) were performed at 300 kV by FEI Tecnai G2 F30 (FEI Co. Ltd, America).The crystal structure and chemical composition of samples were characterised by X-ray diffractometer of Cu Kα radiation (XRD, Rigaku SmartLab SE, Japan), X-ray photoelectron spectroscopy (XPS, Thermo Scientific K-Alpha, USA), and Fourier transform infrared spectroscopy (FTIR, Thermo Scientific Nicolet iS20, USA).

4.2.5. Electrochemical tests

Electrochemical tests were performed with a VersaSTAT-450 (PAR, America) electrochemical workstation using a typical three-electrode configuration consisting of a working electrode of 1 cm × 1 cm graphite paper coated with MoO_3/SnO_2, a counter electrode of 1 cm × 1 cm platinum plate, and a reference electrode Ag/AgCl in 3 M KCl. All potentials measured against Ag/AgCl were converted to the reversible hydrogen electrode (RHE) scale by: E (vs. RHE) = E (vs. Ag/AgCl) + 0.197 V + 0.0591×pH. Linear scanning voltammetry (LSV), cyclic voltammetry (CV), electrochemical impedance spectroscopy (EIS) and chronoamperometry were conducted following stabilization of the open circuit potential. Given the temperature dependence of the charge transfer resistance (R_{ct}), variable-temperature EIS tests were performed at 25, 35, 45, 55 °C to determine the activation energy for chemisorption and electrochemical coupling recovery of gallium ion. The electrochemical interfacial behavior of the gallium recovery process was further analyzed by chronocoulometry. The electrolyte was obtained from the analytical grade gallium standard solution (1000 μg mL^{-1} in 1 M HNO_3), with the pH adjusted to 3.0 corresponding to the recovery experiment.

In the equivalent circuit, R_{ct} represents the charge-transfer resistance associated with electron exchange at the electrode/electrolyte interface (Eq. 4.4), whose relationship with temperature follows the Arrhenius equation:

$$ln\, R_{ct} = ln\, R_0 - \frac{E_a}{RT} \tag{4.4}$$

where R_{ct} is the charge transfer resistance; R_0 is the preexponential factor; E_a is the apparent activation energy; T (K) represents the temperature; and R is the ideal gas constant (8.314 J mol^{-1} K^{-1})

4.2.6. Randles-Sevcik

For irreversible, diffusion-controlled processes, the Randles-Sevcik equation can be expressed as follows:

$$I_p = (2.99 \times 10^5)\, n\, (\alpha n_\alpha)^{1/2}\, D^{1/2}\, C_0^{\infty}\, v^{1/2} \tag{4.5}$$

where I_p, n, α, n_α, C_0^{∞}, D, and v are the current of the cathodic peak, number of exchanged electrons involved in the electrode process, charge transfer coefficient, number of electrons in the rate-determining step, the solution bulk concentration, diffusion coefficient, and the potential scanning rate, respectively.

4.2.7. Double potential step chronocoulometry

Double potential step chronocoulometry is a powerful technique for determining the adsorption of electroactive species on an electrode surface. And it enables the distinction between the charge used for electro-adsorbed substances and the charge used for components in the electrolytic solution. The relationship between charge and the square root of time is given as follows:

$$Q\ (t \leq \tau) = \frac{2nFAC\sqrt{Dt}}{\sqrt{\pi}} + Q_{dl} + nFA\Gamma \tag{4.6}$$

$$Q_r\ (t > \tau) = \frac{2nFAC\sqrt{D}}{\sqrt{\pi}} \times \left[\tau^{1/2} + (t-\tau)^{1/2} - t^{1/2}\right] + Q_{dl} \tag{4.7}$$

$$Q_{ads} = nFA\Gamma \tag{4.8}$$

Where Q and Q_r represent the charges corresponding to the forward and reverse reactions, respectively, τ denotes the potential step time, t is the double layer charging time, n is the number of electrons transferred, F is the Faraday constant, A is the geometric surface area, C is the bulk concentration of reactants, D is the diffusion coefficient, Γ is the electrode surface coverage and Q_{dl} is the double layer charge.

Double step chronocoulometry predicts that adsorption is negligible when the Q-$t^{1/2}$ and Q_r-θ plots [$\theta = \tau^{1/2} + (t-\tau)^{1/2} - t^{1/2}$] intersect at $Q = 0$ and have identical slopes and intercepts, where τ is the duration of the first potential step. In contrast, when reactant adsorption occurs, the Q-axis intercept of the Q-$t^{1/2}$ plot is larger than that of the Q_r-θ plot. The difference between these two Q-axis intercepts corresponds to the charge due to adsorption of reactant species, thereby providing a measure of the adsorbed amount.

4.3. Results and discussion

4.3.1. Characterization of composite MoO_3/SnO_2

The interpenetrating nanoscale heterostructure of MoO_3/SnO_2 was engineered through hydrothermal synergistic nucleation and confined growth (Fig. 4.2a). Strikingly distinct from the bundled nanobelt assemblies of MoO_3 (Fig. 4.3a) and bulk SnO_2 (Fig. 4.3b), composite MoO_3/SnO_2 obtained at Sn/Mo ≤ 0.5 exhibited the loosely packed, mesoporous nanoparticle architecture composed of ultra-small nanocrystals (Figs. 4.3c and d). The morphology was enabled by the multidentate coordination of $H_2C_2O_4$ with Mo^{6+} and Sn^{2+}, which generated stable chelate complexes that deliberately slowed crystallization kinetics, thereby favoring heterogeneous self-assembly. At the

Sn/Mo ratio of 0.75, the high nucleation density of SnO_2 in conjunction with near-saturation growth conditions, promoted Ostwald ripening [33]. This cooperative process drove the structural evolution from loosely aggregated nanocrystals toward energetically minimized spherical nanoparticles (Fig. 4.3e). Notably, the incorporation of SnO_2 effectively suppressed the excessive crystal growth of MoO_3, inducing *in-situ* nanocrystallization of composite MoO_3/SnO_2. And the abundant grain boundaries and heterointerface defects within the nanocrystalline framework not only accelerated charge transfer but also provided additional coordination adsorption sites for gallium ions [31].

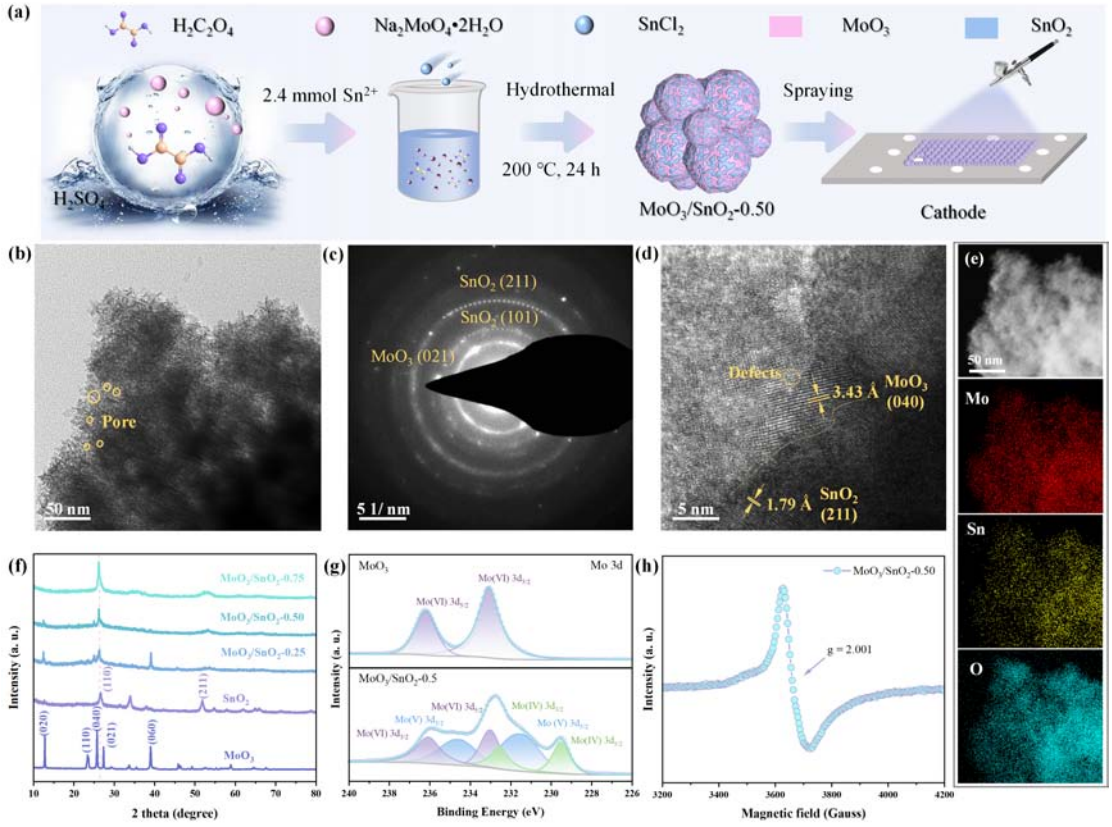


Fig. 4.2 (a) Design of MoO_3/SnO_2 electrode with redox functionality, (b) TEM image, (c) SAED pattern, (d) HRTEM image, (e) TEM image and corresponding elemental mapping of MoO_3/SnO_2-0.50. (f) XRD spectra of MoO_3, SnO_2, MoO_3/SnO_2-0.25, MoO_3/SnO_2-0.50 and MoO_3/SnO_2-0.75. (g) Deconvoluted high-resolution XPS spectra of Mo 3d of MoO_3 and MoO_3/SnO_2-0.50. (h) EPR spectrum of MoO_3/SnO_2-0.50.

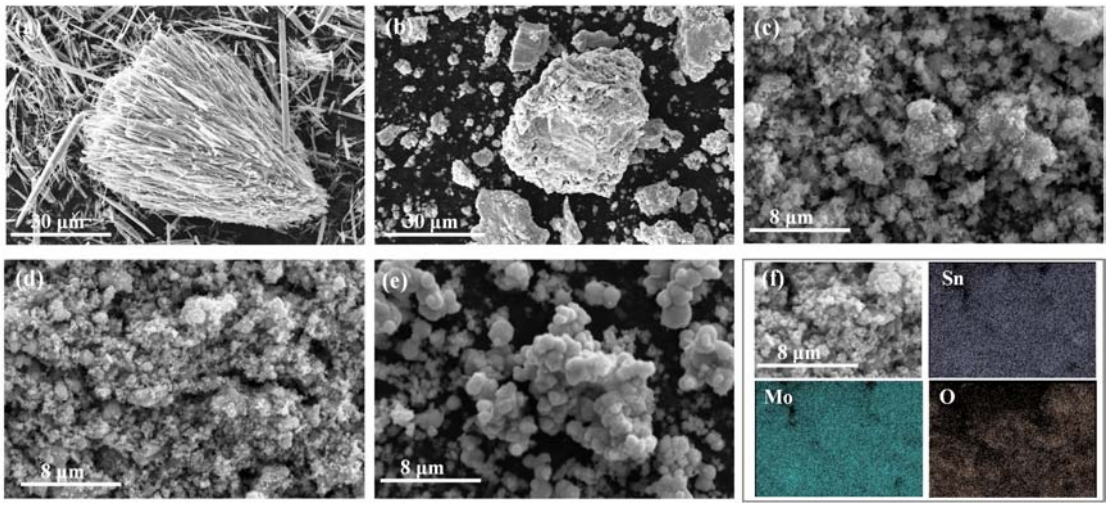


Fig. 4.3 SEM images of (a) MoO_3, (b) SnO_2, (c) MoO_3/SnO_2-0.25, (d) MoO_3/SnO_2-0.50, (e) MoO_3/SnO_2-0.75 and (f) EDS element mapping images of MoO_3/SnO_2-0.50 for Mo, Sn, O.

The coexistence of MoO_3 and SnO_2 crystal domains was simultaneously detected in transmission electron microscope (TEM) and selected area electron diffraction (SAED) tests (Figs. 4.2b and c). Analogously, high-resolution TEM (HRTEM) images showed lattice spacings of 3.38 Å and 3.43 Å for the (021) and (040) crystal planes of MoO_3. Lattice spacings of 1.79 Å, 2.56 Å and 3.38 Å were observed, corresponding to the (211), (101), and (110) crystal planes of SnO_2, respectively (Figs. 4.2d and 4.4). The oxophilic species SnO_2 were anchored into the MoO_3 framework, leading to conspicuous small size effect and lattice distortions [22]. Energy dispersive spectrometer (EDS) elemental mapping analysis confirmed the uniform spatial distribution of Mo, Sn, and O, unambiguously evidencing the formation of integrated nanoscale heterointerfaces (Fig. 4.2e and 4.3f).

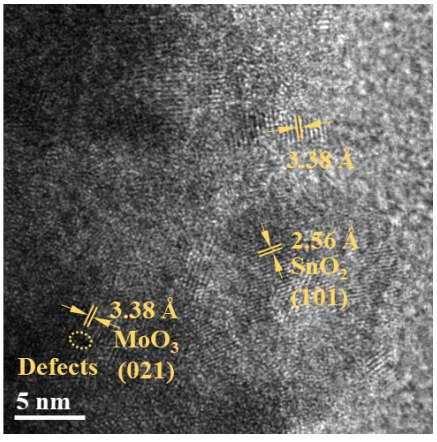


Fig. 4.4 HRTEM image of MoO_3/SnO_2-0.50.

X-Ray diffraction analysis (XRD) patterns of composite MoO_3/SnO_2 displayed well-matched characterized diffraction peaks assignable to α-MoO_3 (ICDD No. 97-015-8256) and rutile-SnO_2 (ICDD No. 98-000-0151) (Fig. 4.2f), with no extraneous reflections within the detection limit, evidencing high phase purity and well-defined biphasic architecture. The characteristic peaks of SnO_2 (110) and (211) gradually intensified with increasing Sn/Mo ratio, and the overlapped 26.0-27.5° envelope evolved from α-MoO_3 (021, 27.3°) to SnO_2 (110, 26.6°) dominant feature. During compositing, Sn^{2+} was oxidized to Sn^{4+} under acidic condition and intercalated or partially substituted into the interlayer or lattice of α-MoO_3, coordinating with symmetrical bridging oxygen in the host α-MoO_3 to form octahedral structures [22,34]. The collective low-angle shifts, attenuation, and broadening of $(020)_{MoO_3}$, $(040)_{MoO_3}$, $(021)_{MoO_3}$, and $(060)_{MoO_3}$ diffraction peaks in the XRD pattern of composite MoO_3/SnO_2, and the red-shifting and attenuation of the Mo=O stretching vibration peak in fourier transform infrared spectroscopy (FT-IR) (Fig. 4.5), were attributed to lattice expansion and local distortion due to the difference in ionic radii ($Mo^{6+} \approx 0.065$ nm < $Sn^{4+} \approx 0.067$ nm) [29].

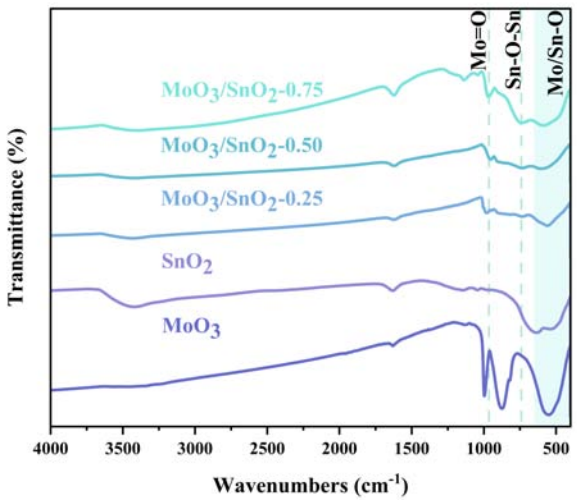


Fig. 4.5 FT-IR spectra of MoO_3, SnO_2, MoO_3/SnO_2-0.25, MoO_3/SnO_2-0.50 and MoO_3/SnO_2-0.75.

High-resolution Sn 3d X-ray photoelectron spectroscopy (XPS) showed that both deconvoluted peaks centered at 495.08 eV and 486.68 eV were assigned to $3d_{3/2}$ and $3d_{5/2}$ of Sn(IV) (Fig. 4.6a) with binding energies lower than the pure SnO_2, which was

potentially related to band bending and electron rearrangement induced by Fermi level alignment [34,35]. Regarding the pure α-MoO_3, two deconvoluted peaks at 236.18 eV and 233.08 eV corresponded to spin-orbit splitting of Mo(VI) $3d_{3/2}$ and Mo(VI) $3d_{5/2}$, respectively (Fig.4.2g). Impressively, the negative shifts of 0.10 eV and 0.04 eV of Mo(VI) deconvoluted peaks were observed in the high-resolution Mo 3d XPS spectrum of MoO_3/SnO_2-0.50, accompanied by distinct Mo(V) and Mo(IV) deconvoluted peaks, which provided direct evidence for the occurrence of electron transfer at the composite interface. The interfacial electron transfer rendered the MoO_3/SnO_2-0.50 junction region a locally electron-rich environment conducive to oxygen vacancy formation, as evidenced by the appearance of oxygen vacancies at 531.24 eV in the O 1s XPS spectrum (Fig. 4.6b) and the characteristic electron paramagnetic resonance (EPR) signal near g = 2.001 (Fig. 4.2h) [36–38]. Additionally, the overall negative shift in the Mo-O and Sn-O peaks attributable to lattice oxygen further indicated that the electron-rich environment at the composite MoO_3/SnO_2-0.50 interface weakened the effective ionicity of lattice oxygen and enhanced final-state screening. In conclusion, the XPS results provided a compelling demonstration of the successful construction of the electron-modulated heterointerface rich in active defects within the composite MoO_3/SnO_2-0.50, which was crucial for enhancing both the surface reactivity and electrical conductivity of the composite.

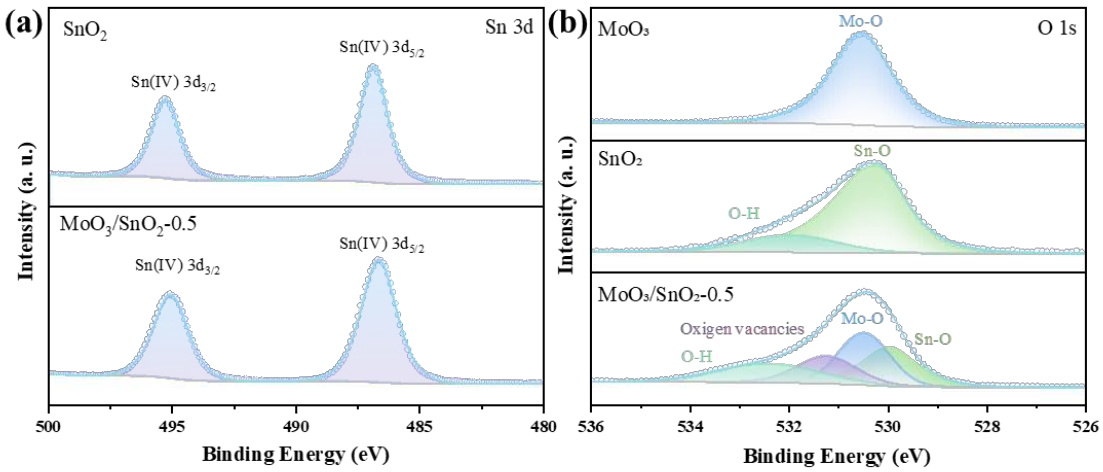


Fig. 4.6 Deconvoluted high-resolution XPS spectra of (a) Sn 3d and (b) O1s of MoO_3, SnO_2 and MoO_3/SnO_2-0.50.

4.3.2. Selective suppression of hydrogen evolution reaction

To evaluate the selective regulation of cathodic competitive reactions by MoO_3, SnO_2, and the composite MoO_3/SnO_2 in gallium-containing acidic electrolytes, iR-corrected LSV measurements were performed with the standard three-electrode system (Fig. 4.7a). We hypothesized that an ideal cathode should suppress hydrogen evolution without compromising interfacial charge transport and reaction activity, enabling the directional allocation of electrons toward the gallium ions recovery process. With the gradual introduction of SnO_2, the current density of the MoO_3/SnO_2 electrodes progressively decreased over a wide potential window. At -0.56 V vs RHE, corresponding to the Ga^{3+}/Ga reduction potential [16], the current densities of MoO_3/SnO_2-0.25, MoO_3/SnO_2-0.50, and MoO_3/SnO_2-0.75 were 1.98 $mA \cdot cm^{-2}$, 1.31 $mA \cdot cm^{-2}$, and 0.29 $mA \cdot cm^{-2}$, respectively, significantly lower than MoO_3 (3.66 mA cm^{-2}). Meanwhile, the overpotential of the MoO_3/SnO_2 electrode at 10 mA cm^{-2} was higher than that of MoO_3 (1.09 V). Gallium ions might be preferentially enriched at the heterointerface and occupy active sites, significantly obstructing the proton reduction pathway, thereby requiring a higher overpotential to sustain the same current density [27,39,40]. The characteristic hydrogen reduction peak near 0.013 V in the CV curve was markedly attenuated for the composite electrodes compared to MoO_3 (Fig. 4.7b), further confirming the dominant contribution of SnO_2 in suppressing hydrogen evolution reaction. Conversely, the pronounced enhancement of the Ga^{3+} reduction peak at -0.541 V was particularly observed for the MoO_3/SnO_2-0.50 and MoO_3/SnO_2-0.75. The positive shift of the Ga^{3+} reduction peak was associated with the electronic rearrangement at the MoO_3/SnO_2 interface resulting from the locally electron-rich environment, thereby lowering the Ga^{3+} reduction energy barrier and improving reduction selectivity.

MoO_3/SnO_2-0.50 possessed the lowest charge transfer resistance (R_{ct}, 1.34 Ω) and solution resistance (R_{Ω}, 40.29 Ω) according to EIS results. The appropriate amount of SnO_2 could form the electronically coupled heterointerface with MoO_3, and the disordered structure generated more active unsaturated oxygen atoms, thus effectively reducing the charge transfer barrier (Fig. 4.7c and Table 4.1). The elevated slope in the low-frequency region of the Nyquist plot provided compelling evidence for enhanced reactant diffusion and accelerated interfacial reaction rate [19]. Consequently, the superior gallium recovery performance of the MoO_3/SnO_2-0.50 electrode could be attributed to the enhanced conductivity, transfer coefficient, and interfacial reaction

kinetics. To further elucidate the electrochemical response characteristics of the MoO_3/SnO_2-0.50 in gallium-containing systems, CV measurements were conducted in both gallium-containing and gallium-free electrolytes, with comparisons to the graphite-based electrode (Fig. 4.7d). Under identical scan potentials, the current response in the gallium-free electrolyte was notably weaker than in the gallium-containing system, accompanied by a faint hydrogen reduction peak. Further analysis revealed that the current response in the gallium-containing system primarily originated from Ga^{3+} reduction or interface adsorption rather than the hydrogen evolution reaction. The graphite substrate showed negligible reduction features under the same conditions, ruling out substrate effects.

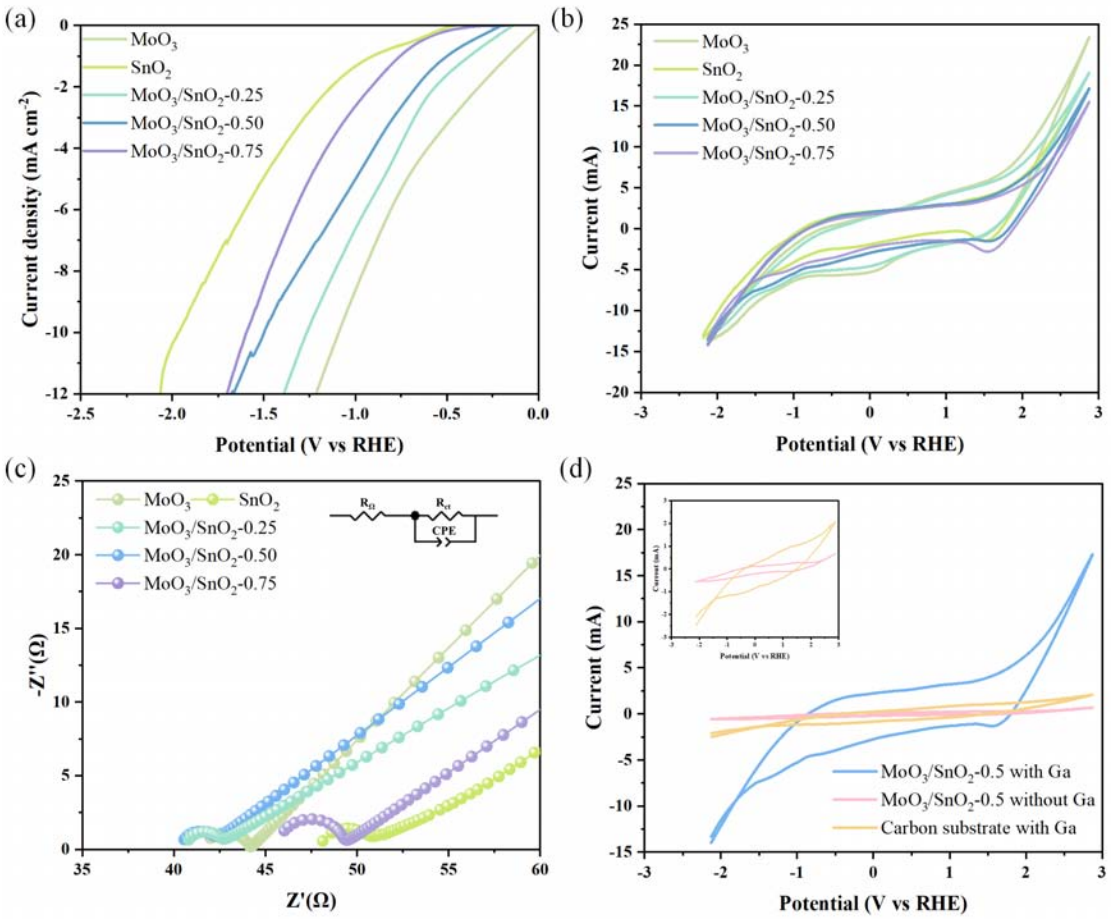


Fig. 4.7 (a) Polarization curves (with iR correction) and (b) CV curves of MoO_3, SnO_2, MoO_3/SnO_2-0.25, MoO_3/SnO_2-0.50 and MoO_3/SnO_2-0.75 electrodes at different applied potentials in gallium-containing electrolyte at a scan rate of 5 mV s^{-1}. (c) Nyquist plots of various electrodes. (d) CV curves of MoO_3/SnO_2-0.50 and graphite substrate electrodes in different electrolytes.

Table 4.1 Fitted electrochemical impedance spectroscopy (EIS) parameters of different electrodes

Electrode	MoO_3	SnO_2	MoO_3/SnO_2-0.25	MoO_3/SnO_2-0.50	MoO_3/SnO_2-0.75
R_Ω	41.60	48.05	40.55	40.29	45.67
R_{ct}	2.51	3.05	1.42	1.34	3.22

4.3.3. Gallium uptake capacity and electrode evaluation

The electrochemical recovery performance of gallium ions in the asymmetric CEC system with the activated carbon as the fixed anode and the various materials as the cathode was estimated based on the constant applied voltage of 1.8 V. The mass used in the calculation accounted for the cathode material and any possible binder. The asymmetric system employing MoO_3/SnO_2-0.50 as the cathode exhibited the highest gallium recovery efficiency (99.8%) and capacity (145.5 mg g^{-1}), which were almost 4.8%-14.4% and 7.5%-31.1% increases, respectively, over that of other cathode materials (Fig. 4.8a). Asymmetric redox-electrode systems have demonstrated outstanding application potential in high-performance electrochemical separation processes for precious metals, heavy metals, and organic pollutants. The separation behavior primarily relies on specific chemical bonding formed between target ions and redox active sites, rather than non-specific uptake within the double layer at the electrode-electrolyte interface [18,20]. Given the sluggish reaction kinetics and low current efficiency (62.3%) observed for MoO_3/SnO_2-0.75 (Fig. 4.8b), it is reasonable to infer that although the excessive SnO_2 incorporation effectively enhanced the interfacial resistance to hydrogen evolution and simultaneously diluted the redox active sites (e.g., Mo^{6+}) available for gallium ions adsorption and nucleation. The current efficiency for gallium ions recovery using MoO_3/SnO_2-0.25 as the cathode, calculated from charge obtained via chronoamperometry (Fig. 4.9) and Eq. 4.3, was significantly lower than that of MoO_3/SnO_2-0.50 (77.2%), owing to substantial electron consumption by competing side reaction. Therefore, precise control of SnO_2 content was essential for achieving an optimal electrochemical equilibrium between hydrogen suppression and gallium promotion, which fundamentally underpinned the superior recovery and current efficiency of the MoO_3/SnO_2-0.50 system.

The time-dependent recovery behaviors of MoO_3/SnO_2-0.50 toward low-concentration gallium ions (50 mg L^{-1}) were fitted using pseudo-first-order (PFO) and pseudo-second-order (PSO) kinetic models under both conventional adsorption and

CEC conditions (Fig. 4.8c). Conventional adsorption reached equilibrium at 240 min, with PSO exhibiting superior correlation coefficient compared to PFO, indicating that about 36.1% of the gallium uptake was governed by chemisorption involving surface complexation [41]. Contrastingly, gallium ions were rapidly recovered at an initial rate of 54 mg g^{-1} h^{-1} in the CEC system, reaching equilibrium after approximately 180 min. The excellent agreement of both kinetic models with experimental data suggested that the electro-assisted recovery process was synergistically controlled by both physical and chemical adsorption. The apparent activation energy of 22.1 kJ mol^{-1} calculated from temperature-dependent EIS results reflected the low energy barrier for interfacial charge transfer, endowing the system with highly efficient reaction kinetics even under mild conditions (Fig. 4.10) [42].

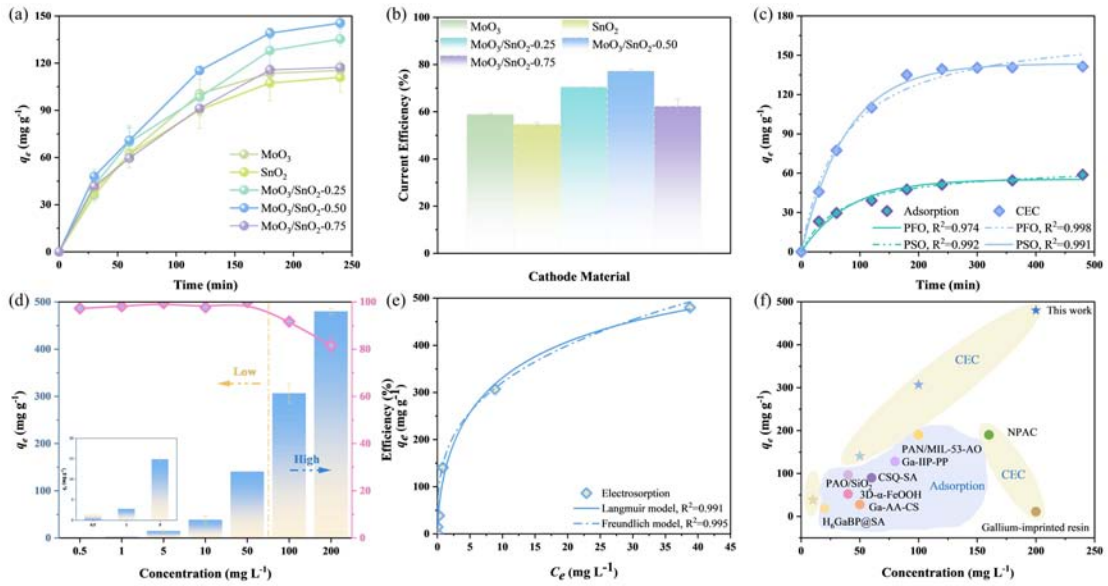


Fig. 4.8 (a) Electrochemical recovery performance and (b) current efficiency of gallium in asymmetric CEC systems with different cathodes under constant applied voltage of 1.8 V. (c) Gallium recovery kinetics in traditional adsorption and CEC processes. (d) Gallium recovery performances at various concentrations. (e) Langmuir and Freundlich isotherm models for gallium recovery. (f) Comparison of gallium recovery capacity with previous literatures.

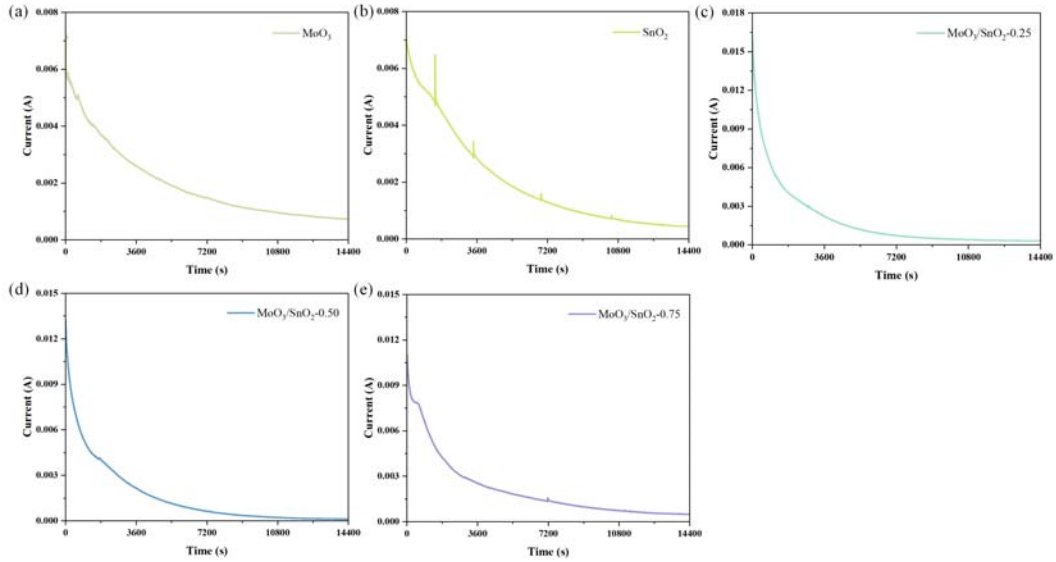


Fig. 4.9 Chronoamperometry tests of (a) MoO_3, (b) SnO_2, (c) MoO_3/SnO_2-0.25, (d) MoO_3/SnO_2-0.50 and (e) MoO_3/SnO_2-0.75 during the gallium recovery process.

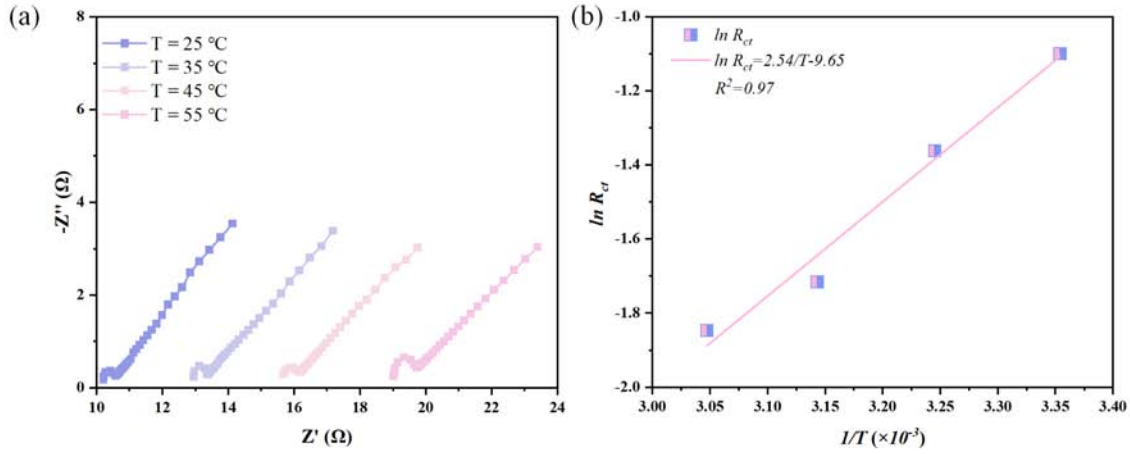


Fig. 4.10 (a) Nyquist plots of MoO_3/SnO_2-0.50 at different temperatures and (b) fitting curve between lnR_{ct} and $1/T$.

Isotherm experiments further demonstrated the advantages of the CEC system in gallium uptake. As the initial concentration increased, the adsorption capacity of MoO_3/SnO_2-0.50 toward gallium ions gradually increased (Figs. 4.8d and 4.11). Within the concentration range of 0.5 to 200.0 mg L^{-1}, gallium recovery efficiencies exceeding 81.7% were achieved within 8 h, corresponding to recovery capacities of 1.5-486.3 mg g^{-1}. Notably, even at trace initial concentrations of 0.5 and 1.0 mg L^{-1}, the recovery efficiencies reached 97.3% and 98.2%, respectively, with rapid kinetics evidenced by reaching 81.5% and 82.0% of saturation capacity within 1 h. The equilibrium

adsorption capacities were further fitted using the Langmuir and Freundlich isotherm models (Fig. 4.8e). In comparison, the superior fit of the Freundlich model ($R^2 = 0.995$) revealed that the CEC process involved multi-site adsorption on the heterogeneous interface, consistent with the synergistic interaction between electric-field-induced electrical double-layer storage and oxygen-coordination-mediated chemisorption at the bimetallic oxide heterointerface [11]. The adsorption intensity (*1/n*) of 0.31 provided strong evidence of the high adsorption affinity for gallium ions [19,43], enabling the electrode to maintain substantial adsorption capacity at low equilibrium concentrations. Comprehensive comparison with previously reported adsorbents and electrochemical systems (Fig. 4.8f) demonstrated that the MoO_3/SnO_2-0.50 electrode achieved outstanding recovery rates and capacities, particularly in treating dilute streams, positioning CEC as a promising technology for gallium recovery [8,9,19,49,53–59].

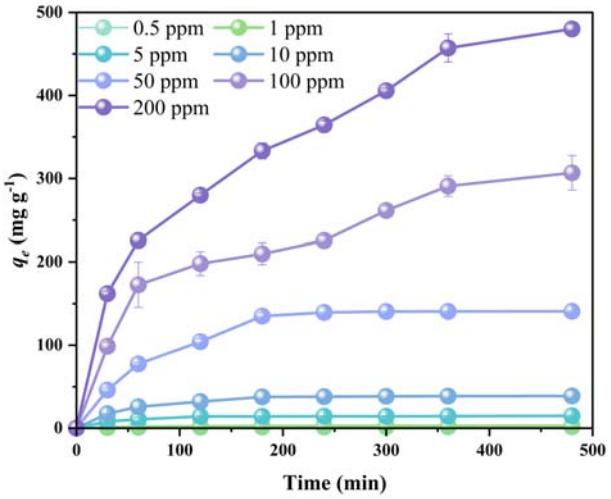


Fig. 4.11 Recovery performance of gallium ions at different initial concentrations (pH = 3.0, 100 mL, 1.8 V, 240 min).

The regenerative performance of the electrode material is crucial for the application of the CEC method. Polarity reversal after ion adsorption is generally considered an effective strategy for electrode regeneration. However, only 9.7% of the gallium was released under reverse polarization conditions at 1.8 V. The gallium capture mechanism on the MoO_3/SnO_2-0.50 electrode differs from the reversible ion storage in capacitive deionization, which is mainly governed by electrical double-layer adsorption or ion intercalation [44,45]. Specifically, gallium species form stable Ga-O-Mo/Sn inner-sphere coordination with oxygen sites at the MoO_3/SnO_2-0.50 heterointerface,

and polarity reversal alone is insufficient to dissociate these coordination bonds. On the other hand, the membrane-free configuration allows part of the released gallium species to migrate to the counter electrode and undergo re-adsorption under reversed polarization, further reducing the desorption efficiency [46,47]. Mild elution with nitric acid (0.1 M) protonated the oxygen-containing binding sites and altered the interfacial coordination equilibrium, enabling efficient gallium desorption with efficiencies exceeding 92.2% within 60 min (Fig. 4.12a). Although a slight decline in recovery efficiency and capacity was observed after four successive adsorption-desorption cycles, 76.7% of gallium ions remained recoverable. Quantitative analysis of Mo and Sn in the electrolyte after acid elution showed that SnO_2 exhibited excellent structural stability, with Sn dissolution loss only on the order of 10^{-3}% (Fig. 4.12b). Limited Mo dissolution occurred from the MoO_3/SnO_2-0.50 heterostructure during regeneration, with a loss of approximately 0.6-1.0%, which may partly account for the attenuation in gallium recovery performance. Furthermore, the repeated formation and dissociation of Ga-O-Mo/Sn coordination bonds may induce local lattice strain, weaken structural continuity, and lead to sluggish recovery kinetics [24]. Nevertheless, the electrode maintained a high recovery capacity (>102.7 mg g^{-1}), outperforming reported adsorbents such as amide-functionalized cellulose [48], P507/disordered mesoporous carbon [10,49] and polymeric resins [50].

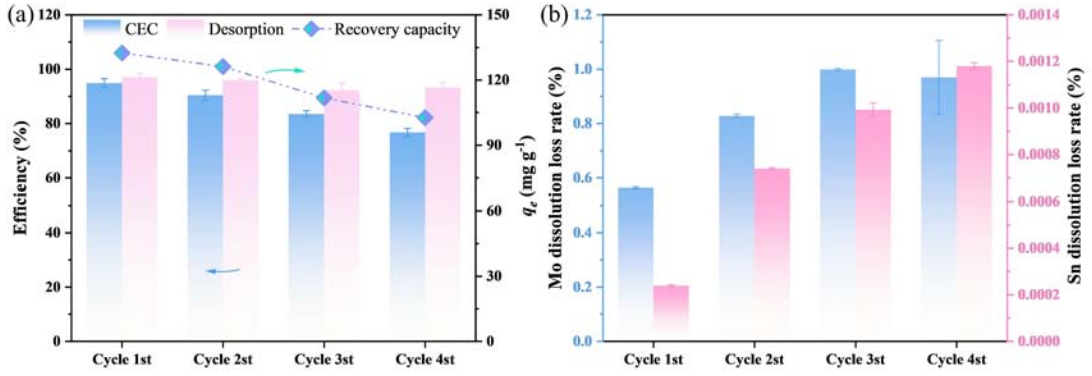


Fig. 4.12 (a) Cycling gallium recovery performance of the MoO_3/SnO_2-0.50 cathode. (b) Mo and Sn dissolution losses from the cathode during the acid elution process.

SEM-EDS characterization of the cathode after desorption showed that the electrode retained the rough particulate morphology observed before gallium recovery, with slight structural collapse and localized physical detachment (Figs. 4.13 and 4.14), suggesting that the performance decline was more likely related to partial structural

damage and reduced accessible active sites. After 20 consecutive CV scans, nearly overlapping redox curves were observed, corresponding to the stable morphology and charge-transfer pathways under repeated polarization conditions (Fig. 4.15). The good structural resilience and electrochemical endurance collectively endow MoO_3/SnO_2-0.50 with application potential for efficient gallium recovery. Future improvements in long-term cycling stability require the simultaneous optimization of electrode architecture and regeneration mode. Electrodes fabricated via in situ electrochemical growth can reduce physical detachment by reinforcing interfacial adhesion between the active material and the substrate [51], while strategies such as pulsed or stepwise reversed polarization in membrane-assisted recovery cells and dilute-acid-assisted electrochemical elution are expected to reduce acid consumption and improve regeneration efficiency [46,52].

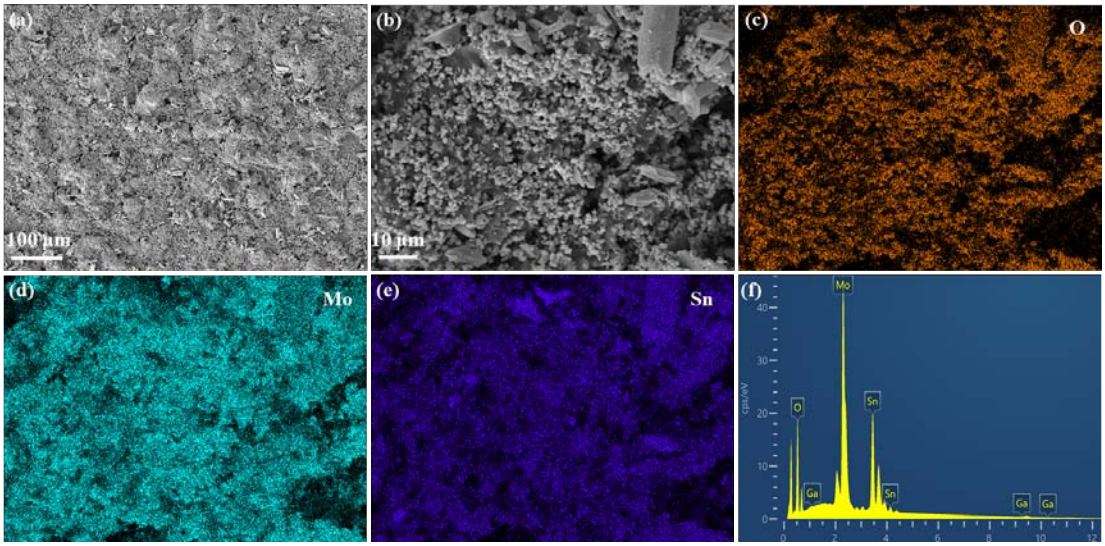


Fig. 4.13 (a,b) SEM images, corresponding EDS elemental mappings of (c) O, (d) Mo, and (e) Sn, and (f) map sum spectrum of the MoO_3/SnO_2-0.50 cathode before gallium recovery.

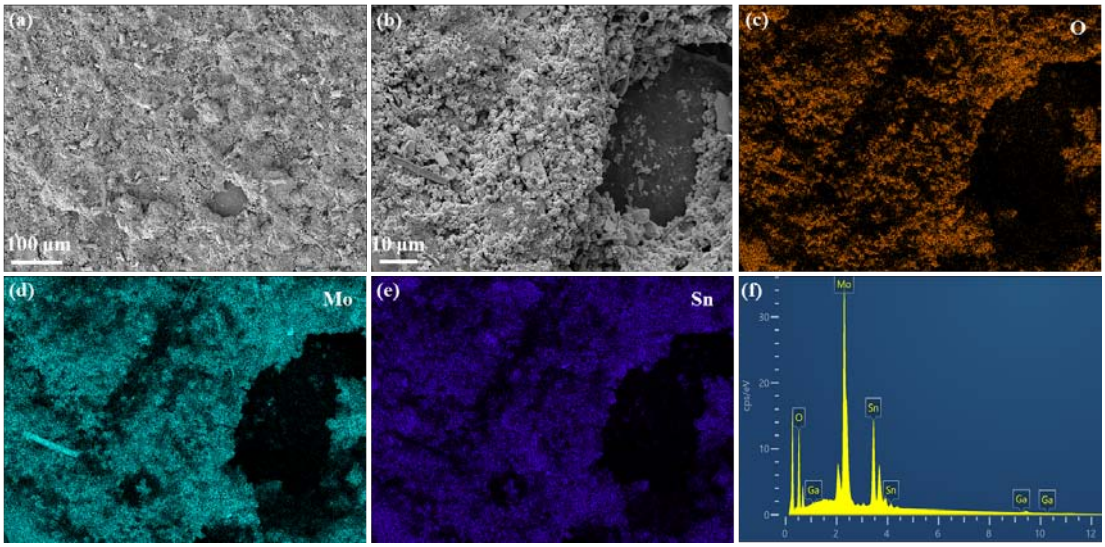


Fig. 4.14 (a,b) SEM images, corresponding EDS elemental mappings of (c) O, (d) Mo, and (e) Sn, and (f) map sum spectrum of the MoO_3/SnO_2-0.50 cathode after desorption.

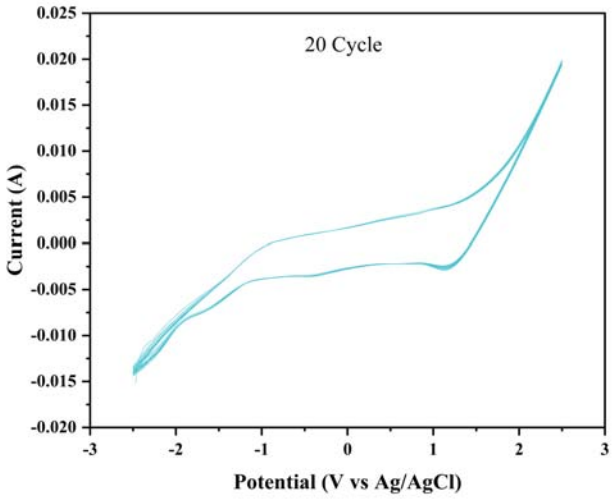


Fig. 4.15 CV curves of the electrode with 20 consecutive cycles.

4.3.4. Environment-controlled selective gallium recovery

The interfacial adsorption and electrosorption coupled recovery of gallium ions was jointly regulated by solution chemistry, electrochemical driving force and mass-transport conditions. As shown in Fig. 4.16a, under acidic conditions (pH = 1-3), hard-acid species (Ga^{3+}, $Ga(OH)^{2+}$ and $Ga(OH)_2^{+}$) formed stable inner-coordinated Ga-O bonds with the *OH and/or *O sites on the MoO_3/SnO_2-0.50, enabling rapid interfacial capture under the applied electro-field. Increasing pH enhanced surface deprotonation

of MoO_3/SnO_2-0.50, thereby exposing more available coordination sites. Considering local pH elevation induced by proton reduction, precipitation was quantified via control experiments (pH = 3.0-3.5), revealing that chemical precipitation contributed only 6.5% of gallium removal (Fig. 4.17). Notably, even at pH 9-10 where gallium exists predominantly as anionic $Ga(OH)_4^-$/Ga $(OH)_5^{2-}$and experiences electrostatic repulsion, recovery efficiencies of 80.4% and 72.8% were achieved, corresponding to capacities of 111.8 mg g^{-1} and 100.6 mg g^{-1}, respectively. Based on SEM and EDS analysis results, the contribution of gallium ions capture by the anode in the CEC system was negligible (Fig. 4.18). NO_3^- as a high-concentration supporting electrolyte suppressed the transport amount of gallium species toward the anode. Due to the strong inner-coordination adsorption formed between the MoO_3/SnO_2-0.50 and gallium ions, a sustained concentration gradient was established within the diffusion layer, rendering diffusion the dominant transport mechanism [60]. Furthermore, the solution convection from the anode toward the cathode further facilitated mass transfer, collectively enabling excellent gallium recovery performance even under alkaline conditions.

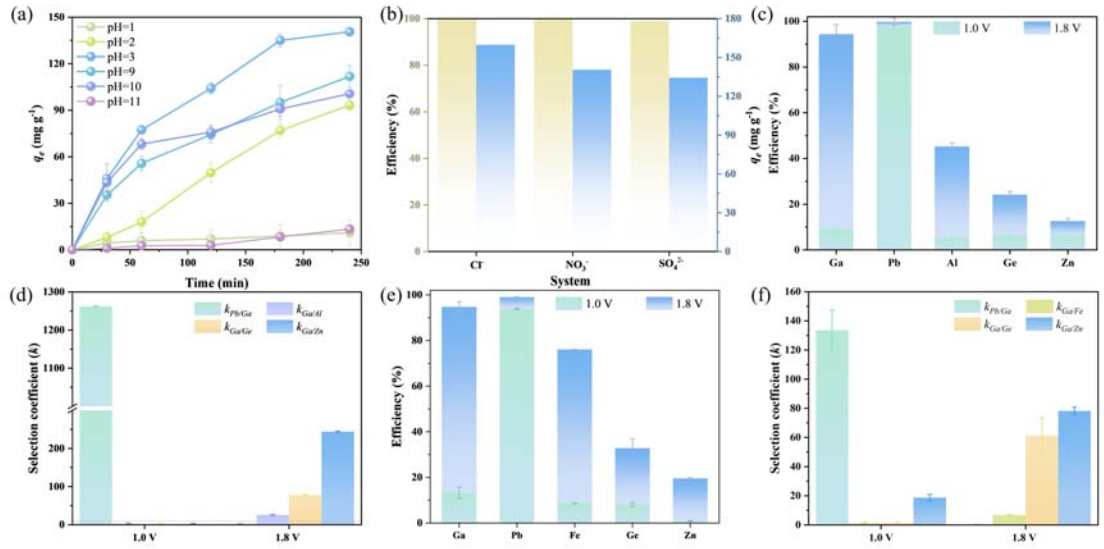


Fig. 4.16 (a) Effect of pH on the CEC process of gallium recovery (V = 100 mL, C = 50 mg L^{-1}, t = 240 min). (b) Gallium recovery performances in different electrolytic systems. Stepwise separation efficiencies in (c) the multi-metal solution and (e) the simulated zinc residue leachate, and corresponding selectivity coefficients in (d) and (f), respectively.

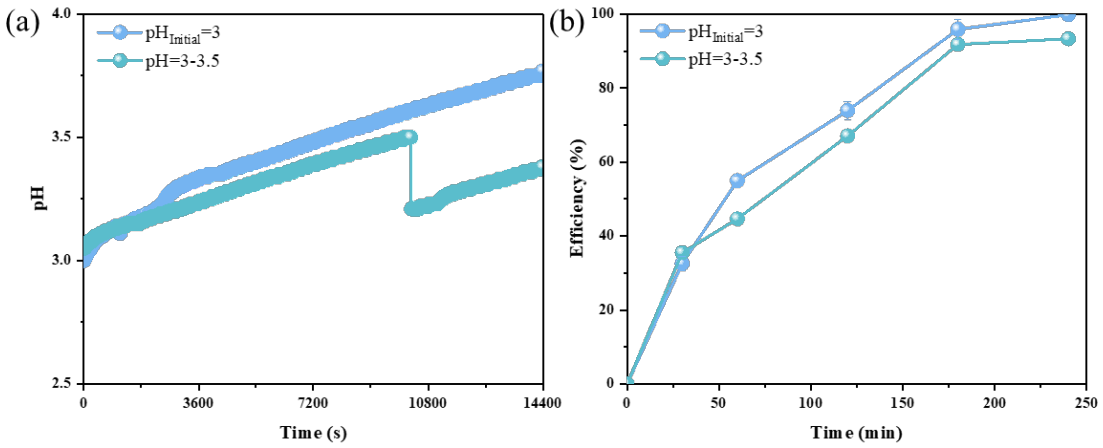


Fig. 4.17 (a) Real-time monitoring and (b) effect of pH during the gallium recovery process.

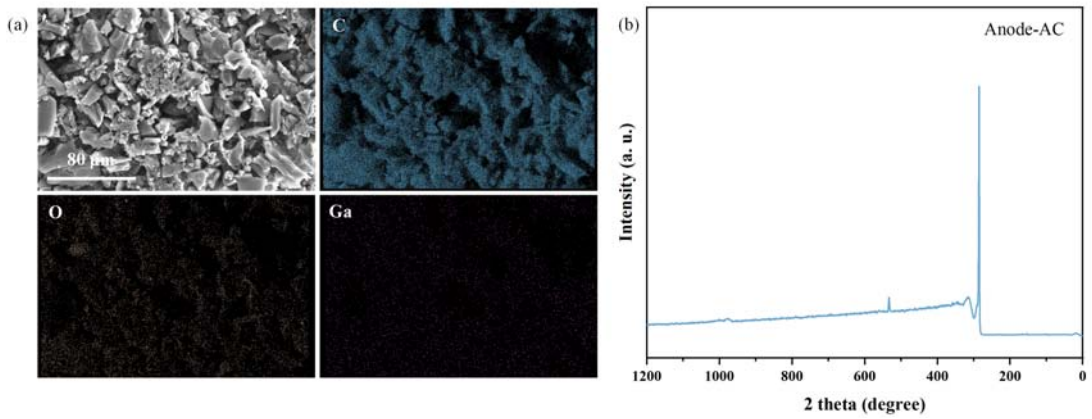


Fig. 4.18 (a) SEM image and corresponding elemental mapping, (b) XRD spectrum of the anode activated carbon after gallium recover.

The applied voltage exerted decisive control over gallium enrichment during CEC process (Fig. 4.19a). An optimal balance between capacity and current efficiency was achieved at 1.8 V. Increasing the potential to 2.2-2.6 V accelerated the migration of gallium species yet substantially intensified hydrogen evolution, reducing electron utilization and diminishing interfacial capture due to bubble shielding and site competition (Fig. 4.19b) [14]. Raising the flow rate to 7.5 mL min^{-1} simultaneously enhanced forced convection and compressed the diffusion layer, resulting in boosted interfacial flux. However, excessive flow destabilized the residence time required for coordination (Fig. 4.20).

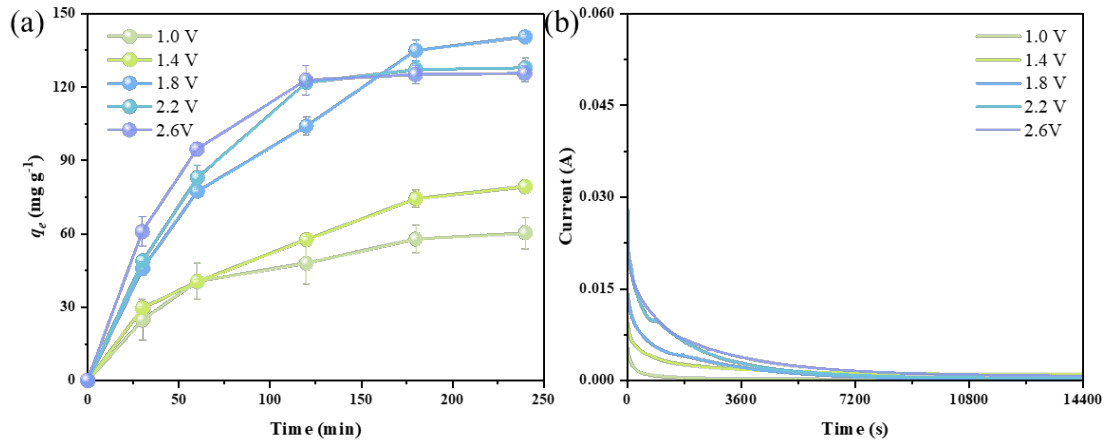


Fig. 4.19 (a) Effect of charging voltage on the CEC process of gallium recovery. (b) Chronoamperometry tests during gallium recovery under different voltage conditions.

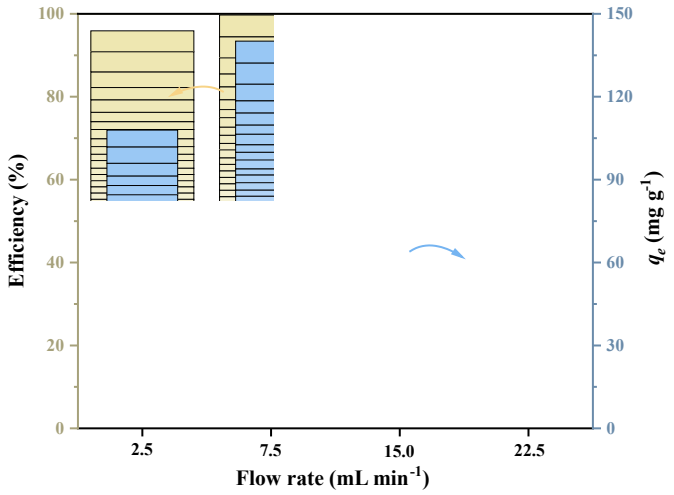


Fig. 4.20 Effect of flow rate on the CEC process.

Acid leaching mediated by chloride-, nitrate-, and sulfate-based media has emerged as a key route for gallium recovery from secondary resources [3,61–63]. To elucidate anion-dependent CEC behavior, three representative systems were systematically evaluated. CEC exhibited robust cross-system applicability, achieving highly efficient gallium enrichment (Fig. 4.16b) with performance following Cl^- > NO_3^- > SO_4^{2-}, corresponding respectively to lower de-solvation barriers, optimal interfacial stability, and intensified interfacial blocking.

The selective recovery performance of gallium ions was assessed in simulated solutions containing common competing metals (Al, Zn, Pb, and Ge). The CEC system

based on molybdenum disulfide defect electrode has been demonstrated to preferentially enrich Pb^{2+} at the relatively low potential of 1.2 V, underscoring the necessity of voltage-programmed stepwise separation [64]. Accordingly, the ions capture behavior of the multi-metal system was first examined at the low voltage of 1.0 V. Pb^{2+} was preferentially captured within 60 min with the removal efficiency of 97.8% (Fig. 4.16c), whereas the capture efficiencies for Ga^{3+}, Al^{3+}, Ge^{4+}, and Zn^{2+} were only 9.0%, 5.3%, 6.5%, and 6.0%, respectively. Elevating the applied voltage to 1.8 V significantly activated the electrical double-layer enrichment and the inner-coordination adsorption processes of gallium ions. The selectivity coefficients ($k_{Ga/Al}$ = 25.3, $k_{Ga/Ge}$ = 77.5, $k_{Ga/Zn}$ = 244.0) all exceeded the commonly used benchmark for determining good selectivity (k > 10), indicating that the enhanced electric field facilitated the interface enrichment and selective capture of gallium ions in the multi-metal solution (Fig. 4.16d).

Simulated zinc residue leachate was prepared based on the composition of zinc refinery residue from a smelter in southern China (Table 4.2) and subjected to the two-step constant-voltage method to further evaluate the low-concentration gallium recovery under interference from high-concentration competing metals [65]. The leachate was continuously pumped through the flow-through device, and the metal ion concentrations in the effluent were measured. As shown in Fig. 4.16e, the low-voltage stage was still dominated by Pb^{2+} removal, with the removal efficiency reaching 93.7% after 240 min. Gallium recovery occurred in both the 1.0 V and 1.8 V constant-voltage stages, contributing 13.3% and 81.4% of the total gallium recovery efficiency, respectively, finally reducing gallium concentration in the effluent to 0.6 mg L^{-1}. Even in the presence of relatively high concentrations of Zn^{2+} and Ge^{4+}, the low-concentration gallium ions exhibited pronounced selective capture, as reflected by the high selectivity coefficients of $k_{Ga/Zn}$ = 78.2 and $k_{Ga/Ge}$ = 61.3 (Fig. 4.16f). The effective response of gallium across a wide voltage window provides a basis for optimizing voltage programs to balance between recovery efficiency and selectivity. Notably, the Fe^{3+} concentration decreased from 207.3 mg L^{-1} to 49.7 mg L^{-1}, which may be attributed to the precipitation reaction observed during the recovery process and competitive adsorption on the electrode surface, indicating that Fe^{3+} is the primary interfering component affecting the selective recovery of gallium. Therefore, pre-removal of iron should be considered a critical treatment step for optimizing the gallium recovery process. Previous studies have shown that solvent extraction method based on Cyanex

921, Cyanex 923, P204, and N235, as well as the ultrasonic-assisted iron powder reduction precipitation, can effectively alleviate the competitive interference of Fe^{3+} while minimizing gallium loss [66–69]. Overall, voltage-programmable selectivity provided a robust strategy for on-demand sequential enrichment of target metals from polymetallic leachates. Further integration with membrane separation technology, enabled by regulating membrane surface charge and confined nanostructure, may promote the directional migration of gallium ions, thereby improving gallium separation selectivity and enrichment purity [3].

Table 4.2 Major elements in simulated zinc residue leachate

Element	Zn	Pb	Fe	Si	Ga	Ge
C (mg L^{-1})	198	139	210	-	10	15

4.3.5. Electro-assisted recovery mechanism

Using uncoated conductive graphite paper as the cathode, the recovery performance of gallium ions through electrical double-layer adsorption was investigated under constant voltage condition. As shown in Fig. 4.21a, the gallium ions recovery efficiency was only 25.9%, indicating that electron injection alone was insufficient to drive effective interfacial capture. When the voltage was not applied, the conventional adsorption process of gallium ions on the electrode exhibited slow kinetics and limited adsorption capacity. In contrast, 93.3% of gallium ions were captured in the CEC system, indicating that the electro-assisted gallium ions recovery achieved by the MoO_3/SnO_2-0.50 cathode was not a simple superposition of adsorption and electrical double-layer adsorption.

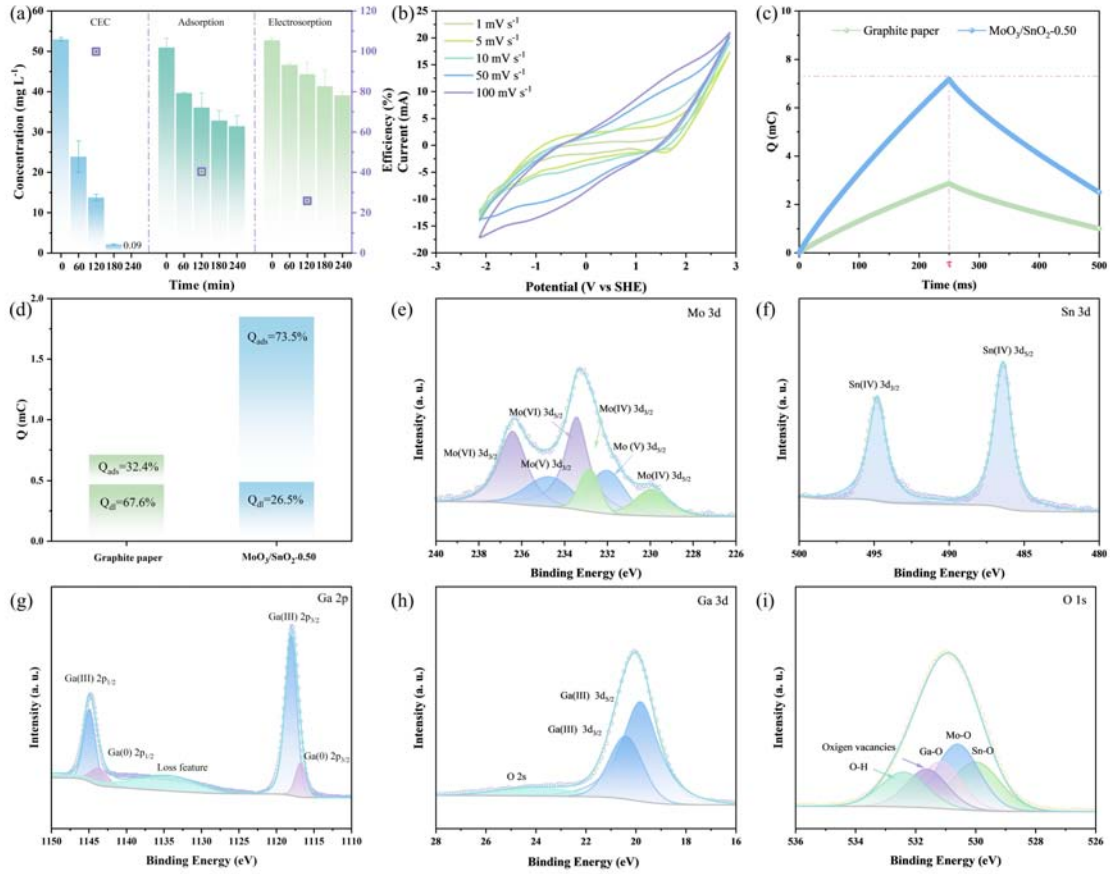


Fig. 4.21 (a) Comparison of gallium recovery performance among CEC, adsorption and electrosorption. (b) CV curves of the MoO_3/SnO_2-0.50 electrode at different scan rates. (c) The double potential step chronocoulometry curves, and (d) charge-distribution analysis distinguishing the contributions of specific adsorption and electrical double-layer capacitance for graphite paper and MoO_3/SnO_2-0.50 electrodes. High-resolution XPS spectra of (e) Mo 3d, (f) Sn 3d, (g) Ga 2p, (h) Ga 3d and (i) O 1s after the recovery of gallium.

CV curves at different scan rates (Fig. 4.21b) showed that the reduction peak shifted toward more negative potentials with increasing scan rate, and no reversible redox peaks appeared, indicating that gallium ions recovery proceeded as an irreversible process dominated by electric field-enhanced surface coordination [15]. The relationship between peak current (I_p) and scan rate (v) is appropriately described by the Randles-Sevcik equation. The linear fit of the I_p-$v^{1/2}$ relationship pointed to diffusion-controlled kinetics (Fig. 4.22). Based on the double potential step chronocoulometry method, the charge associated with specific adsorption on the MoO_3/SnO_2-0.50 cathode significantly exceeded the electrical double-layer charge and

far surpassed that of the bare graphite paper electrode (Figs. 4.21c, d and 4.23), corroborating the observed macroscopic recovery performance [70,71]. The strong interaction between the electrode and gallium ions accelerated the transfer rate of gallium ions in the electrolyte and compressed the electrical double-layer thickness, thereby achieving efficient gallium ions storage [14].

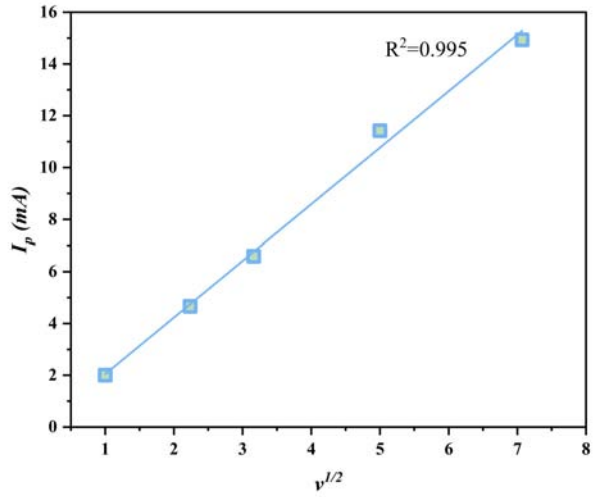


Fig. 4.22 Relationship of I_p and $v^{1/2}$ of the cathodic peak on MoO_3/SnO_2-0.50.

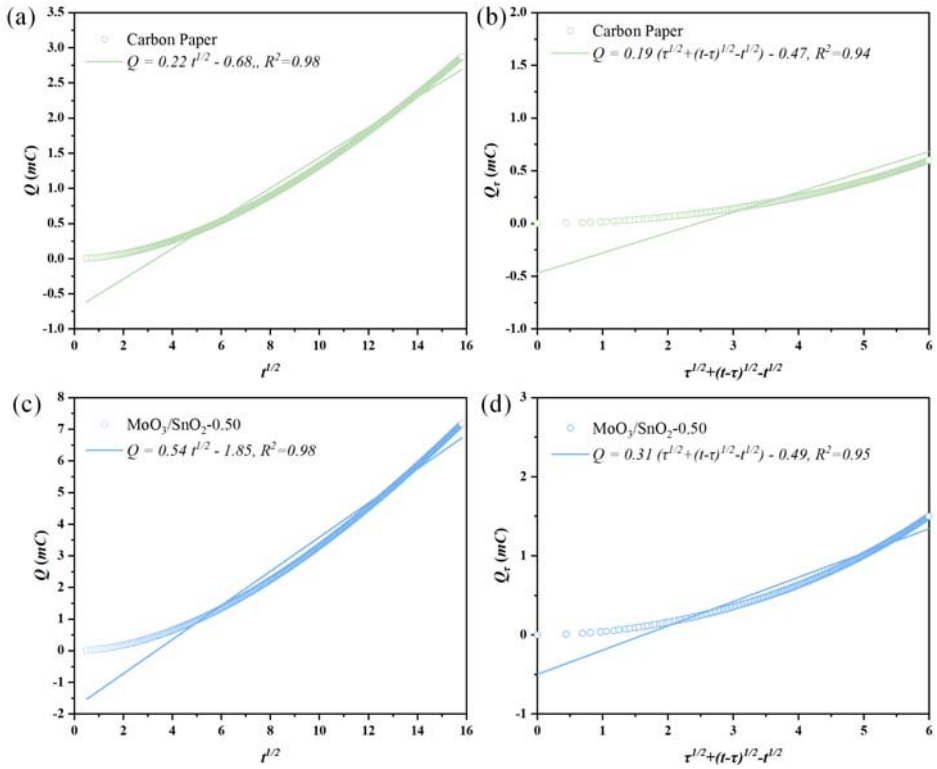


Fig. 4.23 Anson plots of the forward and reverse potential steps in (a, b) graphite

paper and (c, d) MoO_3/SnO_2-0.50.

The evolution of oxidation states and coordination environments provided direct evidence for the interfacial reaction mechanism between MoO_3/SnO_2-0.50 and gallium ions under CEC conditions. In the high-resolution Mo 3d spectrum, the deconvoluted peaks centered at 236.37 eV and 233.38 eV corresponded to $3d_{3/2}$ and $3d_{5/2}$ of Mo(VI), respectively, both exhibiting positive shifts of approximately 0.30 eV compared to the pre-recovery samples (Fig. 4.21e). The relative content of Mo(VI) increased from 29.9% to 53.0%, whereas the relative contents of Mo(V) and Mo(IV) decreased from 47.4% to 29.0% and from 22.7% to 18.0%, respectively. The systematic shift from low- to high-valence states suggested the evolution of the Mo-O local environment during gallium ions capture, characterized by reduced electron density and increasingly electropositive chemical character. The overall positive shift of Mo 3d combined with the opposite negative shift of Sn 3d represented a synergistic response, reflecting electron redistribution across the heterointerface. Notably, although SnO_2 maintained a stable valence state within the applied potential window, the Sn(IV) $3d_{3/2}$ and $3d_{5/2}$ deconvoluted peaks consistently shifted negatively by approximately 0.32 eV, leading to the increased electron density around Sn sites and enhanced surface shielding effect (Fig. 4.21f). Together with previous reports that SnO_2 possessed the high overpotential and weak H^+ adsorption affinity for hydrogen evolution reaction [27,28,72], the electronic environment evolution in MoO_3/SnO_2-0.50 further validated our strategy of suppressing hydrogen evolution to promote efficient gallium ions recovery.

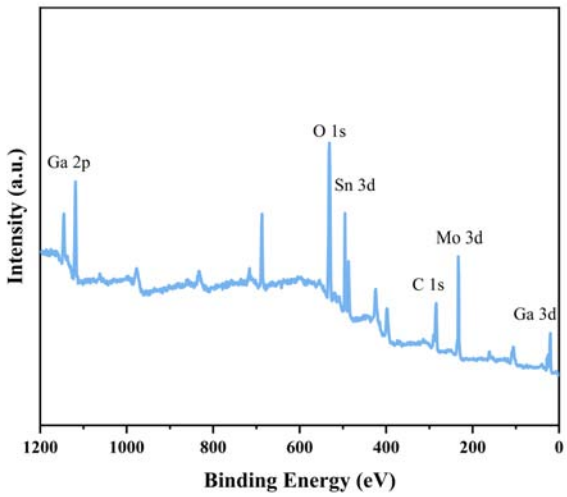


Fig. 4.24 XPS spectrum of MoO_3/SnO_2-0.50 after recovery.

In the XPS spectra after gallium ions loading (Fig. 4.24), Ga $2p_{1/2}$, Ga $2p_{3/2}$, and Ga 3d peaks appeared at 1145.08 eV, 1118.18 eV, and 20.08 eV, respectively. For the high-resolution Ga 2p and 3d spectra, gallium predominantly existed as Ga(III), with strong Ga(III) $2p_{1/2}$, $2p_{3/2}$ and $3d_{5/2}$, $3d_{3/2}$ deconvoluted peaks and negligible metallic signals, demonstrating that gallium ions capture primarily occurred via inner-layer coordination rather than metallic deposition (Figs. 4.21g and h). As shown in Fig. 4.21i and Table 4.3, the emergence of a pronounced Ga-O signal (531.17 eV, 18.2%), together with the attenuation and positive shifts of Sn-O (529.99 eV), Mo-O (530.59 eV) and -OH (532.42 eV) in the high-resolution O 1s spectrum after gallium recovery, further indicated the interfacial complexation of gallium with surface oxygen sites on MoO_3/SnO_2-0.50, likely forming Ga-O-Mo and Ga-O-Sn bridging structures [19,23,24,30,36,73,74]. Similar complexation mechanisms were present in the adsorption of Ag^+ by MoO_x (forming Mo-O-Ag) and UO_2^{2+} by $LiFePO_4$ (forming Fe-O-U) [23,75]. The decreased relative content of oxygen vacancies at the heterointerface implied the establishment of the interfacial microenvironment favorable for gallium ions capture. The centers of oxygen vacancies are known to accumulate positive charge, while adjacent regions host compensating negative charge, giving rise to a locally oriented dipole field [31]. The synergistic interaction between the built-in electric field and the applied electric field impelled the migration and enrichment of positively charged gallium species, including Ga^{3+}, $Ga(OH)^{2+}$ and $Ga(OH)_2^+$, toward defect-rich regions, achieving efficient immobilization through the combined effects of electrostatic adsorption and coordination interactions.

Table 4.3 Binding energies and relative contents of the components in the high-resolution O 1s XPS spectra after recovery

O1s	Binding energy	Relative content	
	(eV)	Before	After
Sn-O	529.99	23.8%	22.9%
Mo-O	530.59	36.4%	27.9%
Ga-O	531.17	-	18.2%
Oxygen vacancy	531.62	16.8%	15.4%
-OH	532.42	23.0%	15.6%

Overall, the bimetallic oxide interface acted as the core foundation for gallium ions separation, owing to its tunable chemical structure and electronic properties. The enhanced electrical double-layer capacitance and oxygen-coordination interactions were crucial for the recovery of low-concentration gallium ions. The synergistic interaction between electrochemical processes and coordination chemistry will expand the application boundaries of resource recovery in complex systems (Fig. 4.25). Flexible potential regulation enables targeted applications, including potential inversion, potential window compression, and multistage potential separation. Strong coordination bonds significantly enhance the recovery rate and efficiency of metal ions while potentially lowering the reduction potential, making the stability constant a key indicator for screening electroactive ligands [16]. The mechanism confers CEC technology with unique advantages in treating hard-to-reduce metals such as gallium, rare earth elements, nickel, magnesium, tungsten, lead and arsenic. Interfacial capture can be achieved directly in low-concentration leachate without additional enrichment steps. For more reactive metals like copper, gold, silver, and platinum group metals, direct conversion to elemental metals occurs at mild potentials, substantially simplifying conventional hydrometallurgical processes and reducing chemical reagent consumption and environmental burden.

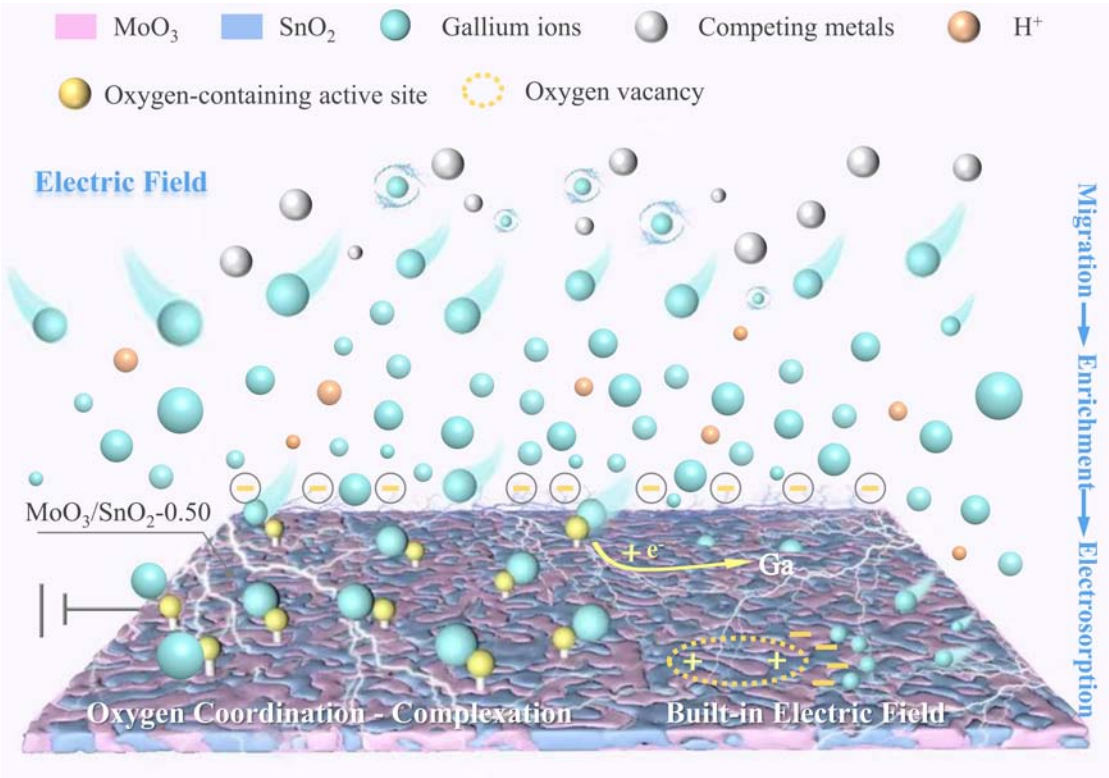


Fig. 4.25 Schematic illustration of the electro-assisted gallium capture mechanism at the MoO_3/SnO_2-0.50 heterointerface.

4.4. Conclusions

The electrochemical strategy based on bimetallic oxide electrode design was proposed to suppress hydrogen evolution reaction while recovering gallium ions over the broad concentration range (0.5-200.0 mg L^{-1}). Compared to conventional adsorption and electrical double-layer adsorption, the CEC system exhibited outstanding electro-assisted gallium ions recovery efficiencies (81.7%-99.8%) and capacities (1.5-486.3 mg g^{-1}), applicable in Cl^-, NO_3^-, SO_4^{2-} systems. The applied electric field promoted ion migration by weakening the hydration energy barrier of gallium species. Efficient storage was primarily attributed to oxygen coordination formed between MoO_3/SnO_2-0.50 and gallium ions. Voltage-programmed stepwise separation provided a feasible strategy for selective gallium uptake in multicomponent systems. And the MoO_3/SnO_2-0.50 electrode demonstrated excellent electrochemical stability and cycling durability. Therefore, this study induced electrons to preferentially participate in the interfacial complexation or reduction of target ions through interfacial electron regulation and asymmetric electrochemical configurations, providing insights into the design of CEC electrodes and the efficient recovery of critical metals from aqueous solutions.

4.5. References

[1] A.N. Løvik, E. Restrepo, D.B. Müller, Byproduct Metal Availability Constrained by Dynamics of Carrier Metal Cycle: The Gallium-Aluminum Example, Environ. Sci. Technol. 50 (2016) 8453–8461. https://doi.org/10.1021/acs.est.6b02396.

[2] F. Lu, T. Xiao, J. Lin, Z. Ning, Q. Long, L. Xiao, F. Huang, W. Wang, Q. Xiao, X. Lan, H. Chen, Resources and extraction of gallium: A review, Hydrometallurgy 174 (2017) 105–115. https://doi.org/10.1016/j.hydromet.2017.10.010.

[3] X. Zhang, Z. Zhang, J. Fu, G. Zhou, G. Li, Y. Cao, G. Fan, P. Li, D. Teng, Toward circular Gallium: Recovery pathways from Bayer Liquor, red Mud, fly Ash, and e-waste, Waste Manag. 218 (2026) 115543. https://doi.org/10.1016/j.wasman.2026.115543.

[4] S. Dhiman, N. Fuloria, A. Ghosh, S. Chaudhary, S. Ziauddin Ahammad, S. Tsushima, N. Kelly, R. Jain, Gallium recovery from red mud: Integration of solvent extraction and siderophore assisted technologies, J. Environ. Manage. 370 (2024)

122374. https://doi.org/10.1016/j.jenvman.2024.122374.

[5] R. Jain, S. Fan, P. Kaden, S. Tsushima, H. Foerstendorf, R. Barthen, F. Lehmann, K. Pollmann, Recovery of gallium from wafer fabrication industry wastewaters by Desferrioxamine B and E using reversed-phase chromatography approach, Water Res. 158 (2019) 203–212. https://doi.org/10.1016/j.watres.2019.04.005.

[6] R.M. DuChanois, N.J. Cooper, B. Lee, S.K. Patel, L. Mazurowski, T.E. Graedel, M. Elimelech, Prospects of metal recovery from wastewater and brine, Nat. Water 1 (2023) 37–46. https://doi.org/10.1038/s44221-022-00006-z.

[7] C. Li, G. Li, F. Qiu, Z. Miao, G. Zhou, M. Qiu, W. Kou, Q. He, J. Zhu, J. Wang, W. Li, Amine-Appended 3D metal organic framework with tailored Energy-Matching effect for breakthrough gallium capture, Sep. Purif. Technol. 378 (2025) 134821. https://doi.org/10.1016/j.seppur.2025.134821.

[8] Y. Liu, Z. Xin, L. Tian, D. Villa-Gomez, W. Wang, Y. Cao, Fabrication of peptide-encapsulated sodium alginate hydrogel for selective gallium adsorption, Int. J. Biol. Macromol. 263 (2024) 130436. https://doi.org/10.1016/j.ijbiomac.2024.130436.

[9] Z. Lv, M. Ma, Y. Huang, W. Wang, G. Li, L. Si, G. Fan, Y. Cao, P. Li, D. Teng, Hydroxamic acid-functionalized chitosan hydrogel beads for sustainable and continuous gallium recovery, Int. J. Biol. Macromol. 322 (2025) 146869. https://doi.org/10.1016/j.ijbiomac.2025.146869.

[10] E. Díez, J.M. Gómez, A. Rodríguez, I. Bernabé, J. Galán, Recovery of Gallium from Aqueous Solution through Preconcentration by Adsorption/Desorption on Disordered Mesoporous Carbon, J. Sustain. Metall. 7 (2021) 227–242. https://doi.org/10.1007/s40831-021-00336-4.

[11] H. Zhu, J. Li, H. Zhang, Z. Wang, N. Wang, C. Wang, F. Jia, S. Song, Coordination-mediated interfacial enrichment for efficient extraction of ultra-dilute rare earth ions via high-density affinity sites electrode, Chem. Eng. J. 521 (2025) 166678. https://doi.org/10.1016/j.cej.2025.166678.

[12] P. Li, Y. Gui, D.J. Blackwood, Development of a Nanostructured α-MnO_2/Carbon Paper Composite for Removal of Ni^{2+}/Mn^{2+} Ions by Electrosorption, ACS Appl. Mater. Interfaces 10 (2018) 19615–19625. https://doi.org/10.1021/acsami.8b02471.

[13] W. Zhan, X. Zhang, Y. Yuan, Q. Weng, S. Song, M. de J. Martínez-López, J.L. Arauz-Lara, F. Jia, Regulating Chemisorption and Electrosorption Activity for Efficient Uptake of Rare Earth Elements in Low Concentration on Oxygen-Doped Molybdenum Disulfide, ACS Nano 18 (2024) 7298–7310. https://doi.org/10.1021/acsnano.4c00691.

[14] W. Zhan, Y. Yuan, Q. Weng, Y. Pan, S. Song, J.L. Arauz-Lara, F. Jia, W. Zhang, Enhanced trace gadolinium(III) extraction via tailored chemisorption on defect-engineered molybdenum disulfide electrodes, Chem. Eng. J. 512 (2025) 162632. https://doi.org/10.1016/j.cej.2025.162632.

[15] D. Wang, Y. Liang, Y. Zeng, C. Liu, C. Zhan, P. Chen, S. Song, F. Jia, Highly selective recovery of gold and silver from E-waste via stepwise electrodeposition directly from the pregnant leaching solution enabled by the MoS2 cathode, J. Hazard. Mater. 465 (2024) 133430. https://doi.org/10.1016/j.jhazmat.2024.133430.

[16] Q. Song, L. Zhang, C. Yang, Z. Xu, Novel Electrodeposition Method for Cu-In-Cd-Ga Sequential Separation from Waste Solar Cell: Mechanism, Application, and Environmental Impact Assessment, Environ. Sci. Technol. 55 (2021) 10724–10733. https://doi.org/10.1021/acs.est.1c02496.

[17] S. Trasatti, Work function, electronegativity, and electrochemical behaviour of metals. III. Electrolytic hydrogen evolution in acid solutions, J. Electroanal. Chem. 39 (1972) 163–184. https://doi.org/10.1016/S0022-0728(72)80485-6.

[18] X. Su, K.J. Tan, J. Elbert, C. Rüttiger, M. Gallei, T.F. Jamison, T.A. Hatton, Asymmetric Faradaic systems for selective electrochemical separations, Energy Environ. Sci. 10 (2017) 1272–1283. https://doi.org/10.1039/c7ee00066a.

[19] J. Fan, L. Gao, S. Li, N. Chai, D. Lei, Efficient recovery of gallium(III) from alkaline solution by electrosorption using biomass-derived carbon aerogel electrodes, Sep. Purif. Technol. 353 (2025) 128297. https://doi.org/10.1016/j.seppur.2024.128297.

[20] S.R. Cotty, N. Kim, X. Su, Electrochemically Mediated Recovery and Purification of Gold for Sustainable Mining and Electronic Waste Recycling, ACS Sustain. Chem. Eng. 11 (2023) 3975–3986. https://doi.org/10.1021/acssuschemeng.3c00227.

[21] L. Yu, G.Z. Chen, Redox electrode materials for supercapatteries, J. Power Sources 326 (2016) 604–612. https://doi.org/10.1016/j.jpowsour.2016.04.095.

[22] I.A. de Castro, R.S. Datta, J.Z. Ou, A. Castellanos-Gomez, S. Sriram, T. Daeneke, K. Kalantar-zadeh, Molybdenum Oxides – From Fundamentals to Functionality, Adv. Mater. 29 (2017) 1701619. https://doi.org/10.1002/adma.201701619.

[23] P. Shao, Z. Chang, M. Li, X. Lu, W. Jiang, K. Zhang, X. Luo, L. Yang, Mixed-valence molybdenum oxide as a recyclable sorbent for silver removal and recovery from wastewater, Nat. Commun. 14 (2023) 1362. https://doi.org/10.1038/s41467-023-37143-2.

[24] N. Wang, J. Li, F. Jia, H. Zhou, Y. Xie, P. Chen, S. Song, M. Quintana, Unraveling

nitrogen-doped and vacancy-engineered synergistically modified molybdenum oxide promoting gallium selective adsorption, Sep. Purif. Technol. 358 (2025) 130158. https://doi.org/10.1016/j.seppur.2024.130158.

[25] W. Huang, H. Wang, R. Hu, J. Liu, L. Yang, M. Zhu, Combining Structural Modification and Electrolyte Regulation to Enable Long-Term Cyclic Stability of MoO_{3-x}@TiO_2 as Cathode for Aqueous Zn-Ion Batteries, Small 19 (2023) 2303286. https://doi.org/10.1002/smll.202303286.

[26] W. Hua, H.H. Sun, F. Xu, J.G. Wang, A review and perspective on molybdenum-based electrocatalysts for hydrogen evolution reaction, Rare Met. 39 (2020) 335–351. https://doi.org/10.1007/s12598-020-01384-7.

[27] T. Dou, J. He, S. Diao, Y. Wang, X. Zhao, F. Zhang, X. Lei, Dynamic reconstructuring of CuS/SnO_2-S for promoting CO_2 electroreduction to formate, J. Energy Chem. 82 (2023) 497–506. https://doi.org/10.1016/j.jechem.2023.03.016.

[28] L. Fan, Z. Xia, M. Xu, Y. Lu, Z. Li, 1D SnO_2 with Wire-in-Tube Architectures for Highly Selective Electrochemical Reduction of CO_2 to C1 Products, Adv. Funct. Mater. 28 (2018) 1706289. https://doi.org/10.1002/adfm.201706289.

[29] G.C. Assis, I.M.A. Silva, T. V. Dos Santos, M.R. Meneghetti, S.M.P. Meneghetti, Photocatalytic properties of SnO_2/MoO_3 mixed oxides and their relation to the electronic properties and surface acidity, J. Photochem. Photobiol. A Chem. 407 (2021) 113035. https://doi.org/10.1016/j.jphotochem.2020.113035.

[30] T. Zhao, P. Qiu, Y. Fan, J. Yang, W. Jiang, L. Wang, Y. Deng, W. Luo, Hierarchical Branched Mesoporous TiO_2–SnO_2 Nanocomposites with Well-Defined n–n Heterojunctions for Highly Efficient Ethanol Sensing, Adv. Sci. 6 (2019) 1902008. https://doi.org/10.1002/advs.201902008.

[31] C. Hou, W. Yang, H. Kimura, X. Xie, X. Zhang, X. Sun, Z. Yu, X. Yang, Y. Zhang, B. Wang, B. Bin Xu, D. Sridhar, H. Algadi, Z. Guo, W. Du, Boosted lithium storage performance by local build-in electric field derived by oxygen vacancies in 3D holey N-doped carbon structure decorated with molybdenum dioxide, J. Mater. Sci. Technol. 142 (2023) 185–195. https://doi.org/10.1016/j.jmst.2022.10.007.

[32] Y. Bao, J. Hao, S. Zhang, D. Zhu, F. Li, Structural/Compositional-Tailoring of Nickel Hexacyanoferrate Electrodes for Highly Efficient Capacitive Deionization, Small 19 (2023) 2300384. https://doi.org/10.1002/smll.202300384.

[33] S.A.K. Leghari, S. Sajjad, F. Chen, J. Zhang, WO_3/TiO_2 composite with morphology change via hydrothermal template-free route as an efficient visible light

photocatalyst, Chem. Eng. J. 166 (2011) 906–915. https://doi.org/10.1016/j.cej.2010.11.065.

[34] C. Wu, H. Xie, D. Li, D. Liu, S. Ding, S. Tao, H. Chen, Q. Liu, S. Chen, W. Chu, B. Zhang, L. Song, Atomically Intercalating Tin Ions into the Interlayer of Molybdenum Oxide Nanobelt toward Long-Cycling Lithium Battery, J. Phys. Chem. Lett. 9 (2018) 817–824. https://doi.org/10.1021/acs.jpclett.7b03374.

[35] A. Kahn, Fermi level, work function and vacuum level, Mater. Horizons 3 (2016) 7–10. https://doi.org/10.1039/c5mh00160a.

[36] J.C. Liu, H. Li, M. Batmunkh, X. Xiao, Y. Sun, Q. Zhao, X. Liu, Z.H. Huang, T.Y. Ma, Structural engineering to maintain the superior capacitance of molybdenum oxides at ultrahigh mass loadings, J. Mater. Chem. A 7 (2019) 23941–23948. https://doi.org/10.1039/c9ta04835a.

[37] J. Xu, C. Zhang, H. Liu, J. Sun, R. Xie, Y. Qiu, F. Lü, Y. Liu, L. Zhuo, X. Liu, J. Luo, Amorphous MoO_x-Stabilized single platinum atoms with ultrahigh mass activity for acidic hydrogen evolution, Nano Energy 70 (2020) 104529. https://doi.org/10.1016/j.nanoen.2020.104529.

[38] J. Su, K. Shi, B. Liu, Z. Xi, J. Yu, X. Xu, P. Jing, R. Gao, J. Zhang, Engineering the Metal-Support Interaction and Oxygen Vacancies on Ru@P-Fe/Fe_3O_4 Nanorods for Synergetic Enhanced Electrocatalytic Nitrate-to-Ammonia Conversion, Adv. Funct. Mater. 34 (2024) 2401194. https://doi.org/10.1002/adfm.202401194.

[39] L. Wang, W. Huang, W. Guo, Z.H. Guo, C. Chang, L. Gao, X. Pu, Sn Alloying to Inhibit Hydrogen Evolution of Zn Metal Anode in Rechargeable Aqueous Batteries, Adv. Funct. Mater. 32 (2022) 2108533. https://doi.org/10.1002/adfm.202108533.

[40] F. Chen, Z. Wu, S. Gupta, D.J. Rivera, S. V Lambeets, S. Pecaut, J. Yoon, T. Kim, P. Zhu, Y.Z. Finfrock, M. Meira, G. King, G. Gao, W. Xu, D.A. Cullen, H. Zhou, Efficient conversion of low-concentration nitrate sources into ammonia on Ru dispersed Cu nanowire electrocatalyst, Nat. Nanotechnol. 17 (2022) 759–767. https://doi.org/https://doi.org/10.1038/s41565-022-01121-4.

[41] L. Zhang, J. Yan, S. Kang, Z. Wang, Y. Miao, R. Gao, T. Zhang, H.J. Ojeda-Galván, M. Quintana, H. Bai, S. Song, Y. Zhao, Tailoring Multiple Functional Domains of Lithium-Ion Sieves for Sustainable Lithium Extraction from Low-Quality Brines, ACS Nano 19 (2025) 33620–33631. https://doi.org/10.1021/acsnano.5c11936.

[42] Y. Mizuno, M. Okubo, D. Asakura, T. Saito, E. Hosono, Y. Saito, K. Oh-Ishi, T. Kudo, H. Zhou, Impedance spectroscopic study on interfacial ion transfers in cyanide-

bridged coordination polymer electrode with organic electrolyte, Electrochim. Acta 63 (2012) 139–145. https://doi.org/10.1016/j.electacta.2011.12.068.

[43] N. Chai, L. Gao, S. Li, Y. Cao, Z. Ma, L. Li, M. Hu, In-suit ion-imprinted bio-sorbent with superior adsorption performance for gallium(III) capture, J. Clean. Prod. 387 (2023) 135861. https://doi.org/10.1016/j.jclepro.2023.135861.

[44] L. Zhang, J. Yan, Z. Wang, T. Zhang, S. Song, M. Quintana, Y. Zhao, Solar-Driven Direct Lithium Extraction from Low-Quality Brines, Adv. Mater. 38 (2026) 12998. https://doi.org/10.1002/adma.202512998.

[45] W. Tang, J. Liang, D. He, J. Gong, L. Tang, Z. Liu, D. Wang, G. Zeng, Various cell architectures of capacitive deionization: Recent advances and future trends, Water Res. 150 (2019) 225–251. https://doi.org/10.1016/j.watres.2018.11.064.

[46] Q. Yao, H.L. Tang, Occurrence of re-adsorption in desorption cycles of capacitive deionization, J. Ind. Eng. Chem. 34 (2016) 180–185. https://doi.org/10.1016/j.jiec.2015.11.004.

[47] Y. Salamat, C.H. Hidrovo, A parametric study of multiscale transport phenomena and performance characteristics of capacitive deionization systems, Desalination 438 (2018) 24–36. https://doi.org/10.1016/j.desal.2018.03.022.

[48] W. Guo, J. Zhang, F. Yang, F. Tan, Z. Zhao, Highly efficient and selective recovery of gallium achieved on an amide-functionalized cellulose, Sep. Purif. Technol. 237 (2020) 116355. https://doi.org/10.1016/j.seppur.2019.116355.

[49] W. Wang, X. Xu, D. Lai, Q. Xu, J. Li, Y. Wang, Selective isolation of gallium and indium from waste photovoltaic modules facilitated by extractant-mesoporous activated carbon composites, Sep. Purif. Technol. 330 (2024) 125510. https://doi.org/10.1016/j.seppur.2023.125510.

[50] P. Raj, M. Patel, A.K. Karamalidis, Chemically modified polymeric resins with catechol derivatives for adsorption, separation and recovery of gallium from acidic solutions, J. Environ. Chem. Eng. 11 (2023) 110790. https://doi.org/10.1016/j.jece.2023.110790.

[51] J. Ni, X. Zhu, Y. Yuan, Z. Wang, Y. Li, L. Ma, A. Dai, M. Li, T. Wu, R. Shahbazian-Yassar, J. Lu, L. Li, Rooting binder-free tin nanoarrays into copper substrate via tin-copper alloying for robust energy storage, Nat. Commun. 11 (2020) 1212. https://doi.org/10.1038/s41467-020-15045-x.

[52] W. Wang, S. Liu, Y. Zhou, J. Luo, J. Shi, Z. Zhou, J. Ma, Extraction of Sr^{2+} from aqueous solutions using an asymmetric pulsed current-assisted electrochemical method,

Sep. Purif. Technol. 276 (2021). https://doi.org/10.1016/j.seppur.2021.119235.

[53]S. Wang, G. Lv, T. Zhang, Preparation of a gallium-imprinted resin-capacitive deionization electrode and study of its gallium adsorption performance, New J. Chem. 48 (2024) 17878–17885. https://doi.org/10.1039/d4nj03271c.

[54]Z. Qin, S. Wang, S. Zhang, J. Xie, C. an Zhou, C. Wang, L. Song, K. Ma, D. Luo, H. Yue, Cross-linked amidoxime porous resin for selective gallium separation in Bayer solutions: Reaction mechanism and kinetic study, Chem. Eng. J. 481 (2024). https://doi.org/10.1016/j.cej.2023.148340.

[55]Y. Zhang, X. Liu, Y. Wang, Z. Lou, W. Shan, Y. Xiong, Polyacrylic acid-functionalized graphene oxide for high-performance adsorption of gallium from aqueous solution, J. Colloid Interface Sci. 556 (2019) 102–110. https://doi.org/10.1016/j.jcis.2019.08.032.

[56]Y. Wang, L. Zhu, Y. Song, Z. Lou, W. Shan, Y. Xiong, Novel chitosan-based ions imprinted bio-adsorbent for enhanced adsorption of gallium(III) in acidic solution, J. Mol. Liq. 320 (2020) 114413. https://doi.org/10.1016/j.molliq.2020.114413.

[57]L. Gao, L. Wang, Y. Cao, S. Li, Persimmon peel-based ion-imprinted adsorbent with enhanced adsorption performance of gallium ions, Miner. Eng. 176 (2022) 107354. https://doi.org/10.1016/j.mineng.2021.107354.

[58]C. Shi, K. Wang, C. Chen, Y. Cao, G. Zhou, J. Wang, C. Li, Highly selective capture of gallium from aqueous solutions using tetradentate amidoxime functionalized MIL-53(Al) nanofiber membranes, Sep. Purif. Technol. 330 (2024). https://doi.org/10.1016/j.seppur.2023.125303.

[59]S. Lu, L. Chen, M.F. Hamza, C. He, X. Wang, Y. Wei, E. Guibal, Amidoxime functionalization of a poly(acrylonitrile)/silica composite for the sorption of Ga(III) – Application to the treatment of Bayer liquor, Chem. Eng. J. 368 (2019) 459–473. https://doi.org/10.1016/j.cej.2019.02.094.

[60]S. Gladyshev, A. Akcil, R. Abdulvaliev, Y. Tastanov, K. Beisembekova, S. Temirova, Kinetic study of gallium electrochemical reduction in alkaline solution, Hydrometallurgy 140 (2013) 95–101. https://doi.org/10.1016/j.hydromet.2013.08.012.

[61]D. Hu, B. Ma, X. Li, Y. Lv, Y. Chen, C. Wang, Innovative and sustainable separation and recovery of valuable metals in spent CIGS materials, J. Clean. Prod. 350 (2022). https://doi.org/10.1016/j.jclepro.2022.131426.

[62]K. Zheng, M.F. Benedetti, R. Jain, K. Pollmann, E.D. van Hullebusch, Recovery of gallium (and indium) from spent LEDs: Strong acids leaching versus selective

leaching by siderophore desferrioxamine E, Sep. Purif. Technol. 338 (2024). https://doi.org/10.1016/j.seppur.2024.126566.

[63] S. Bao, Q. Huang, B. Chen, Y. Jiang, Hydrometallurgical recovery of gallium from gallium-containing secondary resources: Leaching, separation and purification, Sep. Purif. Technol. 376 (2025). https://doi.org/10.1016/j.seppur.2025.134068.

[64] W. Zhan, Y. Yuan, X. Zhang, Y. Liang, S. Song, M. de Jesús Martínez-López, J.L. Arauz-Lara, F. Jia, Efficient and selective Lead(II) removal within a wide concentration range through chemisorption and electrosorption coupling process via defective MoS2 electrode, Sep. Purif. Technol. 329 (2024). https://doi.org/10.1016/j.seppur.2023.125183.

[65] S. Rao, D. Wang, Z. Liu, K. Zhang, H. Cao, J. Tao, Selective extraction of zinc, gallium, and germanium from zinc refinery residue using two stage acid and alkaline leaching, Hydrometallurgy 183 (2019) 38–44. https://doi.org/10.1016/j.hydromet.2018.11.007.

[66] R.K. Mishra, P.C. Rout, K. Sarangi, K.C. Nathsarma, A comparative study on extraction of Fe(III) from chloride leach liquor using TBP, Cyanex 921 and Cyanex 923, Hydrometallurgy 104 (2010) 298–303. https://doi.org/10.1016/j.hydromet.2010.07.003.

[67] K.Y. Macías-Macías, A.E. Ceniceros-Gómez, M.E. Gutiérrez-Ruiz, J.L. González-Chávez, L.G. Martínez-Jardines, Extraction and recovery of the strategic element gallium from an iron mine tailing, J. Environ. Chem. Eng. 7 (2019) 102964. https://doi.org/10.1016/j.jece.2019.102964.

[68] X. Sun, Y. Sun, J. Yu, Removal of ferric ions from aluminum solutions by solvent extraction, part I: Iron removal, Sep. Purif. Technol. 159 (2016) 18–22. https://doi.org/10.1016/j.seppur.2015.12.054.

[69] F. Liu, Z. Liu, Y. Li, B.P. Wilson, M. Lundström, Recovery and separation of gallium(III) and germanium(IV) from zinc refinery residues: Part I: Leaching and iron(III) removal, Hydrometallurgy 169 (2017) 564–570. https://doi.org/10.1016/j.hydromet.2017.03.006.

[70] A. Kousar, T. Laurila, Insights into electrode-electrolyte adsorption dynamics via double potential step chronocoulometry and cyclic voltammetry, J. Electroanal. Chem. 965 (2024). https://doi.org/10.1016/j.jelechem.2024.118374.

[71] Q. Zheng, H. Shao, Correlation between redox species adsorption and electron transfer kinetics of mildly oxidized graphene: A chronocoulometry and SECM study,

Electrochem. Commun. 103 (2019) 83–87. https://doi.org/10.1016/j.elecom.2019.05.014.

[72] J. Zhang, G. Chen, Q. Liu, C. Fan, D. Sun, Y. Tang, H. Sun, X. Feng, Competitive Adsorption: Reducing the Poisoning Effect of Adsorbed Hydroxyl on Ru Single-Atom Site with SnO_2 for Efficient Hydrogen Evolution, Angew. Chemie - Int. Ed. 61 (2022). https://doi.org/10.1002/anie.202209486.

[73] P. Gao, Q. Ru, Z. Pan, J. Zhang, W. Xu, F. Chi-Chung Ling, L. Wei, Robust hetero-MoO_3/MoO_2@N-doped carbon nanobelts decorated with oxygen deficiencies as high-performance anodes for potassium/sodium storage, J. Colloid Interface Sci. 599 (2021) 730–740. https://doi.org/10.1016/j.jcis.2021.04.110.

[74] Y. Li, S.M. Shaheen, M. Azeem, L. Zhang, C. Feng, J. Peng, W. Qi, J. Liu, Y. Luo, Y. Peng, E.F. Ali, K. Smith, J. Rinklebe, Z. Zhang, R. Li, Removal of lead (Pb^{+2}) from contaminated water using a novel MoO_3-biochar composite: Performance and mechanism, Environ. Pollut. 308 (2022) 119693. https://doi.org/10.1016/j.envpol.2022.119693.

[75] S. Chen, X. Wang, H. Zheng, Z. Wang, X. Wang, Z. Lin, S. Feng, C. Zhang, T. Sun, J. Zhu, Electron-buffering rechargeable microelectrode adsorbents for rapid environmental remediation of uranium-containing wastewater, Nat. Water 3 (2025) 937–948. https://doi.org/10.1038/s44221-025-00471-2.

Chapter 5. Conclusions

Global energy transition is driving exponentially growing critical metals demand, particularly gallium, indium, PGMs. Efficient recognition and recovery of critical metal from aqueous resources are critical for environmental remediation and resource sustainability. This work aims to address the challenges of mass transfer limitations, insufficient selectivity, and low recovery efficiency of critical metals in diluted complex aqueous solutions. A series of functional adsorbents and electrode materials were developed through heteroatom doping, defect engineering, heterointerface construction, and cationic porous-interface design. The separation and recovery behaviors were systematically investigated through adsorption, electrosorption, and direct electrochemical reduction. The main conclusions are summarized as follows:

1. Nitrogen doping coupled with defect engineering was employed to construct α-MoO_x/N nanowire adsorbents for high-capacity and highly selective gallium adsorption. Under acidic conditions, the optimized α-MoO_x/N achieved a gallium adsorption efficiency of 98.9% within 60 min and a maximum adsorption capacity of 464.8 mg g^{-1}. The enhanced performance originated from the combined contributions of electrostatic interactions, H^+ exchange, and surface coordination involving Mo-O and nitrogen-containing sites, with oxygen vacancies providing additional high-affinity binding sites for gallium. The adsorbent retained excellent gallium selectivity in the presence of competing ions, including Zn^{2+}, Al^{3+}, Cu^{2+}, and Ni^{2+}, with a maximum $k_{Ga/Zn}$ of 1951. After five consecutive cycles, the gallium capture efficiency remained at 94.5%, demonstrating good potential for cyclic recovery.

2. To overcome the mass-transfer limitations of conventional adsorption in dilute solutions, MoO_3/SnO_2 bimetallic oxide heterointerfaces were constructed for electro-assisted preferential capture of gallium. Controlled incorporation of SnO_2 triggered charge rearrangement at the heterointerface, thereby contributing to suppressing the hydrogen evolution reaction. Over a broad concentration range of 0.5-200 mg L^{-1}, the maximum gallium recovery capacity reached 486.3 mg g^{-1}. Even at trace gallium concentrations of 0.5-1.0 mg L^{-1}, recovery efficiencies remained as high as 97.3-98.2%. Stepwise voltage programming further enabled preferential gallium separation from multicomponent systems, with selectivity coefficients of 1261.7, 25.3, 77.5, and 244.0 over Pb, Al, Ge, and Zn, respectively. The strategy also remained effective in simulated

leachate derived from zinc-smelting residues.

Although excellent separation and recovery performance was achieved in dilute simulated systems, actual secondary aqueous resources generally contain more complex ionic compositions, variable acidity, and diverse organic and inorganic impurities, whose effects on long-term material stability and interfacial reactions require further investigation. Future work should focus on the long-term validation of gallium and indium separation in secondary aqueous resources and on establishing downstream processes for isolating and purification of high-purity PGM products from metal-loaded electrodes.

Appendix I. Articles and patents published during the Ph. D studies

([1]indicates first author, *indicates corresponding author.)

Articles published during the Ph. D studies:

[1] **Ning Wang[1]**, Zhongkang Wang, Yuxuan Xie, Huanyu Zhu, Jianbo Li, Peng Chen, Feifei Jia, Mildred Quintana, Shaoxian Song. Electro-assisted preferential gallium capture from dilute streams enabled by oxygen coordination at bimetallic oxide heterointerfaces, Separation and Purification Technology. 403 (2026) 138781. (JCR Q1, IF 9.1)

[2] **Ning Wang[1]**, Jianbo Li, Feifei Jia, Hongru Zhou, Yuxuan Xie, Peng Chen, Shaoxian Song, Mildred Quintana. Unraveling nitrogen-doped and vacancy-engineered synergistically modified molybdenum oxide promoting gallium selective adsorption, Separation and Purification Technology. 358 (2025) 130158. (JCR Q1, IF 9.1)

[3] **Ning Wang[1]**, Yifeng Xu, Lai Peng, Chuanzhou Liang, Shaoxian Song, Mildred Quintana. Biotic and abiotic removal of acetaminophen during sidestream partial nitritation processes: Underlying mechanisms and transformation pathways, Science of the Total Environment. 958 (2025) 177836.

[4] Huan Zhang, Jiayi Zhang, Huanyu Zhu, Zihao Song, **Ning Wang***, Jianbo Li, Feifei Jia, Shaoxian Song, Activated alumina sphere-supported CdS-MoS_2 heterojunctions: A high-performance catalyst for gold recovery, Journal of Environmental Chemical Engineering. 14 (2026) 122775. (JCR Q1, IF 7.5)

[5] Xuyang Qin, Wenqiang Xu, **Ning Wang***, Peng Chen*, Huanyu Zhu, Mildred Quintana, Hongqiang Li, Shaoxian Song, Fe_3O_4-modified zirconium-based metal-organic framework as a recyclable sorbent for rapid and efficient phosphate removal, Applied Surface Science. 749 (2026) 167932. (JCR Q1, IF 6.6)

Patents published during the Ph. D studies:

[1] Feifei Jia, **Ning Wang**, Peng Chen, Hongru Zhou, Shaoxian Song, 2025. A chemisorption and electrosorption coupling process for short-process recovering of low concentration platinum. Chinese Patent, ZL 202410513166.7 (Authorized)

[2] Jianbo Li, **Ning Wang**, Linshuang Liu, Jingjing Wu, Feifei Jia, Shaoxian Song, 2024. A Gallium Adsorbent, Preparation Method and Application. Chinese Patent, ZL 202411058205.5 (Authorized)

Appendix II. Experimental data

Table II.1 Ga(III) adsorption efficiency of α-MoO_x/N with different nitrogen doping amounts in acidic solutions.

Time (min)	Adsorption efficiency (%)			
	α-MoO_x	α-MoO_x/N-1.05	α-MoO_x/N-0.53	α-MoO_x/N-0.35
0	0	0	0	0
30	11.71	51.41	58.05	89.72
60	13.84	90.97	96.31	98.77
90	16.88	96.82	97.26	98.85
120	31.47	96.88	98.46	99.03
150	58.56	96.86	98.76	99.43
180	89.77	97.20	99.35	99.98
210	92.69	97.68	99.57	99.98
240	92.42	97.08	99.84	99.99

Table II.2 Adsorption kinetic data of Ga(III) on α-MoO_x/N-0.53 at different initial concentrations.

Time (min)	Adsorption capacity (mg g^{-1})								
	5 mg L^{-1}	10 mg L^{-1}	20 mg L^{-1}	30 mg L^{-1}	40 mg L^{-1}	50 mg L^{-1}	60 mg L^{-1}	90 mg L^{-1}	100 mg L^{-1}
0	0	0	0	33.75	42.88	41.98	42.7	42.94	33.75
15	6.03	10.03	33.75	48.12	47.12	51.67	-	65.41	48.11
30	7.17	22.32	48.12	53.74	91.65	113.75	145.70	151.84	53.76
60	8.07	27.10	53.73	56.32	92.45	120.05	156.98	178.65	56.31
90	8.40	27.47	56.32	57.78	92.45	123.52	158.09	186.17	57.72
120	8.77	27.47	57.78	57.95	92.53	123.55	157.56	199.87	57.95
150	8.97	27.77	57.95	57.98	93.60	124.80	156.80	200.33	57.93
180	9.16	27.83	57.98	58.00	93.83	124.98	156.93	201.57	58.00
240	9.42	28.05	58.02	33.75	42.88	41.88	42.70	42.94	33.75

Table II.3 Adsorption efficiencies and selectivity coefficients of α-MoO_x/N-0.53 for Ga(III) and coexisting In(III), Fe(III), Cr(III), Zn(II), Al(III), Cu(II), Ni(II) in binary systems.

Ga/M	Adsorption efficiency (%)		Selection coefficient
	Ga	M	
Ga/In	92.24	59.04	5.63
Ga/Fe	87.91	33.77	14.45
Ga/Cr	89.03	31.71	18.50
Ga/Zn	94.82	5.59	298.11
Ga/Al	86.65	6.78	90.87
Ga/Cu	72.28	5.88	58.21
Ga/Ni	97.62	12.85	102.31

Table II.4 Gallium recovery performance and current efficiency of asymmetric chemisorption and electrosorption coupling systems with different cathodes at 1.8 V.

Time (min)	Adsorption capacity (mg g^{-1})				
	MoO_3	SnO_2	MoO_3/ SnO_2-0.25	MoO_3/ SnO_2-0.50	MoO_3/ SnO_2-0.75
0	0	0	0	0	0
30	35.97	39.13	42.12	47.97	41.69
60	62.66	62.07	69.78	70.87	59.56
120	100.50	90.35	98.36	115.32	91.18
180	113.56	107.37	128.00	139.09	115.68
240	115.35	110.96	135.29	145.50	117.33
Current efficiency	58.87%	54.64%	70.48%	77.28%	62.32%

Table II.5 Effect of pH on gallium recovery kinetics in the chemisorption and electrosorption coupling system (V = 100 mL, C = 50 mg L^{-1}).

Time (min)	Adsorption capacity (mg g^{-1})					
	pH=1	pH=2	pH=3	pH=9	pH=10	pH=11
0	0	0	0	0	0	0
30	4.40	7.95	45.85	35.36	43.39	1.07
60	5.85	17.94	77.37	55.73	68.17	2.65

120	6.99	49.74	104.11	74.31	75.79	2.87
180	8.96	76.91	135.05	95.01	90.80	8.31
240	11.02	93.25	140.51	111.81	100.64	13.35

Table II.6 Effect of voltage on gallium recovery kinetics in the chemisorption and electrosorption coupling system.

Time (min)	Adsorption capacity (mg g^{-1})				
	1.0 V	1.4 V	1.8 V	2.2 V	2.6 V
0	0	0	0	0	0
30	24.92	29.68	45.85	48.93	60.75
60	40.57	40.49	77.37	83.04	94.48
120	48.06	57.68	104.11	121.83	122.66
180	57.90	74.36	135.01	127.14	125.01
240	60.33	79.34	140.58	127.89	125.41

Table II.7 Comparison of gallium recovery performance by chemisorption and electrosorption coupling, adsorption and electrodeposition.

Time (min)	Concentration (mg L^{-1})		
	Chemisorption and electrosorption	Adsorption	Electrosorption
0	52.94	50.94	52.71
60	23.86	39.66	46.65
120	13.765	36.05	44.31
180	2.14	32.82	41.38
240	0.09	31.42	39.06